ABSTRACT

Title of Dissertation: CONTROLLING LIGHT
                                PROPAGATION IN COMPLEX MEDIA
                                FOR IMAGING, FOCUSING AND
                                BRILLOUIN MEASUREMENTS

                                Eitan Edrei, Doctor of Philosophy, 2018

Dissertation directed by: Professor Giuliano Scarcelli
                                Fischell Department of Bioengineering

Imaging and focusing light through turbid media are two fundamental challenges of optical

sciences that have attracted significant attention in recent years. Traditional optical systems

such as confocal microscopy, optical coherence tomography and multi-photon microscopy

utilize ballistic photons traveling in straight trajectories to generate an image; however, with

increasing depth, the signal to noise ratio (SNR) decreases as the number of ballistic photons

decays exponentially. In the first part of this thesis I present two novel techniques for imaging

through scattering medium by decoding seemingly random scattered light patterns and

demonstrate the highest resolution and acquisition speed to date. For point scanning

applications I also study methods to focus light through scattering materials and report on a

fundamental trade-off between the focal point intensity and the focal plane in which it is

generated.

        In the second part of the thesis I investigate how the ability to control light

propagation within turbid media can be used to enhance point scanning measurements such

as Brillouin scattering spectroscopy, a technology recently developed in our lab to

characterize material stiffness without contact. To do this, I first present a novel optical

system ("spectral coronagraph") which yields an improved extinction ratio when inserted

into Brillouin spectrometers to enable the spectral separation in the presence of scattering or close to interfaces. Additionally, to enhance the Brillouin signal, I apply adaptive optics techniques, first developed for astronomy applications, where the incident wave front is shaped to circumvent for optical phase aberrations. Using adaptive optics, I show signal enhancement in artificial and biological samples, an important feature in the context of Brillouin microscopy to promote high SNR imaging in practical scenarios.

CONTROLLING LIGHT PROPAGATION IN COMPLEX MEDIA FOR IMAGING,
FOCUSING AND BRILLOUIN MEASUREMENTS

by

Eitan Edrei

Dissertation submitted to the Faculty of the Graduate School of the
University of Maryland, College Park in partial fulfillment
of the requirements for the degree of
Doctor of Philosophy
2018

Advisory Committee:
  Professor Giuliano Scarcelli, Chair
  Professor Howard M. Milchberg
  Professor Ian M. White
  Professor Peter Kofinas
  Professor Yu Chen

Dedications

To my beloved wife Chen for the unconditional support throughout my doctoral studies, I couldn't have done this without you and I feel truly lucky to have you as my partner in life. To my sweet children Rei, Shahar and Omer which fill my life with joy and remined me that time should be efficiently managed as it is precious and valuable. To my parents Dr. Itzhak and Dr. Rachel Edrei who instilled in me a passion for science from an early age and provided moral and financial support throughout my journey of pursuing higher education abroad. To Shimon and Hana Mandel my in-laws, who were always willing to assist with generosity and without limits.

Acknowledgements

I would like to express my sincere gratitude to my advisor and mentor Dr. Giuliano Scarcelli who has been involved in all aspects of my work through guiding and inspiring as well as criticizing and polishing of ideas. I feel truly lucky to have had such a bright and motivated mentor with a profound knowledge of the underlying physics of the field and simultaneously an open mind and broad vision to explore new ideas. His mentoring has tremendously advanced my research skills and gave me a solid foundation for my future work as a scientist. I would also like to mention the great flexibility he has granted me throughout my doctoral studies and his exceptional availability to all his students. These characteristics reflect upon his unique personality as a mentor and a friend. Giuliano, it was an honor working alongside with you.

I would also like to thank the talented people I have worked with during my doctoral studies who provided advises and new perspectives through personal discussions or group meetings: Dr. Jitao Zhang, Dr. Hongyuan Zhang, Dr. Johnny Suzuki, Antonio Fiore, Milos Nikolic, Christina Conrad, Joshua Webb, Romanus Hutchins, Kim Berghaus, Thomas Mumford and Angelina Nou.

I wish to thank my dissertation committee members for their useful advices and insights and for offering their time, support, guidance and good will.

Finally, I would like to thank the Fischell Fellowship and the Ann. G Wylie Fellowship for providing me the resources to successfully complete my dissertation.

Table of contents

Part II: Brillouin spectroscopy within scattering and aberrating materials

Chapter 1

Introduction

Optical modalities are widespread in biological research and clinical medicine because of several advantageous features. The high resolution obtained by optical imaging which is a result of the short wavelength of the visible spectrum (<1 µm), has a great potential for imaging on the microscopic scale, which is crucial in many applications. The relatively low cost of optical modalities can enable the wide distribution of photonic devices. Moreover, importantly, because of the complex interactions between light and matter one can extract functional information of the sample under study, which often can't be obtained otherwise; for instance, the interaction between light and spontaneous acoustic phonons or with vibrational molecular modes within materials gives rise to the Brillouin and Raman scattering phenomenon's respectively.

Unfortunately, the advantage of light-based modalities comes with a severe drawback; short wavelengths are highly susceptible to scattering as the scattered intensity is typically inversely proportional to the wavelength. Since most biological tissues are not transparent, traditional optical imaging and focusing in biological tissue are fundamentally limited in terms of depth and resolution (Ntziachristos, 2010). Scattering presents an additional and even greater challenge for Brillouin spectroscopy which features a weak signal that is very close in frequency to the incident light. Elastic scattering (i.e. non-shifted in frequency) enhances the intensity of the non-shifted excitation peak, which makes the slightly shifted Brillouin spectral signatures

undetectable. Indeed, although Brillouin microscopy has recently emerged as a promising tool in biomedical applications, so far it has only been applied in transparent materials such as corneal and lens tissue or single cells (Scarcelli and Yun, 2008, Scarcelli et al., 2012, Scarcelli and Yun, 2012, Scarcelli et al., 2015b, Remer and Bilenca, 2016a).

In this thesis, we report on the development of techniques to overcome the effect of scattering on optical modalities. The effect of scattering on system performances varies among different optical modalities and depends on parameters such as coherence vs incoherence illumination and upon specific needs and applications such as imaging, focusing or spectroscopic measurement. Hence, treatment for each modality is unique and throughout this thesis we present different methods which are compatible with the requirements of each modality. Nonetheless, the different techniques rely on some common underlying concepts which we will introduce in this chapter.

This thesis is composed of two parts. The first part contains three chapters and deals with the problem of overcoming scattering effects in imaging and focusing systems. The second part contains four chapters and addresses the specific scattering challenges of Brillouin spectroscopy. The first part begins with Chapter 2: we describe a novel modality which enables imaging through dynamic scattering materials. This technique is based on coherent illumination and in contrast to competitive technologies, it is immune to movements of the scattering material. This is an important feature because most biological samples are not stable for long time periods. Chapter 3 introduces an incoherent imaging modality through scattering materials which provides sub-diffraction resolution and can be applied to common scenarios such as fluorescence microscopy. In chapter 4 we move the discussion from imaging to focusing applications. This is important because many optical modalities (including imaging systems) rely on a point by point scanning

process (for instance, confocal microscopy and two-photon microscopy); hence, the ability to focus light through scattering materials is beneficial. In this context, we analyze the fundamental principles of methods developed to focus light through highly scattering materials; we analytically derive and experimentally demonstrate the ultimate limits of such systems thus providing methods to reach optimal performances.

Part II begins with chapter 5 in which we discuss the additional challenge presented by elastic scattering on Brillouin spectral measurements. We then introduce the concept of a "spectral coronagraph", an optical system we integrated into Brillouin spectrometers to suppress elastic scattering effects. In chapter 6, we discuss the precision of Brillouin measurements, its dependence on optical specifications as well as on the analysis method and demonstrate solutions to improve such precision. Chapter 7 is devoted to the method of signal enhancement via wave-front shaping to correct for weak scattering resulting from large scale variations of the refractive index. Here we show how the performances of such method are expected to decrease in spectroscopy where the signal can arise from any location within the illumination path. In chapter 8 we apply the wave-front shaping method as introduced in chapter 7 to Brillouin spectroscopy. We show improvement of both signal and resolution in phantom samples as well as in biological specimens. Finally, chapter 9 includes conclusions of the different principles introduced in the thesis and emphasizes the specific contributions this thesis has had on the research of each field. In this chapter, we also discuss future work which can further advance the principles introduced in the thesis.

1.1 Effect of scattering on light propagation

Light propagation through a turbid medium is a complex process with many individual scattering events, each of which disrupts the light path in an independent manner. The characteristic length

scale governing the scattering process is the average distance between scattering events which is often referred to as the mean-free path (MFP). This quantity can also be linked to the inhomogeneity of the refractive index, i.e. it represents the average spatial scale of the refractive index variability, which is the underlying cause of scattering. In biological tissues the MFP is approximately 100µm (Jacques, 2013), within this length-scale a large amount of photons are considered ballistic, i.e. they manage to travel in a straight trajectory. However, after propagation through several MFP's of scattering medium, correlations between the incoming and out coming fields are lost and the light distribution approaches a "random walk" with no resemblance to the original incoming structure; often, this is referred to as the "diffusive regime".

More quantitatively, the decrease in number of ballistic photons as a function of distance traveled through the sample is described by the Beer-Lambert law:

$$I(z) = I_0 e^{-\mu \cdot z} \quad (1.1)$$

Where µ in the absence of absorption is the scattering coefficient defined as: $\mu = {}^1\!/_{MFP}$. Hence, if light emerging from an object is transmitted through a scattering medium a distance of 3 MFP's, less than 5 % of the incoming photons preserve their original trajectories. It is therefore nearly impossible to reconstruct the original distribution of the electromagnetic field using a simple wide-field imaging system.

Although the transition between the ballistic and diffusive regimes is a continuum, in practice, it is useful to distinguish between weakly scattering and highly scattering scenarios. In weakly scattering scenarios, the scattering is caused by large-scaled slowly-varying refractive index mismatches, hereby referred to as aberrations. On the contrary, in highly scattering cases, the spatial scale of refractive index variations is small and can even be smaller than the wavelength.

Coherent light traveling through a highly scattering medium will typically generate "speckles", i.e. a random interference pattern, on a distant screen.

Highly scattering processes are typically categorized by the size of the scattering particles (or equivalently, the spatial scale of refractive index variations); Mie scattering refers to scenarios in which the scattering scale is of equal size or bigger than the wavelength while in Rayleigh scattering the scale is much smaller than the transmitted wavelength. Each scattering type has a different dependence on wavelength as well as a different angular spread isotropy. Light propagation through biological tissues involves both scattering regimes but is dominated by Mie scattering events (Mourant et al., 1998, Johnsen and Widder, 1999). The preponderance of Mie scattering has a direct impact on the isotropy of scattering within biological tissues; Mie scattering is mostly forward directed, therefore scattering within biological tissues is not isotropic. The anisotropy parameter is defined as:

$$g = \langle cos\emptyset \rangle \quad (1.2)$$

Where $\emptyset$ is the tilting angle after the scattering event. For biological tissues, the value of g is typically high (>0.9), indicating that the scattering directionality is close to the normal incident angle (Jacques, 2013, Yaroslavsky et al., 2002, Cheong et al., 1990).

1.2 Approaches for suppressing aberrations and scattering effects in imaging systems

Historically, many methods have been introduced to enable better optical performances within scattering or aberrating materials. The different approaches to deal with the degradation of optical capabilities by scattering can be divided into three main categories. The first category includes long established methods which are designed to counteract the aberrations by wave-front shaping.

In these techniques, generally referred to as adaptive-optics (AO) systems, a beam is spatially modified by a pre-designed phase map complementary to the refractive index variations of the aberrating material (Tyson, 2015). The second category includes modalities designed to reject photons undergoing multiple scattering events (diffusive photons) and provide an image comprised of only the non-scattered ballistic photons. A large number of well-established modalities belong to this category such as confocal microscopy (Pawley, 2010), multiphoton microscopy (Denk et al., 1990) and optical coherence tomography (OCT) (Huang et al., 1991). The third category is of more recent development and encompasses several methods designed to "decode" the scrambled information carried by the scattered (i.e. diffused) photons. We will discuss the different approaches and their limitations; within each modality we will emphasize the concepts relevant for this thesis.

1.2.1 Adaptive optics

Adaptive optics is a technique originally developed by astronomers to correct blurriness of images caused by atmospheric aberrations (Tyson, 2015, Beckers, 1993). The principle relies on measuring the aberrated wave-front and on correcting these aberrations by introducing local phase variations applied by an active device such as a deformable mirror. In recent years AO has become a useful strategy in optical microscopy as well, enabling real-time correction of sample induced aberrations (Wang et al., 2014b, Wang et al., 2015b, Ji et al., 2010, Tao et al., 2011a, Roorda and Williams, 1999). AO techniques can be classified into direct and indirect methods. Typically, in direct methods a 'guide star' is placed or generated in the desired imaging plane and the wave-front is monitored by a wave-front sensor. In contrast, indirect methods either apply an iterative process to estimate the aberration or calculate the aberration from an acquired image. After the

aberration is determined, the correct phase map can be presented as a combination of a set of orthogonal polynomials and projected by the deformable mirror to counteract the aberrations introduced by the sample. The set of Zernike polynomials are commonly used to represent such aberrations as they have circular boundary conditions and are therefore suitable for circular apertures such as lenses. Direct approaches are faster because a single acquisition is needed to measure the phase aberration; however, the wave-front measurement requires a guide-star (i.e. a point-like emitter) at the measured location, which may be difficult to introduce, especially *in vivo*.

Two main strategies have been applied to correct phase distortions, the first is named "pupil adaptive optics" in which the deformable mirror is placed conjugate to the pupil of the imaging system. In this case if the aberrations are spatially variant, the field of view will be limited to a small region around the optimizing location (the 'guide star'), and therefore it is most suitable for point-scanning techniques. A second method named "conjugate adaptive optics" is designed to provide a larger field of view by placing the deformable mirror in conjugate plane to the sample plane where the aberrations are generated. In this configuration the correction process is valid within a much larger field of view, and it is most suitable for wide field microscopy (Johnston and Welsh, 1994, Ragazzoni et al., 2000, Mertz et al., 2015, Park et al., 2015). We will discuss and show implementations of AO in Brillouin spectroscopy in chapters 7 and 8.

It is important to realize the limitations of AO in correcting for scattering events. Conventional AO was successfully implemented in scenarios where the wave-front variations occur over long distance such as the atmosphere or to correct for aberrations of the eye (Roorda et al., 2002). In such cases, both the sensing and the correcting procedures have enough resolution to accurately match the distortion phase profile; however, in the case of highly scattering medium standard AO fails (Tyson, 2015, Katz et al., 2012).

In recent years modified AO techniques were used to generate a high intense focal point beyond highly scattering materials by means of constructive interference. Using a spatial light modulator (SLM) with many pixels providing independent control of thousands of degrees of freedom, several researchers were able to shape the interference pattern and obtain a focal point with 2-3 orders of magnitude higher intensity than the average background (Vellekoop and Mosk, 2007, Vellekoop et al., 2010, Vellekoop and Aegerter, 2010). This can be done either by performing a measurement of the phase map, a method known as optical phase conjugation (OPC), (Yaqoob et al., 2008) or by placing the SLM within the optical path and applying an iterative feedback algorithm to enhance a single point behind the scattering layer. Similar modalities have been applied to deliver light within deep biological samples (Liu et al., 2015). However, despite the exciting progress in the field, the ability to transform these achievements into practical functioning modalities have been lacking. This is partially attributed to the fact that only a small amount of the total energy delivered by the beam is focused into a single location, yielding a Strehl ratio (i.e. the ratio between the peak intensity to the maximal intensity obtained using an ideal optical system) of 2 % at most. We will further discuss and demonstrate the trade-offs of these techniques in chapters 4.

1.2.2 Gating of ballistic photons

Many well-established methods which are commercially available are based on a gating mechanism, i.e. scattered diffusive photons are blocked and only ballistic photons are analyzed. For instance, a confocal microscope is designed to spatially reject diffusive photons using a pinhole placed in front of the light collecting detector (Pawley, J. 2010); Optical coherence tomography is based on coherent gating so multiply scattered light doesn't contribute the interference pattern

(Huang et al., 1991); multi-photon microscopes require high intensity distribution to initiate the non-linear process which can't be achieved by diffusive light (Helmchen and Denk, 2005). However, since the number of ballistic photons decay exponentially with depth (see equation 1.1), traditional imaging modalities are not suitable for the diffusive regime.

1.2.3 Decoding information from diffusive photons

An underlying concept shared by several methods to enable reconstruction of objects hidden behind scattering materials is that light injected at one end of a scattering material still preserves some correlations to its original field as it is transmitted through the other end. This can be understood by considering a tightly confined intensity distribution of light entering from one end of a scattering material, the intensity distribution will broaden spatially as it propagates through the material and will appear with a final width of $\sim 2L$ at the other end (L being the width of the scattering material) (Freund et al., 1988). This implies that any light distribution transmitted through a scattering material is still correlated to the original form, however, it undergoes a broadening process proportional to the width of the scattering material, a phenomenon known as the "shower curtain effect". The dependency of the "shower curtain effect" solely on the thickness of the scattering layer may seem striking at first, however, it can be derived from some fundamental properties of light propagation in scattering medium: It has been shown that the mean path length traveled by light within a disordered medium is invariant with respect to the internal microstructure of the medium and only depends on its' geometrical boundaries (Pierrat et al., 2014, Savo et al., 2017). Quantitatively, the mean path is given by: $\langle l \rangle = \frac{4V}{\Sigma}$, where V is the volume of the disordered medium and Σ is the surface area. For a scattering material layer of thickness L and area A the volume is $L \cdot A$ and the surface area is roughly $2A$, hence $\langle l \rangle \approx 2L$.

The shower-curtain effect is routinely observed in our everyday life: an object placed behind a scattering layer appears blurred, but if the object is attached to the scattering layer, it can be clearly resolved as long as the scattering layer is thin. In chapter 2 we show how we can exploit this phenomenon to image thorough scattering materials.

In the far-field, this phenomenon is translated into what is known as the "memory effect" (Freund et al., 1988). The memory-effect, first described in the 1980's, is a peculiar phenomenon observed when light propagates through a scattering medium (Feng et al., 1988, Freund et al., 1988, Freund, 1990). Within a certain range of impinging angles, known as the memory-effect angular range, the seemingly-random speckle patterns observed after the scattering medium are highly correlated, i.e. the patterns resulting from different incoming angles are mostly just shifted with respect to each other. The correlation function decays monotonically as a function of the angular range, and the profile depends on the layer thickness as well as the wave-number:

$$C(\Delta\theta) = \left[\frac{k|\Delta\theta|L}{sinh(k|\Delta\theta|L)}\right]^2 \quad (1.3)$$

where $\Delta\theta$ is the angular spread of the illuminating beam, L is the thickness of the layer and k is the wave-number. Several modalities where recently developed based on the aforementioned concepts. Bertolotti et al (Bertolotti et al., 2012) first presented a study in which a fluorescent object was hidden behind a highly scattering layer. By performing a scanning procedure while varying the illumination angle within the angular range of the memory effect, they were able to reconstruct the object. Katz et al (Katz et al., 2014a) introduced a similar modality which enabled a single shot reconstruction instead of a lengthy scanning process. In chapter 3 we show how the memory effect can be used in a different manner based on deconvolution to enable imaging through highly scattering material.

These newly developed methods which decode information from diffusive photons are still limited either in terms of imaging depth or the stability requirements of the scattering material; however, they pave the way towards further advances in the field as we will discuss in the first part of this thesis.

1.3 Scattering effects in Brillouin spectroscopy

1.3.1 Brillouin micro-spectroscopy

Brillouin spectroscopy is a measure of the inelastic interactions between photons and propagating acoustic sound waves (phonons) within a material (Boyd, 2008). In this process the incoming photons can either loose or gain energy and therefore acquire a frequency shift. Thus, a typical Brillouin spectrum is composed of three peaks – the central Rayleigh peak which comes from the elastic scattering from the sample and has the same frequency as the original excitation laser, and two shifted peaks, named stokes and anti-stokes. The Brillouin frequency shift depends on material properties such as the elastic modulus, refractive index and density, therefore for many decades, Brillouin light scattering spectroscopy, based on acoustic phonon-photon interaction, has been a powerful optical technique in applied physics and material science due to its unique ability to characterize mechanical properties of materials at high spatial resolution without contact (Dil, 1982, Hartschuh et al., 2005, Benedek and Fritsch, 1966, Fleury and Boon, 1969, Koski et al., 2013).

In this technique, a monochromatic beam is directed to a region of interest and is inelastically scattered by the material. As a result of acoustic waves traveling through the matter, a slight shift of the scattered light frequency can be detected using a high-resolution spectrometer.

The size of the shift is proportional to the longitudinal modulus of the material following the equation:

$$\Omega = 2n\frac{v}{\lambda}sin\frac{\theta}{2} \quad (1.4)$$

where Ω is the frequency shift, n is the refractive index, λ is the wavelength, θ is the scattering angle and v is the speed of sound which can be expressed in terms of the longitudinal modulus and the density: $v = \sqrt{\frac{K}{\rho}}$ (Boyd, 2008). Historically, spectrometers based on a cascade of Fabry-Perot etalons have provided sufficient extinction and resolution to detect and resolve Brillouin peaks (Meng et al., 2016, Dil, 1982). These devices are based on two parallel mirrors which are typically ~95 % reflective and the distance between the mirrors determines the wavelength which can efficiently be transmitted through the etalon by means of constructive interference. Yet, measurements with multi-pass Fabry-Perot interferometers are time consuming as scanning of the distance between the mirrors is required to obtain a full spectrum which is generally not practical for imaging and/or biomedical applications. More recently, spectrometers based on virtually-imaged-phased-array (VIPA) etalons were developed where the beam is focused into the etalon and the back faced mirror is completely reflective. These devices enabled rapid measurements of Brillouin spectra with high throughput in a single shot (Scarcelli and Yun, 2008, Scarcelli and Yun, 2011).

Using VIPA spectrometers, Brillouin spectroscopy combined with confocal microscopy has found biological applications in cell biomechanics (Scarcelli et al., 2015b, Elsayad et al., 2016, Zhang et al., 2017, Antonacci and Braakman, 2016, Meng et al., 2016, Mattana et al., 2017, Palombo et al., 2014), plaque characterization (Antonacci et al., 2015b) and is being tested in the clinic for ophthalmology applications (Besner et al., 2016, Scarcelli et al., 2015a).

1.3.2 The twofold effect of elastic scattering on Brillouin spectra

For Brillouin spectral measurements, two specifications are critical: due to the small spectral shift of Brillouin signatures, high spectral contrast (or extinction) is needed within spectrometers to eliminate noise from the incident laser or stray light; in addition, Brillouin interaction has a small scattering cross-section defined as the ratio between the incoming intensity flux and the total scattered power from a volume of interest. Hence, the number of photons available for detection are fundamentally limited and a highly sensitive devices are required.

As elastic scattering is introduced within the beam path, it presents a double challenge to the detection of the inelastic Brillouin signatures: 1. As in imaging applications, the elastic scattering reduces the amount of light delivered to the focal point, and the measured signal is degraded. 2. The elastic scattering may enter the spectrometer and appears as a high intense peak at the spectral origin (i.e. non-shifted light). Since the Brillouin signals are located in close proximity to the non-shifted signature, it becomes very difficult to separate them from the significantly more intense central peak.

In recent years, a great amount of research has been conducted to increase the spectral extinction of VIPA-based spectrometers. One solution is to increase the spectral selection of the spectrometer: a third VIPA spectrometer stage (Scarcelli and Yun, 2011) or a narrowband filter within the optical train such as a Fabry-Perot etalon (Fiore et al., 2016, Shao et al., 2016) were inserted in the spectrometer and provided improved extinction of 20 dB or more, but with significant insertion losses; the spectral selection of the spectrometer was also increased by inserting an absorbing gas chamber (Meng et al., 2014) which can give both high extinction and low losses but requires tunable lasers and frequency locking to maintain stable rejections. Another approach is to eliminate the non-shifted light component by destructive interference (Antonacci et

al., 2015a); this can reach up to 35 dB added extinction with moderate loss but generally only works for a specific reflection plane and stably maintaining the efficiency of the spectrometer over time can be challenging. Beam shaping of the VIPA output has yielded moderate increase in extinction of up to 10 dB for only 10% insertion loss (Scarcelli et al., 2015b), but the insertion losses become significant if higher extinctions are required. Finally, also stimulated Brillouin scattering has been shown to improve the discrimination between elastic scattering and Brillouin-shifted components (Remer and Bilenca, 2016a).

Despite the vast amount of effort invested and the high extinction rate provided by modern spectrometers, the signal of Brillouin measurements degrades rapidly with depth even in translucent samples. Throughout the second part of this thesis we demonstrate methods to improve both the extinction performances of the spectrometer (chapter 5) but also enhance the Brillouin signal deeper within aberrating samples by means of AO (chapters 7,8).

PART I

Imaging and focusing through scattering materials

Chapter 2

Coherent imaging through scattering medium by means of the shower-curtain effect[*]

In this chapter, we will introduce a coherent method for imaging through highly scattering dynamic medium. Several phenomena have been recently exploited to circumvent scattering and have succeeded in imaging or focusing light through turbid layers. However, the requirement for the turbid medium to be steady during the imaging process remains a fundamental limitation of these methods. Here we introduce an optical imaging modality that overcomes this challenge by taking advantage of the so-called shower-curtain effect, adapted to the spatial-frequency domain via speckle correlography. We present high resolution imaging of objects hidden behind millimeter-thick tissue or dense lens cataracts. We demonstrate our imaging technique to be insensitive to rapid medium movements (> 5 m/s) beyond any biologically-relevant motion. Furthermore, we show this method can be extended to several contrast mechanisms and imaging configurations.

---

[*] The results of this chapter were part of a peer reviewed publication, *Optica* 3 (1), 2016.

2.1 Principle: imaging correlography

The optical system we developed takes advantage of the shower-curtain effect properties and generalizes them to achieve high-resolution imaging of objects placed at a nearly arbitrary distance behind the scattering medium. The imaging procedure is based on retrieving the object's Fourier transform from the turbid medium (used as the shower curtain) through a correlography technique based on speckle illumination.

Imaging correlography (Idell et al., 1987, Idell et al., 1989, Voelz et al., 1991), which was developed in the 1980s, uses similar principles as speckle interferometry (Labeyrie, 1970, Dainty, 1975). A coherent beam is diffused by a scattering object (Fig. 2.1a), giving rise to a speckled object field $f_n(x, y)$, where the subscript n refers to a specific speckle configuration emerging from the object. After propagation to the far field, a two-dimensional Fourier transform $\left|\hat{F}[f_n(x, y)]\right|^2$ can be observed. By the Wiener–Khinchin theorem, the Fourier transform of this pattern is related to the autocorrelation of the speckled object:

$$\hat{F}\left|\hat{F}[f_n(x, y)]\right|^2 = f_n(x, y) \star f_n(x, y) \qquad (2.1)$$

Averaging over many independent realizations of processed speckle patterns, the autocorrelation of the original object can be obtained (Idell et al., 1987, Idell et al., 1989, Voelz et al., 1991).

From the autocorrelation function which does not have phase information, a phase retrieval algorithm can be applied to image the object (Fienup, 1978, Fienup, 1982). The algorithm in its' basic version assumes a random phase matrix as an initial guess and applies it together with the intensity pattern to obtain a guess of the object using an inverse Fourier transform. Since the object of interest is known to have only real and positive values, the algorithm will change iteratively (by a pre-defined value) the matrix guess at the locations where an imaginary or negative value was

obtained. After several iterations only real and positive values are generated, and the object is reconstructed.

Traditional imaging correlography techniques are not suitable for imaging close objects behind highly scattering media. Here, we overcome these issues through the shower-curtain effect and with speckle illumination. By illuminating the object with a speckle pattern rather than a coherent beam, we extend the correlography technique to transmitting or other non-scattering objects. More importantly, we show that the correlography principles can be effectively applied in the near field. While the far-field condition is usually known as: $z > \frac{2D^2}{\lambda}$ (D, size of the object; λ, wavelength), by tuning the spatial coherence of the illumination beam, as one can do with speckle illumination, the "far-field" condition can be written as:

$$z > \frac{2D \cdot R_c}{\lambda} \qquad (2.2)$$

where R_c is the correlation radius of the speckle pattern (Goodman and Haupt, 2015). This interesting modification to the far-field condition can be intuitively understood by the following reasoning: The far-field is obtained at a plane in which each individual field emitted from a location on the object interferes with all other fields emerging from the object. Therefore, it depends on two parameters: 1. The size of the object – the bigger it is the more the field needs to travel to achieve complete interference from the entire aperture. 2. The angle at which the field diverges from the object which is inversely proportional to the aperture size (multiplied by the wavelength). For a coherent illumination, these two parameters are proportional to the size of the object D, and this is the origin of the D^2 in the far-field expression. In partially coherent illumination the divergence angle is enlarged and is determined by the coherence area (i.e. the speckle size), and therefore the far-field is described by equation 2.2.

We experimentally verified the near-field validity of our protocol by illuminating a double-slit aperture (width 150 μm, separation 1 mm) with a coherent beam and with a speckle pattern. Placing the camera in the near field (50 mm), we observed the double-slit Fresnel diffraction pattern as expected [Figs. 2.1(b) and 2.1(c)]; however, by performing our correlography-based reconstruction, we obtained the Fourier transform of the double slit as if we were working under the Fraunhofer "far field" diffraction condition [Figs. 2.1(d) and 2.1(e)].
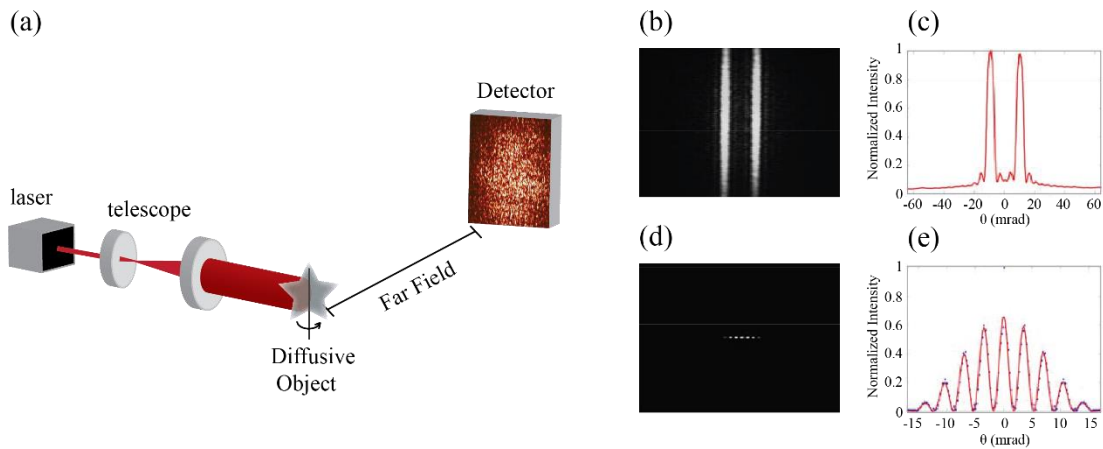
Figure 2.1. (a) Imaging correlography setup: different speckle realizations are recorded by tilting slightly the diffusive object. (b) Diffraction pattern observed 50 mm from a double slit aperture when illuminated by a coherent laser beam. (c) The line plot corresponding to the average of the recorded pattern shows a clear near-field Fresnel pattern. (d) Diffraction pattern observed 50 mm from the aperture as retrieved by correlography analysis when the slits are illuminated by a speckle pattern. (e) The corresponding averaged line plot clearly shows a far-field diffraction pattern, as confirmed by the fit to the Fourier transform of the double slit (red line).

Using this property, in practice, for objects with sizes ranging between 100 μm and 1 mm, the Fourier transform can traditionally only be recorded at distances as high as tens of centimeters; instead, we can reduce this distance requirement by one to two orders of magnitude by tuning the illuminating speckle size between 1 and 10 μm. This makes our technology compatible with

biomedical applications such as retinal imaging behind cataracts or imaging of the back of the ear behind the tympanic membrane.

2.2 Methods

Our experimental setup, processing procedure, and exemplary results are shown in Fig. 2.2. We employed a He–Ne laser beam at 632 nm; after expanding the beam, we used a ground glass diffuser to generate the speckle pattern that illuminates the aperture mask (object). Light transmitted through the object hit a second diffuser, which acted as the turbid medium of interest. Through the shower-curtain effect, the light pattern projected on the front side of the turbid medium can be observed on the back side of the turbid medium. To record such a pattern, one can either place a camera in the plane of the turbid medium, or, as we did, image the plane of the turbid medium onto a camera with a lens. After recording 3000 frames while shifting the first diffuser, we Fourier transformed, processed, and summed each frame to yield the autocorrelation of the object. At last, we reconstructed the original object from the autocorrelation using Fienup phase retrieval algorithm.
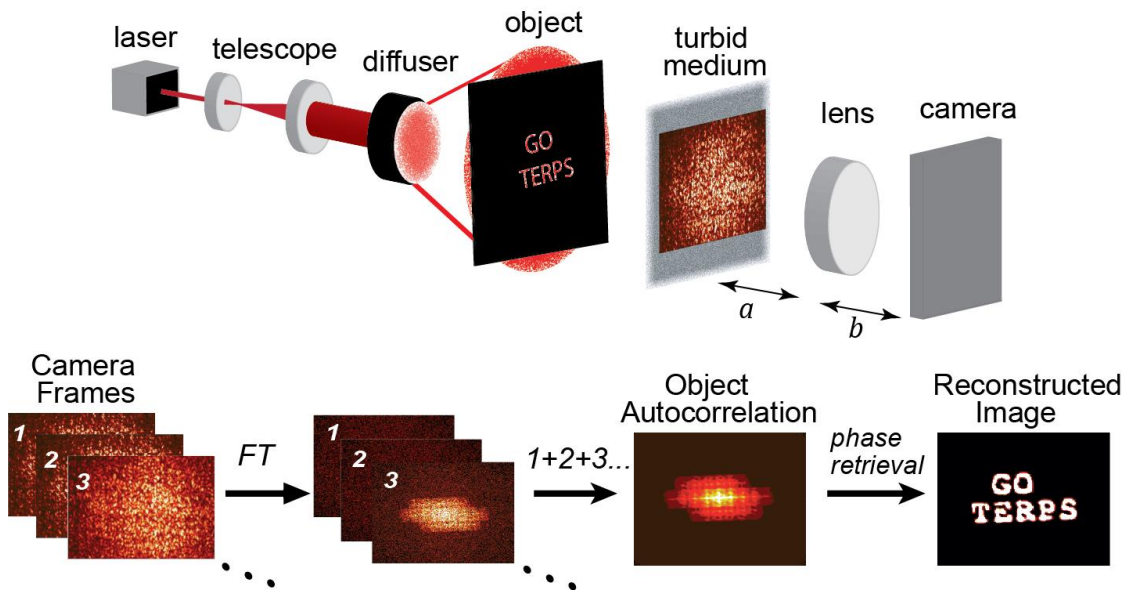
Figure 2.2. Upper panel: Experimental setup: an expanded laser beam is diffused by a first diffuser; the scattered light passes through the object and generates a complex pattern on a turbid medium. The plane of the turbid medium is imaged onto the camera with a lens of focal length f ($1/a + 1/b = 1/f$). Lower panel: Data processing and experimental results: the acquisition procedure is repeated many times while the first diffuser is shifted. For each frame, we performed a Fourier transform, DC filtering, and averaging to obtain the autocorrelation of the object. From the autocorrelation, we retrieved the object with a phase retrieval algorithm.

2.3 Experimental results

2.3.1: Imaging through thick biological specimens:

To present our imaging performances through biological tissues, we used a dense nuclear cataract from ex vivo rabbit eyes and a 0.8-mm-thick chicken breast tissue. Both these turbid media are visually opaque, i.e., standard systems cannot image objects hidden behind them [Figs. 2.3(a) and 2.3(b)]. For our experiment, we used objects printed on a photolithography mask, with the smallest features ~10 μm [Figs. 2.3(c) and 2.3(d)]. We illuminated the objects with a speckle pattern, as

previously described, and recorded the transmitted light at the back surface of the turbid medium. The conventional imaging system yielded no information about the objects [Figs. 2.3(e) and 2.3(f)]; instead, our reconstruction process accurately retrieved the shape of the original objects [Figs. 2.3(g) and 2.3(h)]. Our protocol can be applied to image through thicker scattering samples; the inset in figure 2.3(h) shows the reconstruction of the same object as in figure 2.3(d) through a 3.3 mm chicken breast tissue.
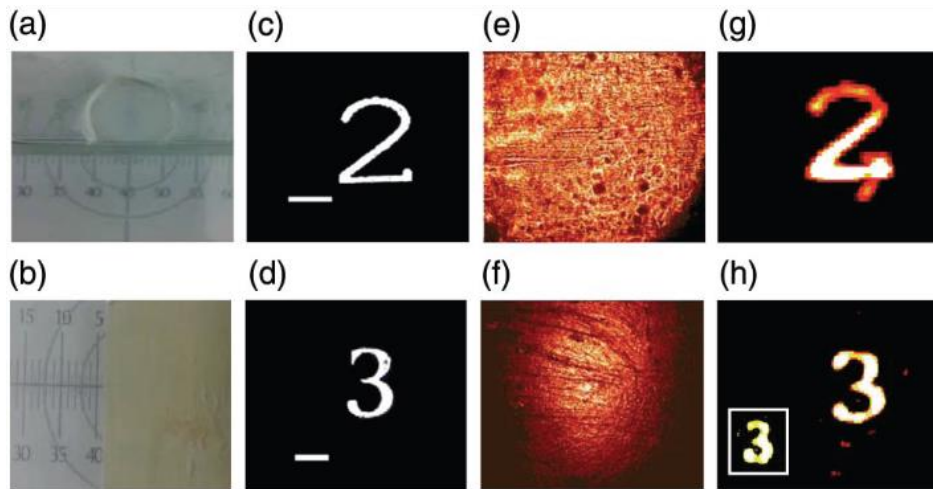
Figure 2.3. Imaging through biological turbid media. (a) and (b) Photograph of a ruler placed 0.5 in hidden behind a cataract and an 0.8-mm-thick chicken breast tissue. (c) Object mask used for imaging through cataract. Scale bar, 200 μm. (d) Object mask used for imaging through the chicken tissue. Scale bar, 100 μm. (e) and (f) Average of the recorded images as seen through the cataract and the tissue (distances 80 and 100 mm, respectively). (g) and (h) The reconstructed images as obtained after correlography analysis. The inset in figure 2.3(h) shows the reconstruction of the object when placed behind 3.3 mm of chicken breast tissue (the object was 600 mm behind the tissue).

2.3.2: Imaging through dynamic turbid medium:

A key feature of the shower-curtain phenomenon is that any phase aberration introduced in the plane of the turbid medium does not affect the intensity pattern recorded if that plane is imaged

onto a camera. Thus, in our scenario, the turbid medium can be effectively thought of as a screen where images or other light patterns are projected and recorded. As a result, the turbid medium is not required to be stable during the imaging process; in fact, operating in an imaging configuration, dynamic scattering processes occurring at the turbid medium plane do not contribute to the degradation of the point-to-point correspondence of the imaging system. To vividly demonstrate this intriguing property, we used a ground glass as a turbid medium, and we rapidly rotated it (37 revs/s) using a commercial fan [Fig. 2.4(a)], yielding greater than 5 m/s linear speed at the pattern location. We used the same object aperture as in the static case [Fig. 2.4(b)]. As expected, neither the single shot of the camera [Fig. 2.4(c)] nor the average of all recorded frames [Fig. 2.4(d)] seemed to provide useful information about the object; however, by adding the processed Fourier transforms of all images and applying the phase retrieval algorithm, we could reconstruct a clear image of the object [Fig. 2.4(e)]. The speckle decorrelation time introduced by the turbid medium in this scenario is shorter than 1 μs, which is several orders of magnitude faster than the camera acquisition time.
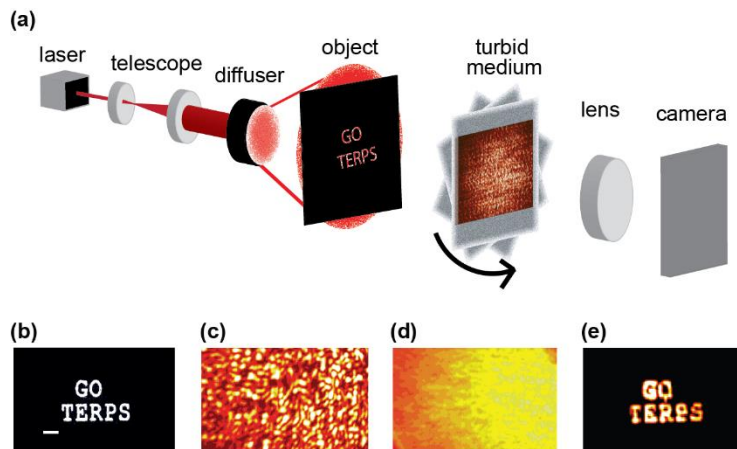

Figure 2.4. Imaging through dynamic turbid media. (a) Experimental setup: an expanded laser beam is scattered by a ground glass diffuser and the resulting speckle pattern illuminates an object. The light transmitted through the object propagates 190 mm and goes through a rapidly rotating

ground glass. We used a camera to record the light pattern on the rotating ground glass. (b) Object. Scale bar, 200 μm. (c) Representative single shot as recorded by the camera. (d) Average of 3000 camera frames of different speckle realizations. (e) Reconstructed image

2.3.3: Imaging around the corner:

Beyond transmission configurations, we demonstrated our imaging protocol in the "look around the corner" geometry. We used a similar setup to Fig. 7, but we collected the light scattered off the turbid medium [Fig. 2.5(a)]. High-quality image reconstructions were obtained also in this configuration [Figs. 2.5(b) and 2.5(c)].
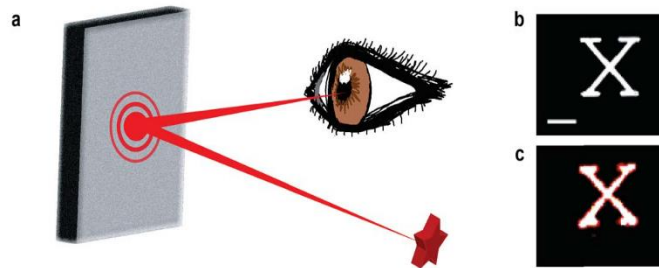
Figure 2.5. Imaging around the corner. (a) In the reflection configuration, we recorded the light scattered off the turbid medium. For these experiments, as the turbid medium, we used white paper located 150 mm from the object. (b) Object. Scale bar, 200 μm. (c) Reconstructed image.

2.3.4: Different contrast mechanisms:

Furthermore, our imaging protocol can be extended to contrast mechanisms other than transmission. As a proof-of-principle demonstration, we used the object birefringence as the imaging contrast [Fig. 2.6(a)]. To make a birefringent object, we surgically extracted and fixed a bovine cornea; we stained it with picrosirius red (PSR) and attached it to a USAF chart [Fig. 2.6(b)]. The PSR staining of the collagen-rich tissue sample changed the polarization of the

incoming light; therefore, placing two crossed polarizers before and after the object, the recorded pattern was only due to the birefringence contrast, while the light transmitted with no polarization change was effectively suppressed (18 fold). Our imaging protocol was clearly able to reconstruct the shape of the birefringent regions of the object [Fig. 2.6(c)]. We used the same cross-polarized setup to image a bovine retinal tissue sample through a ground glass diffuser. Only light that was scattered by the different features in the tissue was collected by the imaging system, as shown by directly imaging the tissue with standard polarized microscopy [Fig. 2.6(d)]. Also in this case, our reconstruction process was able to retrieve the object shape through the turbid medium [Fig. 2.6(e)].
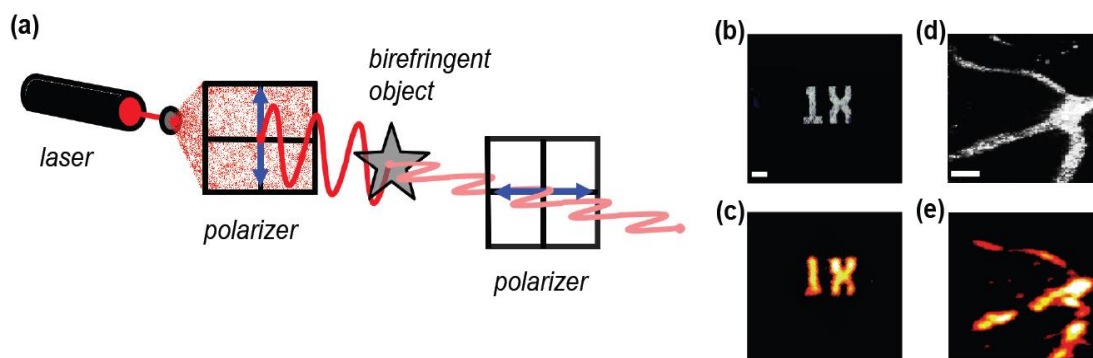
Figure 2.6. Different contrast mechanisms. (a) Schematic principle of the experimental setup. (b) and (c) We placed an object made of fixed corneal tissue between two cross polarizers so that only light that changed polarization went through. The distance between the object and the turbid medium here was 55 mm. (b) Object aperture imaged in free space. Scale bar, 250 μm. (c) Reconstructed image. (d) and (e) Between two cross polarizers, we placed a dried retinal tissue sample so that only light scattered by tissue features went through. The distance between the object and the turbid medium here was 140 mm. (d) Retinal tissue object imaged in free space in a cross polarized configuration. Scale bar, 250 μm. (e) Reconstructed image through turbid medium.

2.4 Discussion and summary

At a fundamental level, the spatial correlations exploited by the shower-curtain phenomenon are governed by the same principles as the ones used in the memory effect (Bertolotti et al., 2012, Katz et al., 2014a). The angular range of the memory effect can be thought of as the maximum numerical aperture through which an object can be observed, and thus provides an upper limit on the spatial frequency cutoff of the shower curtain. We quantitatively demonstrated this correspondence; we measured the memory angular range for increasing number of scattering papers by placing the layers on a rotational stage and plotting the decorrelation curve for each number of scattering papers. The angular width of the memory effect was estimated by the FWHM of the decorrelation plot. We plotted the inverse value of this angle versus the resolution obtained for the same scattering medium when placed right in front of the object and found a strong linear correlation [Fig. 2.7].
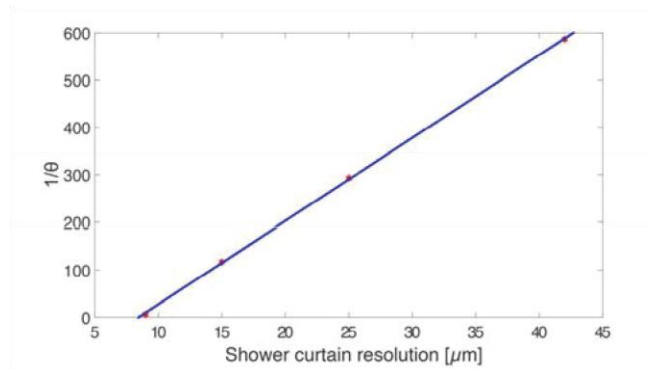
Figure 2.7. The resolution determined by the shower-curtain effect is inversely related to the angular width of the memory effect.

Therefore, the imaging resolution through the scattering layer via shower curtain effect is inversely proportional to the angular range allowed by memory effect. This result confirms that the near-field spatial correlations between front-side and back-side of the turbid medium that are exploited in the shower-curtain effect are due to the same phenomenon that regulates the far-field spatial

correlations exploited in memory effect protocols. For an intuitive understanding, the angular range allowed by memory-effect in a given turbid medium, can be interpreted as the maximum angle (i.e. NA) through which we can see an object with the shower-curtain effect. Hence, in static conditions, image protocols that use the shower-curtain effect will be able to reconstruct objects through the same scattering layers as the pioneering work by Bertolotti et al. (Bertolotti et al., 2012) and Katz et al. (Katz et al., 2014a), with equivalent limitations on resolution and field of view.

However, our protocol uses coherent processing to exploit the shower curtain effect in the Fourier domain, i.e., the features we measure through the scattering layer are the spatial frequencies of the object rather than the object features. Therefore, the scattering medium primarily degrades the field of view (FOV) rather than the resolution of the imaging system. The highest spatial frequency of an object of size D will be: $\sim \frac{z\lambda}{D}$, this frequency has to be larger than R_t which is the smallest resolvable feature through the turbid medium enabled by the shower curtain effect: $\frac{z\lambda}{D} > R_t \rightarrow z > \frac{DR_t}{\lambda}$. And in terms of angular FOV we obtain:

$$\theta \approx \frac{D}{2z} \rightarrow \theta < \frac{\lambda}{2R_t} \qquad (2.3)$$

For a ground glass diffuser, we measured $R_t < 8\,\mu m$, corresponding to FOV $\sim 1.8°$; for the 0.8 mm chicken tissue, we measured $R_t < 20\,\mu m$, corresponding to FOV $\sim 0.7°$. The resolution of the system instead is given by how many Fourier components can be recorded at a high signal-to-noise ratio. Thus, the lens that images the turbid medium plane onto the camera has to provide enough resolution to distinguish R_t and enough field of view to capture the full Fourier spectrum of the object. For a ground glass turbid medium located 35 mm from the object, we obtained a 3 μm resolution corresponding to an effective NA of 0.1 compared to the geometrical 0.16 NA of the

system. Diffraction-limited resolution can be obtained by optimizing the pixel size, speed, and sensitivity of the camera sensor. Working in the Fourier domain may be advantageous because by enlarging the distance between object and scattering layer, thicker media can be handled; we demonstrated this property by imaging an object with 10-μm-sized features behind a 3.3-mm-thick piece of chicken breast tissue (Fig. 2.3(h), inset). However, the ultimate thickness of the scattering medium is limited, as the light-diffusion delay spread within the turbid medium should not exceed the temporal coherence set by the first diffuser.

In dynamic conditions where the turbid medium is moving, and light correlations are degraded, our protocol is markedly different from memory-effect protocols. Three peculiar features (i.e., near-field correlations through the shower curtain, coherent formation of the object Fourier transform, and direct readout of the object Fourier transform in an imaging configuration) contribute to make our protocol nearly insensitive to the motions of the scattering medium.

Being based on the Fourier transform retrieval, however, our method is inherently a coherent technique. Therefore, unlike previous incoherent reconstructions, broadband contrast mechanisms such as fluorescence are difficult to use. This also represents the practical limit on the motion of turbid media that can be handled. To retrieve high-quality Fourier transforms, the single-frame acquisition time should be faster than the speckle decorrelation time of the first diffuser, which in epi-detection configurations may also be a moving biological tissue. With our low-cost camera, we operated in the order of a 10 ms acquisition time, which would already allow imaging without artifacts caused by breathing, saccadic movements or heartbeats. It is straightforward to improve this performance and achieve sub-millisecond acquisition times using a more sensitive camera.

In summary, we demonstrated a speckle correlography protocol based on the shower-curtain effect adapted to the Fourier domain. This enabled imaging through millimeter-thick tissues, insensitive to turbid medium motion. Using light power levels safe for in vivo tissue applications and low-cost optical components, we demonstrated imaging performances that are promising for biomedical applications such as imaging the retina through a cataract or the back of the ear through the tympanic membrane.

Chapter 3

Incoherent imaging through scattering medium using memory-effect based deconvolution[*]

In many scenarios, an incoherent imaging approach is needed such as in fluorescent microscopy. In this chapter we introduce a method to image incoherently through scattering materials. We demonstrate a novel microscopy technique enabled by the optical memory effect that uses a deconvolution image processing and thus it does not require iterative focusing, scanning or phase retrieval procedures. We show that this newly established ability of direct imaging through turbid media provides fundamental and practical advantages such as three-dimensional refocusing and unambiguous object reconstruction. We further demonstrate that this method provides an improved resolution below the diffraction-limit.

---

[*] The results of this chapter were part of a peer reviewed publication, *Scientific Reports* 6, 2016

3.1: Principle

Deconvolution processing is a well-established and widely used technique in astronomy (Starck et al., 2002), microscopy (Sarder and Nehorai, 2006) as well as non-optical imaging (Taxt, 1995). It relies on the linear properties of imaging systems for which the imperfect image recorded by an instrument can be written as the convolution of the perfect object function with the point spread function (PSF) of the optical system, i.e. its response to a point source. Measuring or estimating the PSF of the system, one can restore, i.e. deconvolve, a high-quality image from the measured one (Sibarita, 2005, Pawley, J. 2010). The process relies on the following mathematical concept: the camera image is a convolution of the PSF and the object: $I_{camera} = PSF \otimes Object$. Taking the Fourier transform of both sides yields: $FT(I_{camera}) = FT(PSF) \cdot FT(Object)$ where we applied the convolution theorem to simplify the right-hand side. Dividing both sides by $FT(PSF)$ and taking the inverse Fourier transform one can obtain the Object. Hence, given the image acquired by the camera and the PSF, the deconvolution operation can yield better resolution than the diffraction limit and provide significant improvements in image contrast thanks to the available information of the system's response (Schermelleh et al., 2010). Yet, this process is very susceptible to noise as the high spatial frequencies have small amplitudes and therefore division by the $FT(PSF)$ involves divisions by numbers close to zero. To overcome this drawback, in practice iterative algorithms are applied to estimate the object form the blurred image and the PSF, these algorithms are less affected by intensity fluctuations, but they involve longer and heavier computational processes.

While the power of the deconvolution operation has been known for decades and is ubiquitously used to correct for aberrations in optical systems, it has never been exploited for imaging through scattering media, because the PSF is known to present dramatic spatial variations

due to scattering. However, we show here that when a turbid medium is within an imaging system, the correlation properties of the memory effect predict a spatially-invariant PSF within the memory-effect angular range. This is due to a fundamental property of the memory effect, i.e. that when a beam impinging upon a turbid medium is tilted, the generated speckle pattern acquires a linear phase gradient, i.e. it is only shifted but not distorted within the optical system. Thus, within the memory-effect range, deconvolution microscopy can effectively be used for high-quality image reconstruction through the scattering layer.

3.2: Method

We demonstrated our novel imaging technique experimentally with the setup in Figure 3.1a. We illuminated an object aperture (e.g. Fig. 3.1b) with incoherent illumination and imaged it onto a low-cost CMOS camera using a single-lens (f=250 mm) imaging system aligned for 1.4 magnification. Within the imaging system, we placed a scattering medium (120-grit ground glass diffuser) so that the recorded image pattern was totally scrambled (Fig 3.1c). We then applied a standard deconvolution operation (150 iterations of a Richardson-Lucy (R-L) algorithm (Richards.Wh, 1972, Lucy, 1974)) using the PSF of the system measured by replacing the object with an iris of typical size 10-50 µm (Fig 3.1d). This yielded an accurate reconstruction of the object hidden behind the scattering medium (Fig 3.1e).
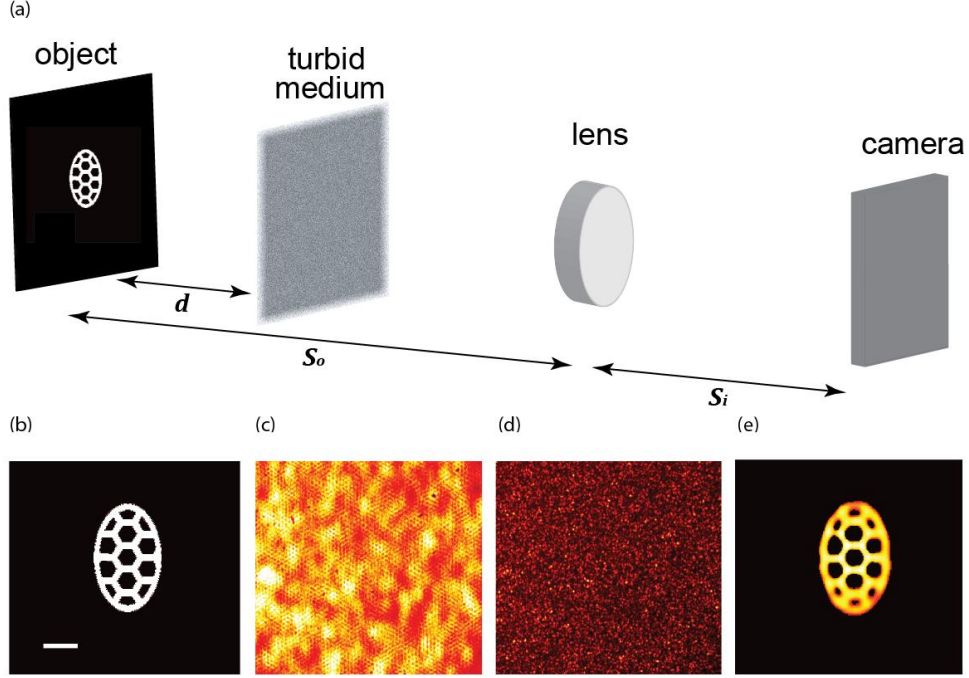
Figure 3.1: (a) Optical setup. A mask is placed a distance (d=16cm) behind a 120 grit ground glass diffuser. The plane of the object was imaged onto a CMOS camera using a 250mm focal length lens. (b) Image of the object without turbid medium. Scale bar, 200µm. (c) Scrambled image as recorded through the ground glass. (d) PSF of the overall setup recorded by replacing the object with an iris. (e) Reconstructed object after deconvolution.

The performances of our imaging system can be analyzed using Huygens-Fresnel field propagation. The field at the image plane in the system in Fig. 3.1a can be written as:

$$E(\rho_I) = A \iiint E(\rho_O) e^{\frac{ik}{2d}(\rho_T - \rho_O)^2} P(\rho_T) T(\rho_T) e^{\frac{ik}{2(S_O - d)}(\rho_L - \rho_T)^2} L(\rho_T) e^{\frac{ik}{2S_I}(\rho_I - \rho_L)^2} d\rho_O d\rho_T d\rho_L \quad (3.1)$$

Where $\rho_O, \rho_T, \rho_L, \rho_I$ are the transverse coordinates in the plane of object, turbid medium, lens and image (camera) respectively. Using an explicit pupil function P as limiting aperture of the optical system, all the integrals can be performed on an infinite interval without loss of generality. We denoted the generic complex function of the turbid medium by $T(\rho_T)$, the lens operator by $L(\rho_T) = e^{-\frac{k}{2f}\rho_L^2}$, and a proportionality constant by A. The distances from the object to turbid

medium and lens are d and S_O respectively; the camera is located a distance S_I from the lens so that the Gaussian thin lens relation $\frac{1}{S_O} + \frac{1}{S_I} = \frac{1}{f}$ is followed.

Performing the integrals over the lens plane and applying the thin lens equation, Equation (1) simplifies to:

$$E(\rho_I) = A \iint E(\rho_O)e^{\frac{ik}{2d}\rho_O^2}P(\rho_T)T(\rho_T)e^{-\frac{ik}{d}\rho_T\left(\rho_O+\rho_I\frac{S_O}{S_I}\right)}d\rho_O d\rho_T \qquad (3.2)$$

Recognizing the Fourier transform integral: $\tilde{T}(\rho_O,\rho_I) = \int P(\rho_T)T(\rho_T)e^{-\frac{ik}{d}\rho_T\left(\rho_O+\rho_I\frac{S_O}{S_I}\right)}d\rho_T$ the intensity in the camera plane can be simplified to:

$$I(\rho_O) = \int |E(\rho_O)|^2 |\tilde{T}(\rho_O,\rho_I)|^2 d\rho_O \qquad (3.3)$$

Thus, the PSF of the system, obtained by using a delta function $\delta(\rho_O - \rho_{iris})$ in the object plane, is given by:

$$PSF(\rho_I) = \left| \int P(\rho_T)T(\rho_T)e^{-\frac{ik}{d}\rho_T\left(\rho_O+\rho_I\frac{S_O}{S_I}\right)}d\rho_T \right|^2 \qquad (3.4)$$

Therefore, the PSF of the system is the convolution of the pupil function of the imaging system with no turbid medium and the turbid medium function. With no turbid medium (i.e. T=1), the system reduces to a standard imaging system with magnification $M = \frac{S_O}{S_I}$. Importantly, it is clear from Equation 3.4 that a linear phase gradient acquired by $T(\rho_T)$, as the one occurring within the memory effect angular range, will yield a spatially-invariant PSF for the overall system.

To experimentally demonstrate the spatial invariance of the PSF, we replaced the object in the setup of Fig. 3.2a with a small iris and translated the iris laterally across the object plane behind a layer of opaque tape (50 um). Figures 3.2 (a-c) show three representative images corresponding to three different locations of the iris. It is visually apparent that the PSF patterns are shifted but

not distorted, as predicted. To quantify the PSF variation at different locations within our field of view we measured cross-correlations of the different patterns and compared it to their autocorrelation. As shown in figure 3.2 (d), the height of the peak is nearly unaltered proving the invariance of the PSF within the angular range of the memory effect.
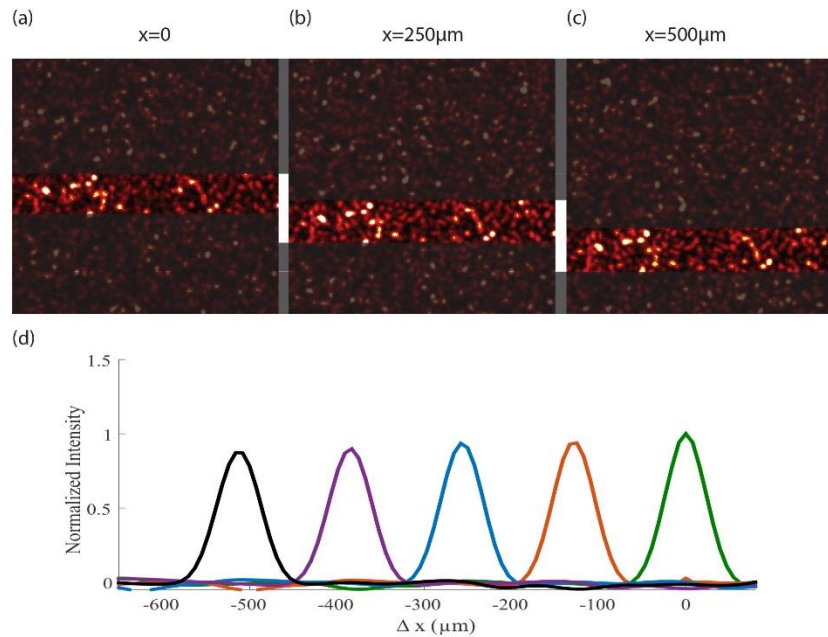
Figure 3.2: (a-c) PSF of the imaging system across the memory-effect field of view, measured by laterally shifting an iris in the object plane. The central area is highlighted to facilitate visualization of the undeformed shifted pattern. (d) Comparison of autocorrelation and cross correlations of different patterns at different iris positions demonstrating nearly unaltered PSFs within the memory-effect field-of-view.

It is interesting to compare these results with the theoretical ones predicted by equation 1.3. To do that we need to account for the anisotropic parameter g which is not considered in the derivation of equation 1.3. To do so we refer the reader to the work of Schott et al. (Schott et al., 2015) where the authors examin the effect of anisotropic scattering on the memory effect angular range. Following their findings here we define the effective thickness of the scatterign layer L_{eff} to be the thickness which corresponds to an isotropic medium with the same angular memory effect range as the sample of interest (i.e. the value that should be used in equation 1.3). For chicken breast tissue this value is tipically about 30 time smaller than the actual thickness, and

since the tape we used in figure 3.2 has a similar properties we shell assume also here $L_{eff} \approx$

$^L/_{30}$. Substituting the following values $L_{eff} = {}^L/_{30} = 1.7 \ \mu m, k = \frac{2\pi}{0.5}, \Delta\theta = \frac{\Delta x}{d} = \frac{0.5 \ mm}{45 \ mm}$,

into equation 1.3 we obtain the decorrelation value to be $C(\Delta\theta) \approx 0.98$, which means the

correlations are yet hgihly preserved as seen from the minor decrease of the peak in figure

3.2(d). However, when 20 layers of tape are attached to generate a 1 mm thick layer, the

decorrelation evolves rapidely so even when $\Delta x = 150 \ \mu m$ the theoretical value from

equation 1.3 drops to $\approx 54 \ \%$ in agreement with the experimental results shown in figure 3.3.
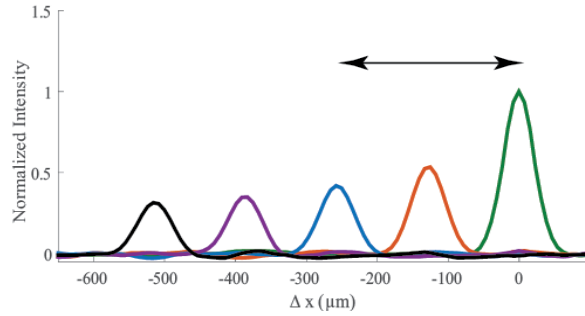
Figure 3.3: Comparison of autocorrelation and cross correlations of different patterns at different iris positions through 20 layers of tapes (L=1 mm) demonstrating a rapid decrease of the pattern correlation.

3.3: Experimental results

3.3.1: Sub-diffraction resolution

We show that deconvolution microscopy through turbid media retains the same powerful

properties as if there were no turbid media such as sub-diffraction resolution. For this, we used an

object (Fig. 3.4a) whose features are smaller than the optical resolution of our imaging system. In

a standard configuration, i.e. with no turbid medium, the image appeared blurred due to the limited

resolution of the imaging system (Fig. 3.4b). As we placed a diffusive tape in front of the object

(d=10cm), the image appeared heavily scrambled (Fig. 3.4c). However, by deconvolving the

scrambled image with the system PSF (in Fig. 3.4e), the image of the object was reconstructed and

sharp (Fig 3.4d). To better visualize the resolution improvement, we show an averaged line plot across the imaged object with standard imaging configuration against the reconstructed image via deconvolution through turbid medium in Fig. 3.4f. Using a point-like object, we have directly quantified that our protocol applying 150 R-L iterations yields a ~1.8-fold resolution improvement below diffraction limit consistent with previous demonstrations of resolution enhancement by deconvolution processing in standard optical systems (Catlin and Dainty, 2002, Christou et al., 2004).
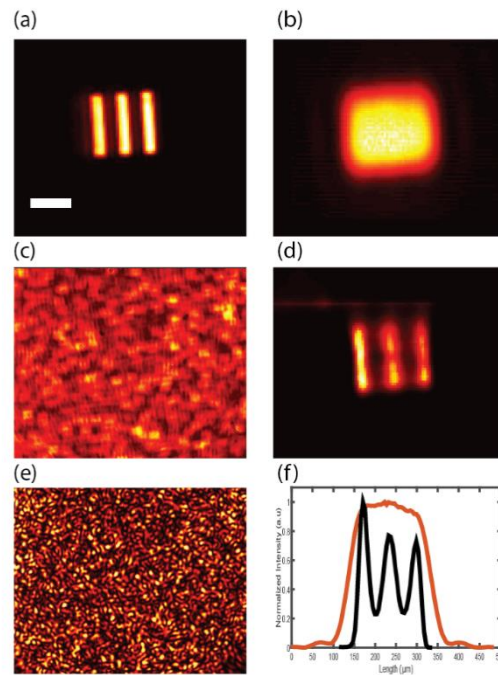
Figure 3.4: Sub-diffraction imaging through turbid medium. (a) Imaged object. Scale bar, 100 µm. (b) Blurred image of the object with no turbid medium and a standard imaging system of low numerical aperture. (c) Image of the object hidden behind a diffusive tape. (d) Image reconstruction by deconvolution. (e) PSF of the imaging system through the diffuser. (f) Averaged intensity line plot of (b) and (d) visualizes the enhanced resolution of the reconstructed image (black) compared to standard imaging (red).

3.3.2: 3D imaging

Another important feature of deconvolution microscopy is its three-dimensional sectioning capability, or its ability to re-focus out-of-plane images with results that in certain conditions can rival confocal microscopy (McNally et al., 1999). This interesting feature is maintained in our protocol through turbid media and represents a marked difference over previous memory-effect methods characterized by extended depth of focus (Katz et al., 2014a). To demonstrate our reconstruction is sensitive to the axial location of the object we placed the object 5 mm away from the in-focus plane. In a standard imaging system without turbid medium, the image appeared blurred, as expected (Fig. 3.5a). The turbid medium placed at a distance d=5cm from the object scrambled the image completely (Fig. 3.5b). Next, we measured the three-dimensional PSF (3D-PSF) by placing an iris at different axial planes. By performing the deconvolution with the 3D-PSF function, we demonstrated successful reconstruction of a high quality image as well as 3D refocusing (Fig. 3.5c). Interestingly, also the decorrelation of the PSF along the depth axis may introduce an optical sectioning effect (Park et al., 2009); however, this effect was not exploited in our experiment because in our setup the decorrelation full width at half maximum (FWHM) was 1.5mm, five times larger than the depth of focus of the optical system (0.3mm).
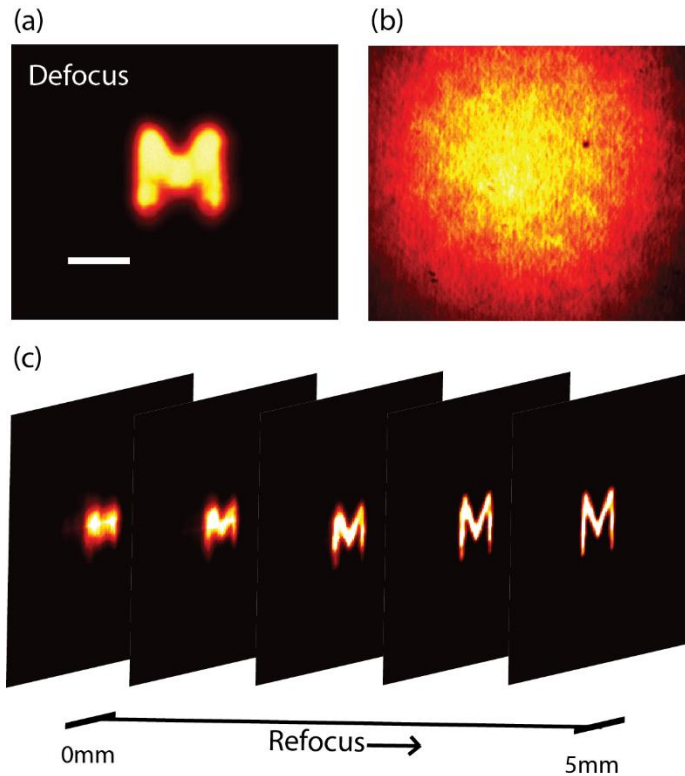
Figure 3.5: (a) Defocused image of an object as seen through an imaging system (with no turbid medium) focused on a plane 5mm away from the location of the object. Scale bar, 200µm. (b) the image is scrambled when a 120-grit ground glass diffuser is placed in front of the object. (c) Refocusing of the out-of-plane image through a turbid medium by deconvolution with the PSF measured at different axial locations.

3.3.3: Large field-of-view illumination

As in standard deconvolution procedures, noise is the practical limiting factor on the quality of the image reconstruction. When performing deconvolution imaging through turbid media based on memory effect, additional noise sources are introduced with respect to traditional free-space deconvolution imaging. For example, the components of the light emitted by the object at large angles will not be confined to the memory effect range and thus will result in an uncorrelated DC noise term. In our experiment, this noise term was minimized using a field stop within the optical

system. Similarly, DC noise terms will be introduced if objects that are larger than the memory-effect field of view are illuminated, as they will produce uncorrelated patterns within the reconstruction procedure. To quantitatively analyze this effect, we recorded many uncorrelated speckle patterns (PSFs) produced by point sources placed at distant locations within the object plane. As expected, the deconvolution of each PSF with itself gives back a noiseless reconstruction of the individual point source; instead, as many uncorrelated patterns are added or simultaneously recorded, the signal to noise ratio (SNR) of the deconvolution reconstruction degrades. We quantified the SNR to remain greater than 1 with up to 40 uncorrelated patterns. This hints at an interesting feature of our protocol: deconvolution processing is robust against illumination outside the memory-effect field of view in the object plane, which instead is known to degrade phase-retrieval procedures. To demonstrate this feature experimentally, we used a turbid medium made of twenty 50µm-thick layers of scattering tape and illuminated a large object placed 45mm behind the medium (Fig. 3.6a). The field of view (FOV) of the memory effect (estimated at the FWHM) was 200mdeg (corresponding to the white circle in Fig. 3.6a). Behind the turbid medium the object was completely blurred (Fig. 3.6b), as expected. After deconvolving the image with the measured PSF, we reconstructed the desired part of the object (Fig. 3.6c). While the illuminated area was 20 times larger than the one allowed by the memory effect, the reconstructed regime falls within the area dictated by the memory effect FOV.
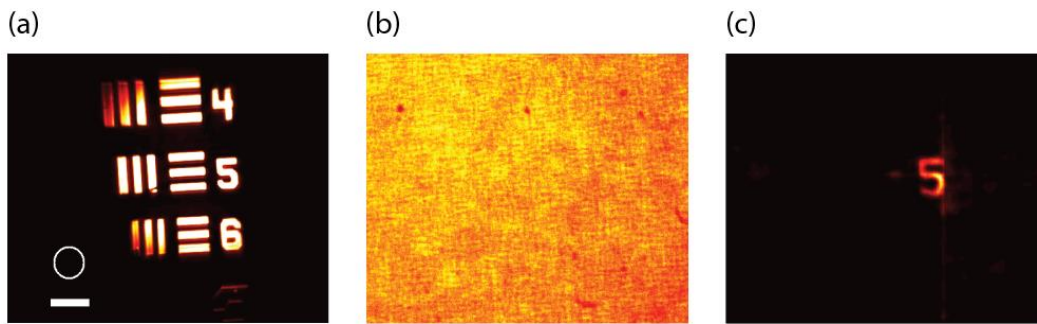
Figure 3.6: Large FOV illumination: (a) The object illuminated in the experiment (scale bar, 200μm), the white circle indicates the FOV permitted by the memory effect (this experiment was performed using a 632nm CW laser). (b) The blurred object as seen through a scattering layer of 20 tapes (total thickness of 1mm). (c) The reconstruction of the object after applying 400 deconvolution iterations, only a small regime corresponding to the memory effect range was restored.

3.4 Discussion and summary

Thus, we have demonstrated a new imaging approach that enables to perform three-dimensional imaging below the diffraction limit through turbid media. Compared to other memory-effect based modalities, our new protocol has similar limits in terms of scattering layers to go through (Bertolotti et al., 2012, Katz et al., 2014a, Yang et al., 2014), however, those modalities have an infinite DOF and lack the ability to perform a three dimensional sectioning (Katz et al., 2014a). Moreover, phase retrieval algorithms which are used in these studies impose strict limitations on the complexity of the objects that can be imaged and do not guarantee convergence to an unambiguous correct solution (Shechtman et al., 2015, Liberman et al., 2016); this is not a concern in our imaging protocol. In order to achieve these features, though, our protocol requires to have information about the PSF of the scattering medium; in this respect our protocol should be compared to other methods that pre-characterize the turbid medium. These techniques have flourished in the past decade (Horstmeyer et al., 2015). Measuring the transmission matrix to correct for sample induced aberrations as well as iterative focusing to obtain the desired shaped wave-front have been successfully demonstrated in highly scattering media (Popoff et al., 2010a, Katz et al., 2012). However, these techniques generally have minutes-long acquisition times as they require either an iterative process or multiple acquisitions. A faster wave-front sensing and shaping modality is optical phase conjugation (OPC) in which the scattered light field is recorded

and reversed to compensate for the aberrations of the medium (Yaqoob et al., 2008, Cui and Yang, 2010). Recently, the time needed for focusing light through scattering medium using OPC/DOPC was reduced to several milliseconds (Liu et al., 2015, Wang et al., 2015a). However, for imaging purposes scanning across the object plane is often needed which increases the measurement time (Hsieh et al., 2010, Wang et al., 2012). In contrast, here we showed a wide-field imaging modality where it is sufficient to record a single shot of the scattered intensity, and the image is obtained by deconvolution processing.

In conclusion we have demonstrated that the fundamental principles of the optical memory effect can be effectively used to perform deconvolution microscopy of objects hidden behind visually opaque materials thus providing sub-diffraction three-dimensional imaging. As we used a basic deconvolution algorithm, our technique is expected to significantly improve with more sophisticated deconvolution procedures (Starck et al., 2002). Our imaging method can be extended to epi-detection configurations for practical applications by using established methods to estimate the system point spread function either by a blind process (Kundur and Hatzinakos, 1996) or using guide-stars embedded in the medium at the object plane (Horstmeyer et al., 2015).

Chapter 4

Coherent focusing through scattering medium: a fundamental trade-off between speckle size and intensity enhancement[*]

Many optical modalities operate by scanning a focal point through a sample (e.g. confocal and two-photon microscopy) rather than in a wide-field configuration as we have discussed in chapters 2 and 3. In this chapter, we study the method of focusing light through a highly scattering material by modifying the phase profile of the illuminating beam which has attracted a great deal of attention in the past decade. We report on a tradeoff between two seemingly independent quantities of critical importance in the focusing process: the size of the focal point obtained behind a scattering medium and the maximum achievable brightness of such focal point. We demonstrate that the intensity enhancement limitation becomes dominant when the focusing plane gets closer to the scattering layer thus limiting the ability to obtain tight focusing at high contrast, which has direct relevance for the many applications exploring scattering materials as a platform for high resolution focusing and imaging.

---

[*] The results of this chapter were submitted for publication and are under peer review.

4.1 Background

Light-based imaging and focusing methods have been historically limited to transparent materials or shallow depths due to multiple light scattering in complex media (Ntziachristos, 2010). Traditional methods to combat distortions by measuring and projecting complementary phase maps (e.g. adaptive optics) (Tyson, 2015, Beckers, 1993) have been able to compensate for mild aberrations due to imperfect optical elements, atmospheric turbulence and distortions within the eye (Beckers, 1993, Roorda and Williams, 1999, Roorda et al., 2002). Yet, they are largely ineffective in highly scattering media due to the numerous amount of degrees of freedom involved and the short scattering mean-free-path. Starting with the pioneering work by Vellekoop and Mosk (Vellekoop and Mosk, 2007), the past decade has seen tremendous progress in our ability to focus a laser beam through a highly scattering material. In this process the "focal point" is obtained by tailoring the relative phases of light in the scattering medium to constructively interfere at a point of interest. This can be achieved either by iteratively modifying the incident beam phase profile with a spatial light modulator (SLM) (Vellekoop and Mosk, 2007, Vellekoop, 2015, Vellekoop and Mosk, 2008b), by directly measuring the optical transmission matrix of the scattering medium (Popoff et al., 2010b, Conkey et al., 2012, Choi et al., 2011) or by recording the field fluctuations induced by the medium (Yaqoob et al., 2008, Wang et al., 2015a). Interestingly, a focal point can be obtained even though the controllable elements needed to perfectly counteract scattering deep within opaque samples is still much larger than those provided by the SLM. This rather surprising ability is due to the relative phase adjustment process as opposed to the absolute correction obtained by traditional adaptive optics.

Delivering light through disordered materials has attracted a great deal of interest for diverse applications such as deep-tissue focusing (Liu et al., 2015), optogenetic modulations (Ruan

et al., 2017), imaging of hidden objects (Katz et al., 2012, Hsieh et al., 2010) and high resolution focusing/microscopy (Van Putten et al., 2011, Jang et al., 2018, Leonetti et al., 2018, Di Battista et al., 2015). The underlying concept shared by these works is that the combination of a scattering medium with spatially-resolved control of the beam phase profile can effectively work as a lens. Several enabling features of such "scattering lens" systems have been described such as super-resolution focusing (Park et al., 2013), versatile focal length and structural compactness (Kamali et al., 2016, Antipa et al., 2018). However, the practical features and limitations of the focusing capabilities of "scattering lenses" are not fully understood. Addressing this question, here we report on a tradeoff between the size of the smallest speckle (serving as focal point) that can be obtained behind a scattering medium and the brightness of such focal point achieved via intensity enhancement. We present a theoretical derivation and experimental demonstration that as the focal plane gets closer to the scattering material leading to smaller speckle size, the intensity enhancement of the focal point within this plane is compromised. We show that this intrinsic limit imposes practical constraints on focusing protocols, as it effectively limits the size of a focal point enhanced through a scattering layer, and/or sets an upper-bound to the intensity flux delivered to a given location within a scattering medium. Our study refers to scenarios of highly scattering materials in which the number of controllable elements (i.e. SLM pixels) is much lower than the one needed to produce a perfect complementary phase map and therefore a focal point is obtained by aligning the incident phase.

The intensity enhancement at a point behind a scattering layer (i.e. the ratio between optimized focus intensity and average background) for a monochromatic coherent light has been previously described as (Vellekoop and Mosk, 2008b):

$$I_{enhancement} = \gamma N \qquad (4.1)$$

where N is the number of controllable degrees of freedom on the phase profile of the illuminating beam and γ is an experimental scaling factor. For polychromatic light sources the enhancement is reduced by the number of independent frequency components (van Beijnum et al., 2011, Paudel et al., 2013, Hsu et al., 2015, Andreoli et al., 2015).

The enhancement in Eq. (1) can be understood as follows: consider N uncorrelated fields of amplitude E_o propagating towards a plane. The amplitude of the field at the plane will be $E_o\sqrt{N}$ since the fields are not correlated. If the phase of these fields is adjusted to constructively interfere at the said plane the field amplitude will be enhanced to E_oN, i.e. the enhancement from the uncorrelated scenario is $\sqrt{N}$. Accordingly, the intensity enhancement is the square of the field enhancement and is therefore proportional to the number of propagating fields N. The pre-factor γ depends on several experimental parameters such as the operation mode of the SLM, the sensitivity of the camera to small intensity changes, the noise level throughout the enhancement process and the stability of the scattering medium (Anderson et al., 2014, Vellekoop, 2015, Yılmaz et al., 2013).

Here we find that the intensity enhancement is not generally constant when focusing light behind a scattering medium and that Eq. (4.1) represents the upper limit of intensity enhancement that can be reached. We derive a general expression for intensity enhancement in terms of the fundamental characteristics of the scattering phenomenon (e.g. scattering divergence angle, density of scattering elements, beam spatial coherence). Importantly, we find that these scattering properties introduce severe limitations as the focusing plane gets closer to the scattering layer thus compromising the ability to enhance the intensity of a focal point when high resolution is desired.

4.2 Analytical derivation

Let's consider the general scenario to achieve an enhanced focal point P at a plane located a distance z from a scattering layer. To maximize intensity at point P; a phase map of linear dimension D is projected by an SLM onto the scattering layer and is optimized using a continuous sequential algorithm (Vellekoop and Mosk, 2008a) (Fig. 4.1).
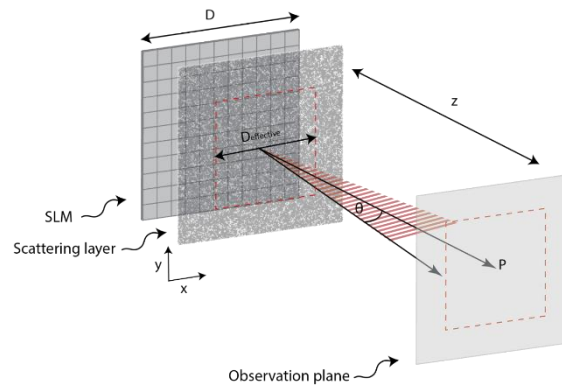
Figure 4.1: Schematics of a general procedure to form a focal point at location P in a plane displaced by the axial distant z. The SLM surface is imaged on a scattering layer to spatially control the phase profile of the incident beam.

Because the scattering process is characterized by a divergence angle θ, light diffused by the scattering layer will not be re-directed everywhere; instead, scattering will re-direct light within a cone of angle θ centered around the normal to the scattering plane (Fig. 4.1). Locations on the scattering layer for which the scattering cone does not include point P will not contribute to the enhancement process. Thus, only a portion of the illuminated area will contribute to the intensity enhancement. Accordingly, for every experimental scenario, we can define an effective area $A_{effective}$ which contributes to the intensity at point P. To quantify $A_{effective}$, we model the illumination plane as a collection of scattering point sources and assign a weight factor to each point based on their effective contribution to the intensity of focal point P. Specifically, we can

assume that each scattering point source generates a beam with a transverse gaussian profile of width determined by the scattering angle θ and by the propagation distance z (i.e. with standard deviation $z \cdot tan(\theta)$). The effective area is the weighted integral of all the scattering point sources:

$$A_{effective} = \int_0^D \int_0^D e^{\frac{-(x^2+y^2)}{2(z \cdot tan\theta)^2}} \, dxdy \quad (4.2)$$

where x, y are the spatial coordinates in the plane of the scattering layer (i.e: $z = 0$). In the limit of large distances from the scattering layer, i.e. for $z \to \infty$, the integration of Eq. (4.2) yields $A_{effective} = D^2$, i.e. all SLM pixels equally contribute to the optimization process. This is the ideal situation described by Eq. 4.1. For finite distances from the scattering layer, the integration of Eq. (4.2) can be solved analytically by substitution, $\tilde{x} \ (\tilde{y}) = x \ (y) \cdot \frac{1}{\sqrt{2} \cdot z tan(\theta)}$, to give:

$$A_{effective} = \frac{\pi}{2} \cdot (z \cdot \tan\theta)^2 \cdot \left[erf(\frac{D}{\sqrt{2} \cdot z \cdot \tan(\theta)}) \right]^2 \quad (4.3)$$

Thus, only SLM pixels that fall within the effective illumination area will contribute to the enhancement. This leads to the general form of Eq. (1):

$$I_{enhancement} = \gamma N \cdot \frac{A_{effective}}{A} \ = \gamma N \cdot \frac{\pi}{2D^2} \cdot (z \cdot \tan\theta)^2 \cdot \left[erf(\frac{D}{\sqrt{2} \cdot z \cdot \tan(\theta)}) \right]^2 \quad (4.4)$$

In summary, the ideal enhancement would be reached in perfectly isotropic scattering conditions where the light is distributed equally over a solid angle of 2π after the scattering medium. Instead, even though the intensity distribution of the SLM pattern projected onto the scattering layer is uniform, the finite divergence angle of scattering phenomenon decreases the contribution of peripheral locations. The intensity enhancement can be interpreted as arising from a radially degrading intensity distribution, which directly affects both the focal intensity and the effective

numerical aperture. Let's analyze the behavior of the intensity enhancement as a function of the unitless parameter: $U = \frac{D}{\sqrt{2} \cdot z \cdot \tan(\theta)}$:

$$I_{enhancement} = \gamma N \cdot \frac{\pi}{4} \cdot \left(\frac{1}{U}\right)^2 \cdot [erf(U)]^2 \qquad (4.5)$$

We note two limits: $\lim_{U \to \infty} \left[\frac{\pi}{4} \cdot \left(\frac{1}{U}\right)^2 \cdot [\text{erf}(U)]^2\right] = 0$, $\lim_{U \to 0} \left[\frac{\pi}{4} \cdot \left(\frac{1}{U}\right)^2 \cdot [\text{erf}(U)]^2\right] = 1$. The first limit occurs for focal planes very close to the scattering layer, i.e. $z \ll D$. Under these circumstances, the effective illumination area vanishes and the enhancement approaches zero (our derivation, though, does not consider the evanescent field and is restricted to $z > \lambda$). The second limit refers to when the focal plane is far from the scattering layer. In this case, the effective illumination area is the entire illumination area, and the enhancement approaches the optimal γN value. Interestingly, this limit can be expressed as: $\frac{D}{\sqrt{2} \cdot z \cdot \tan(\theta)} \ll 1$ and reduces to

$$z \gg \frac{d \cdot D}{\lambda} \qquad (4.6)$$

where d is the average linear distance between scattering particles and we approximated the scattering angle as $tan(\theta) \approx \theta \approx \frac{\lambda}{d}$ (Giglio et al., 2001) (valid under the condition $d > \lambda$). This limit exactly coincides with the 'far-field' condition for partial coherent light: $z \gg \frac{\Delta\mu \cdot D}{\lambda}$ derived from the propagation of mutual coherence (generalized Van Cittert- Zernike theorem (Goodman and Haupt, 2015, Cerbino, 2007, Edrei and Scarcelli, 2016b)), where $\Delta\mu$ is the coherence length right after the scattering material, which was shown to approach d (Giglio et al., 2001). This relation links the maximum intensity enhancement achievable to fundamental properties of the scattering phenomenon such as the concentration of scattering elements and the beam spatial coherence. Interestingly, while the focal length of scattering lenses has been so far assumed to be

entirely variable (Ryu et al., 2016, Jang et al., 2018), here we find that a 'far-field' condition needs to be met for optimal focusing.

4.3 Experimental results

To experimentally verify our theoretical predictions, we built the setup in Fig. 4.2(a). A polarized expanded laser beam of $\lambda = 660\ nm$ (LaserQuantum) was reflected off the surface of phase-only SLM (Hamamatsu X10468-01). The SLM plane was then imaged on a 600-grit diffuser (Thorlabs) which served as scattering medium. To vary the illumination area, we used a de-magnifying 4-f imaging system, with L1 of focal length 400 mm and L2 of variable focal length (45mm to 3mm). An infinitely corrected imaging system was used after the scattering layer to record a plane of interest (L3 = 0.75 NA, 20X, L4 = 200 mm). The distance between the scattering medium and the observation plane (i.e. the plane of enhancement) was selected by adjusting the translational stage of L3. To enhance a single point beyond the scattering layer, the SLM was divided into 100 macro-pixels, and each pixel was varied individually from 0 to 3π to determine the optimal phase configuration by using the recorded pattern on the camera as feedback (Vellekoop, 2015). This process was repeated for all pixels twice, for a total $\sim 20min$ per enhancement process.
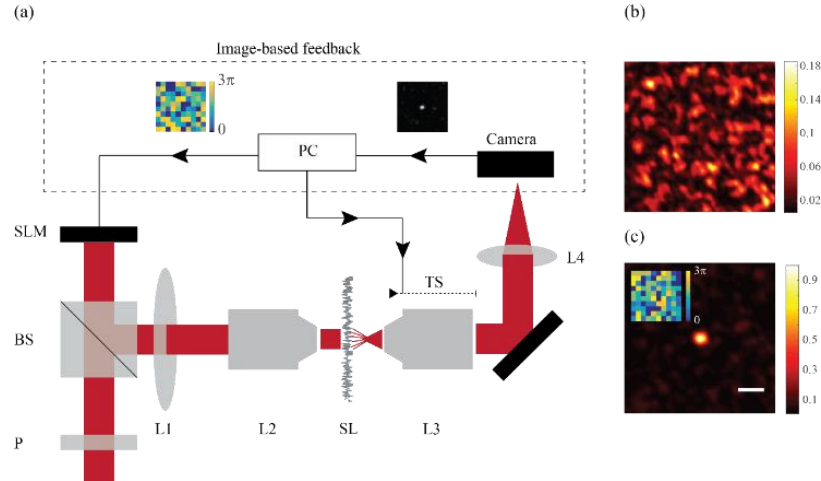
Figure 4.2: (a) Experimental setup: the SLM surface (divided into 100 macro-pixels) was imaged via a 4-f imaging system (L1, L2) onto the scattering layer. A plane behind the scattering layer was imaged onto the camera, and a location within the imaged plane was enhanced by applying a feedback loop to vary the phase map of the SLM. The imaged plane was selected by adjusting the translational stage of L3. (b) Intensity distribution pattern before the enhancement process. (c) Intensity distribution after the enhancement process (scale bar = 5µm). The inset shows the final SLM phase map to which the algorithm converged.

First, we verified our ability to focus light through a scattering material consistently with traditional protocols. We imaged a plane located 1.6 mm after the scattering layer (corresponding to $z \sim 3.2D$) and as expected obtained a speckle pattern, shown in Fig. 4.2(b). We selected a central location in the pattern, performed the sequence to enhance the intensity recorded at that location. After two iterations of every pixel, we arrived at the final intensity distribution presented in Fig. 4.2(c). The number of degrees of freedom controlled by the SLM is orders of magnitude smaller than those needed to perfectly correct for the variations of the scattering medium and thus, the optimization of relative phases re-directs a small portion of the light energy to form a high contrast focal point. We reached an enhancement of 32 corresponding to $\gamma \sim 0.3$, consistent with previously reported values (Yılmaz et al., 2013, Vellekoop and Mosk, 2008b).

Next, we directly demonstrated the prediction of Eq. (4.4). We de-magnified the SLM onto the scattering layer to an area of linear dimension $D = 500\ \mu m$, and executed the enhancement protocol at planes of different distances from the scattering layer. Figure 4.3(a) shows the intensity enhancement as the selected focal plane gets closer to the scattering layer (orange dots). The black line is a fit to the experimental data using Eq. (4.4) and keeping $\tan(\theta)$ as a free parameter. The intensity enhancement is not constant as Eq. (4.1) would predict but increases with the distance from the scattering layer, in agreement with the theoretical prediction of Eq. (4.4).
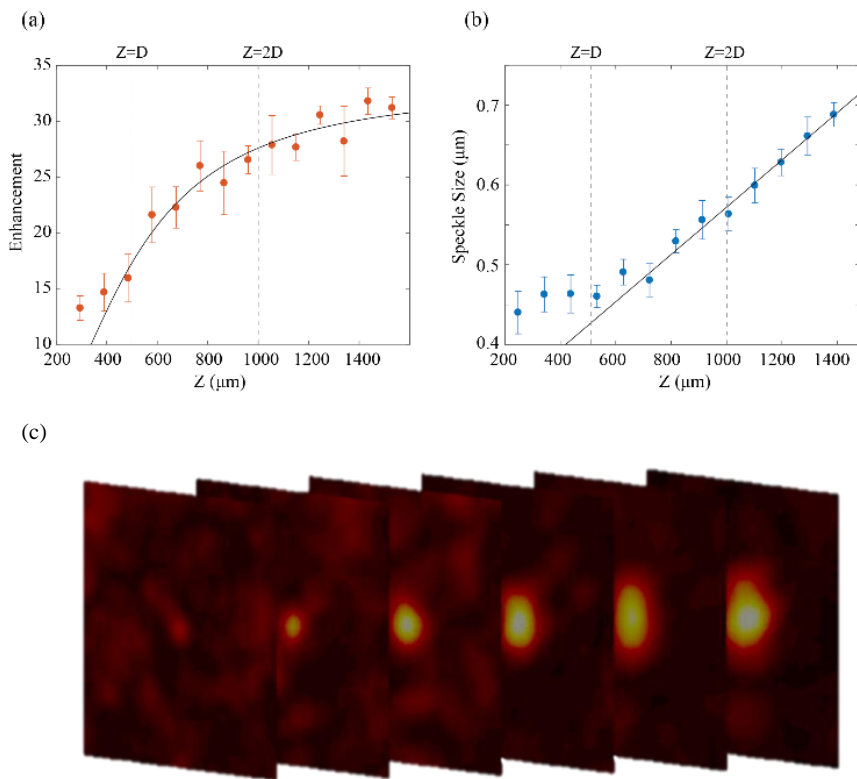
Figure 4.3: (a) Intensity enhancement at different focusing planes of varying distance from the scattering layer. Experimental data (orange dots) are well fit by Eq. (4) (black line). The optimization algorithm was performed >10 times for each data point and results below the median were discarded to eliminate artifacts due to mechanical vibrations or material decorrelation. (b) Speckle size at different focusing planes of varying distance from the scattering layer. Experimental data are calculated by first performing an autocorrelation of the speckle pattern then measuring the width at HWHM of the peak and dividing it by $\sqrt{2}$ to account for the autocorrelation broadening (Edrei et al., 2017b)(blue dots). A linear fit (black line) fits well the data after the critical distance.

(c) Experimental data of the focal point obtained at several distances (separated by $\approx 250\ \mu m$) from the scattering layer.

Figure 4.3(b) shows the corresponding average speckle size obtained at various distances from the scattering layer: as expected the speckle size is constant until a critical distance ($z_c \approx \frac{d \cdot D}{\lambda}$ (Goodman, 2007, Cerbino, 2007)) and then scales up linearly. Figure 4.3(c) shows the combined effects described in figures 4.3(a) and figure 4.3(b) – as the focal distance is increased the contrast is improved but the focal size is enlarged. Interestingly, this effect can also be explained using the effective area concept: before the "far-field" condition of Eq. 4.6, the effective area contributing to the constructive interference proportionally decreases and thus prevents further reduction of the speckle size (Goodman, 2007). Figures 4.3(a) and 4.3(b) are consistent with each other: using the value for θ obtained from the fit of Fig. 4.3(a), the critical axial location for linear speckle growth is $z_c \approx 1.65D$. Since in this experiment $D = 500\mu m$ this yields $z_c \approx 800\mu m$ which corresponds to the transition to linear speckle growth in Fig. 4.3(b).

To prove the universality of our findings, we repeated the experiments in Fig. 3 for three different sizes of illumination (D=250µm, 500µm, 1250µm) of the scattering layer. To compare the results, we considered that Eq. (4) reduces to $I_{enhancement} \approx 0.73\gamma N$ at the critical distance $z = z_c$ (under the approximation $tan(\theta) \approx \theta \approx \frac{\lambda}{d}$ [23]). Therefore, for each illumination size, we plot the value of z corresponding to 73% enhancement of the maximal value, which should correspond to the critical distance z_c. The results are presented in Fig. 4.4(a):
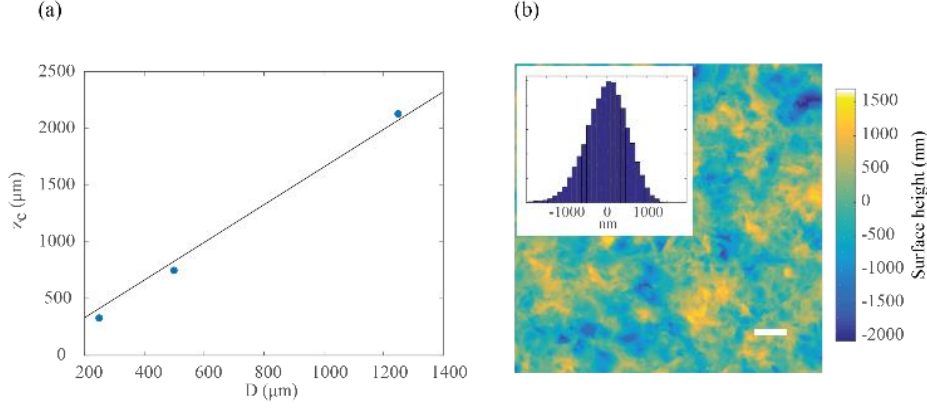
Figure 4.4: (a) Critical distance z_c, evaluated as the axial location corresponding to 73% of the maximal intensity enhancement, vs the illumination linear dimension D (blue dots). The black line is a linear fit to the data through the origin of the coordinates. (b) AFM surface height map of the scattering layer (scale bar $= 10\mu m$). The inset shows the distribution of surface heights.

The correlation between D and z_c is expected to be governed only by the divergence angle: $\theta \sim \frac{\lambda}{d}$ and is therefore constant for any illumination size. Indeed, the data from the three illumination sizes are well described by a linear fit. From the slope of the fit, we extracted the scattering divergence angle $\theta \sim \frac{\lambda}{d} = 0.6$, corresponding to $d = \frac{\lambda}{0.6} = 1100\ nm$. We confirmed the estimate of the scattering scale d by mapping the height of the diffuser with an Atomic Force Microscope (AFM) as shown in Fig. 4.4(b). From the AFM measurement the FWHM of the variation distribution is $\sim 1200\ nm,$ in good agreement with our calculated value. In biological tissues the scattering angle is typically smaller with forward scattering being the preferred direction (Jacques, 2013, Schott et al., 2015).

Our analysis leads to important practical consequences regarding focusing applications through scattering materials. Let's examine the experimental scenario where we want to distinguish two-point objects (at distance r) and we illuminate only one of them with the enhanced focal point. In this situation, the relevant specification to optimize is the contrast ratio between the two points, which depends both on the intensity enhancement and on the width of the focal point.

Assuming the focal point to have a Gaussian intensity profile of width $\sigma = \frac{z\lambda}{4D}$ given by the linear regime of Fig. 4.3(b), the contrast ratio can be evaluated combining Eq. (4.4) and the intrinsic contrast of the Gaussian intensity distribution:

$$C_r(z) = \gamma N \frac{\pi}{2D^2} (z \cdot tan\theta)^2 \left[erf \left(\frac{D}{\sqrt{2} \cdot z \cdot tan(\theta)} \right) \right]^2 \left(1 - e^{-\frac{r^2}{2\sigma^2}} \right) \qquad (4.7)$$

Fig. 4.5(a) illustrates the contrast ratio for two objects at distance r according to Eq. (4.7). The distance r between the two objects determines the needed resolution and, as a consequence, the distance z for maximal contrast ratio. For example, if a resolution of λ is desired, the maximal contrast ratio will be achieved at a plane $z \approx 2D$. Trying to enhance a focal point in a plane closer to the scattering layer will degrade the contrast due to lack of enhancement efficiency; trying to enhance the focal point in a plane farther from the scattering layer will degrade the contrast because the focal point widens. The set of maxima of Fig. 4.5(a) forms the Modulation Transfer Function (MTF) of the system, shown in Fig. 4.5(b) as a function of λ/r, a unitless measure of the spatial frequency of interest. As in traditional imaging systems, the modulation transfer function decays at high spatial frequencies; unlike traditional imaging systems, the best MTF values of this imaging system also depend on the observation plane z.
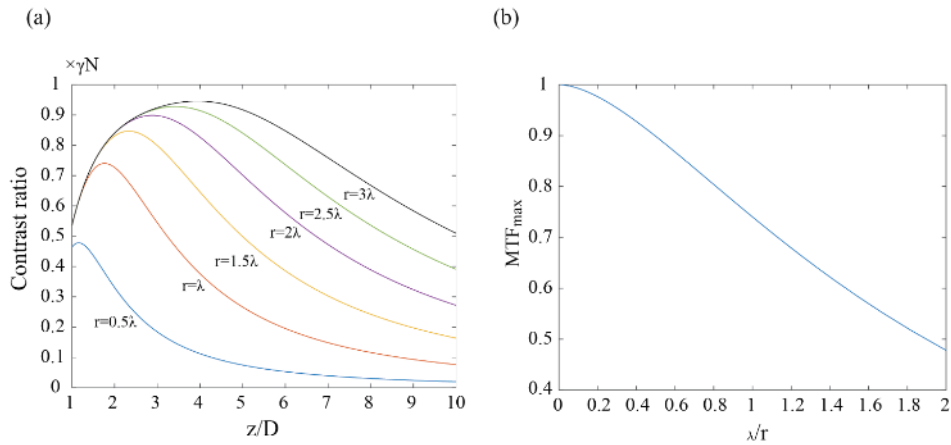

55

Figure 4.5: (a) Contrast ratio of the enhanced focal point as a function of distance from the scattering layer for different lateral resolutions ($\theta = 0.6$). The optimal contrast depends on the required resolution and is obtained at a specific distance from the scattering layer. (b) The MTF of the system evaluated by collecting the maxima of (a).

4.4 Discussion

In summary, in this work we derived and verified the intrinsic limits of intensity enhancement that can be reached when focusing light through a scattering material at different axial locations. This has direct relevance for the many studies that use scattering materials as a platform for high resolution microscopy/focusing (Vellekoop et al., 2010, Van Putten et al., 2011, Jang et al., 2018, Leonetti et al., 2018). Our analysis can determine the maximum contrast achievable when high-resolution or super-resolution is attempted with scattering lenses. Optimal enhancement is achieved by imaging as many SLM pixels as possible into the effective illumination area calculated here; thus, in practice, the ultimate enhancement limit is reached when the SLM pixels are de-magnified to the smallest size allowed by the imaging system that projects the SLM map onto the scattering material. In the evanescent-wave regime ($z \sim 100\ nm$) sub-wavelength resolutions can be reached (Parigi et al., 2016); but, the effect of the divergence angle will need to be considered. The effective illumination area in the evanescent regime is expected to be reduced to several microns, which will limit the intensity enhancement; this could explain why experimentally the enhancement was found to be far from optimal in this regime (Park et al., 2013). For practical applications, it will be important to establish how much intensity enhancement is required to achieve sufficient contrast for specific purposes, such as fluorescence excitation, neural activity modulations or label-free imaging. This will ultimately determine how close the focusing plane can be set and how high resolution can be achieved. The phenomenon we describe here may also be applicable to the emerging field of focusing and imaging through multimode fibers (Ploschner

et al., 2015, Papadopoulos et al., 2012, Papadopoulos et al., 2013, Tzang et al., 2018) as the enhancement capabilities at close proximity to the fiber outlet is expected to decrease.

In conclusion, we theoretically derived and experimentally verified the intrinsic limits of intensity enhancement when focusing light through a scattering material. We found that the enhancement is severely limited as the distance between the scattering layer and the focal plane is decreased while it approaches the optimal value of γN in the far field where the focal point, hence the resolution of the optical system, is not optimal. In this work we obtained the coherent focal point using an iterative process; however, our derivation is general and valid for other methods of coherent focusing using phase modifications such as optical phase conjugation (Yaqoob et al., 2008), transmission matrix inversion (Popoff et al., 2010b) or time reversal (Derode et al., 1995).

PART II

Brillouin spectroscopy within scattering and aberrating materials

Chapter 5

Spectral coronagraphy for high extinction Brillouin imaging[*]

In this chapter, we discuss the extinction problem introduced by elastic scattering in the context of VIPA (virtually imaged phased array) based Brillouin spectroscopy and present a novel method to reduce such effect. The extinction is defined as the ratio between the intensity of a spectral peak to the background arising from the peak residual and observed at other spectral components. Current designs of multi-stage VIPA spectrometers offer enough spectral extinction to probe transparent tissue, cells and biomaterials. However, in highly scattering media or in the presence of strong back-reflections, such as at interfaces between materials of different refractive indices, VIPA-based Brillouin spectral measurements are limited. While several approaches to address this issue have recently been pursued, important challenges remain. Here we have adapted the design of coronagraphs used for exosolar planet imaging to the spectral domain and integrated it in a double-stage VIPA spectrometer. We demonstrate that this yields an increase in extinction up to 20 dB, with nearly no added insertion loss. The power of this improvement is vividly demonstrated by Brillouin imaging close to reflecting interfaces without index matching or sample tilting.

5.1 Background

For many years, Brillouin light scattering spectroscopy has been used in applied physics and material science to characterize material properties without contact and noninvasively (Hartschuh et al., 2005, Dil, 1982, Serga et al., 2006, Still et al., 2008, Minami and Sakai, 2009). Spontaneous Brillouin scattering arises from the interaction of incident light with acoustic phonons, thus, the scattered light presents very small frequency shifts on the order of 1–10 GHz (<0.02 nm). As a result, Brillouin spectroscopy is challenging from an experimental standpoint: high spectral resolution as well as high spectral extinction are needed to detect weak Brillouin signals close to non-shifted optical signals, which can be more than 10^9 times stronger (Boyd, 2008). Traditionally, this challenge has been met with multi-pass Fabry-Perot interferometers (Sandercock, 1970, Meng et al., 2016, Palombo et al., 2014); however, this technique requires long acquisition times of about minutes per spectrum (Palombo et al., 2014). In recent years, the development of VIPA-based spectrometers (Scarcelli and Yun, 2008) dramatically reduced the required acquisition time by parallel spectral detection. This approach enables collecting the entire Brillouin spectrum in one shot and with high throughput efficiency, thus bringing the acquisition times down to ~100 ms, even for low power incident light levels compatible with biological materials (Scarcelli et al., 2008, Scarcelli and Yun, 2012, Scarcelli et al., 2015b, Fiore et al., 2016, Scarcelli et al., 2012).

The spectral extinction of the various designs of VIPA-based spectrometers has proven sufficient to observe Brillouin signatures of transparent tissues, polymers and biological cells (Elsayad et al., 2016, Antonacci and Braakman, 2016, Scarcelli et al., 2015b, Antonacci et al., 2015b, Steelman et al., 2015, Zhang et al., 2016). Instead, VIPA-based Brillouin measurements have remained limited in situations where a large amount of non-shifted laser light enters the spectrometer. This occurs when scattering media such as biological tissues are sampled and

especially when voxels close to an interface of two materials with a different refractive index are interrogated. This experimental situation is particularly important for in vivo Brillouin measurements, where index mismatches cause large back-reflections (Besner et al., 2016, Girard et al., 2015, Scarcelli et al., 2015a). For example, according to Fresnel equations (Goodman, 2005), an interface between two materials with small refractive index difference, e.g. 1.4 vs 1.5, will reflect ~0.12 % of the laser light directly into the spectrometer, i.e. a non-shifted component of more than 6 orders of magnitude higher than the Brillouin signal. Without sufficient spectral extinction, such large non-shifted component bleeds through the rest of the spectral pattern, thus resulting in a strong background at Brillouin-shifted frequencies.

In recent years, a great amount of research has been conducted to increase the spectral extinction of VIPA-based spectrometers. One solution is to increase the spectral selection of the spectrometer: a third VIPA spectrometer stage (Scarcelli and Yun, 2011) or a narrowband filter within the optical train such as a Fabry-Perot etalon (Fiore et al., 2016, Shao et al., 2016) were inserted in the spectrometer and provided improved extinction of 20 dB or more, but with significant insertion losses; the spectral selection of the spectrometer was also increased by inserting an absorbing gas chamber (Meng et al., 2014) which can give both high extinction and low losses but requires tunable lasers and frequency locking to maintain stable rejections. Another approach is to eliminate the non-shifted light component by destructive interference (Antonacci et al., 2015a); this can reach up to 35 dB added extinction with moderate loss but generally only works for a specific reflection plane and stably maintaining the efficiency of the spectrometer over time can be challenging. Beam shaping of the VIPA output has yielded moderate increase in extinction of up to 10 dB for only 10 % insertion loss (Scarcelli et al., 2015b), but the insertion losses become significant if higher extinctions are required (Antonacci et al., 2016). Finally, also

stimulated Brillouin scattering has been shown to improve the discrimination between elastic

scattering and Brillouin-shifted components (Remer and Bilenca, 2016a).

In this chapter, we take a different approach to the issue and demonstrate a relatively simple

addition to a VIPA spectrometer that can increase extinction by up to 20 dB without reducing the

intensity of the Brillouin signal. We found that the remaining obstacle to achieve the ultimate

extinction of VIPA spectrometers comes from the diffraction noise of the optical elements within

the spectrometer; as a result, we introduced a spectral coronagraphy filter designed to eliminate

this noise component. Importantly, our method is compatible with other noise reduction techniques

and so it could be combined with them in the future to maximize performance.

5.2 Principle

To explain the principle behind our method, we use a double-stage VIPA spectrometer as an

example. In each stage of the spectrometer, the VIPA etalon produces a spectrally dispersed pattern

in the focal plane of the lens placed just after the etalon [Fig. 5.1(a), planes A and B], i.e. the

spectrally dispersed pattern is the Fourier transform of the electromagnetic field at the output of

the VIPA. In a double-stage spectrometer, the two spectral dispersion stages are cascaded

orthogonally to each other and the planes of the respective spectrally dispersed patterns are

conjugated [Fig. 5.1(a), planes A and B]. Finally, the image of the spectrally dispersed pattern is

projected onto a CCD camera and a pattern like in Fig. 5.1(a) (plane C) is formed where the

Brillouin signals are surrounded by periodic patterns of non-shifted light components.

In scattering media or close to interfaces, the non-shifted light components include

elastically scattered light and laser reflections, which are dominant so that the Brillouin-shifted

component is difficult to detect. This situation is conceptually similar to what astronomers face

when they want to image exosolar planets located near stars, i.e. faint objects located in close proximity of a bright light source. In astronomy, the contrast ratio between the faint object of interest and the bright star is often as high as 10^9. This has spurred the extensive development of so-called coronagraphs (Baudoz et al., 1997, Mawet et al., 2005, Roddier and Roddier, 1997, Rouan et al., 2000, Lyot). A popular coronagraphy technique was first implemented by Bernard Lyot (Lyot). In the Lyot coronagraphy technique, the exosolar scene is imaged onto an occulting mask, which is designed to block the light generated by the bright star. However, the diffraction of the light from the bright star due to the finite sized optical elements of the imaging system is often still several orders of magnitude brighter than the faint object of interest. To address this issue, another 4-f imaging system is employed to image the occulting mask plane onto the camera, and a spatial filter is placed in the Fourier plane of the imaging configuration to block high order spatial frequencies generated by the diffraction.

To adapt the coronagraphy solution to Brillouin spectroscopy, we recognized VIPA spectrometers present the opposite experimental situation of exosolar planet imaging: instead of having a bright star in the center of the field of view, several bright peaks are in the corner of the field of view and the faint objects (the Brillouin peaks) sit in the center. The first part of the coronagraphy solution is already implemented in most VIPA spectrometers; two spatial filters, shaped as rectangular masks, are generally employed in the planes of the spectrally dispersed patterns to let Brillouin-shifted signal through while physically blocking all non-shifted light components. These masks effectively block the geometrical path of non-shifted light components; however, they cannot stop high-order spatial frequency components arising from light diffraction within the beam path. This results in strong background noise for the Brillouin signal of interest. To better describe the extent of this issue, we consider the exemplary configuration where a lens

(f=200 mm) is used after the VIPAs to obtain the far-field spectral pattern. The measured spectrum is the convolution of the ideal spectral pattern with an Airy-function given by the diffraction limit of the lens [as illustrated in Fig. 5.1(b)]. High frequency side lobes typical of the Airy function will thus appear at the boundaries of the blocking masks as illustrated in Fig. 5.1(c) [Note that Figs. 5.1(b) and 5.1(c) employ different intensity scales to better visualize the features in each figure]. Diffraction of the non-shifted component of the light therefore leads to a significant background (-35 dB) in the center of the spectrally dispersed pattern, regardless of the spectral performances of the VIPA interferometer. Under high back-reflection conditions, this high frequency diffraction pattern can easily overcome the Brillouin signal, as illustrated in Fig. 5.1(c).
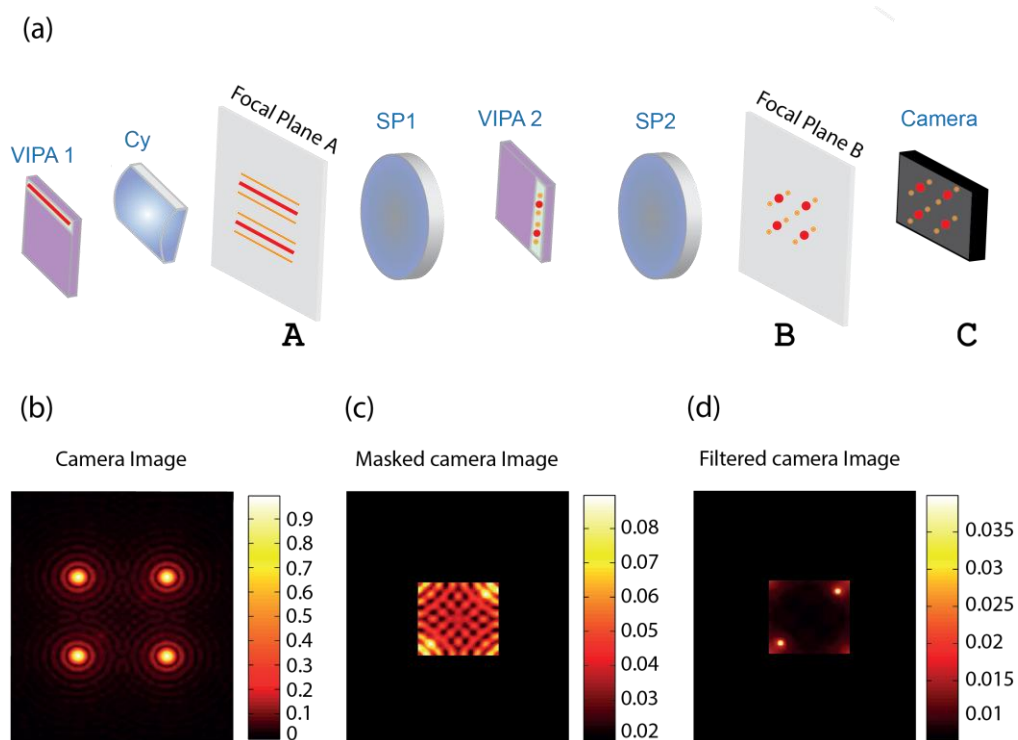

Figure. 5.1. Illustration of diffraction noise in the double stage VIPA spectrometer: (a) Schematics of the spectrometer. The first VIPA pattern is observed at the focal plane of a cylindrical lens (plane A) and imaged via a 4-f imaging system and through a second VIPA onto a second plane (plane

B). Finally, the pattern is recorded by a camera (planes A, B and C are conjugated). (b) An illustration of the Airy patterns and the Brillouin signals as recorded by the camera, under a high back-reflection condition. Two vague Brillouin peaks located within the Airy patterns can be barely distinguished from the background noise. (c) By physically blocking the periphery of the field of view the majority of the light intensity is blocked, yet, the diffraction pattern is still present. (d) In the absence of the diffraction patterns very faint signals can be visualized.

To eliminate the diffraction noise within the spectrometer, similarly to Lyot coronagraphy, another 4-f imaging system can be built to image the plane of the blocking masks onto the camera. A spatial filter is then introduced in the Fourier plane of this imaging system to block the high spatial frequencies generated by diffraction of the strong laser reflections. As illustrated in Fig. 5.1(d), this is expected to yield a much cleaner spectrum, in which faint signals placed near bright spectral components can be measured.

5.3 Characterization of spectral coronagraphy

To characterize the performance of the coronagraphy filter, we built a Brillouin microscope with a double-stage apodized VIPA spectrometer. The experimental setup is shown in Fig. 5.2(a). We expanded a single frequency laser beam of wavelength 660 nm (LaserQuantum) and, after a beam-splitter, focused it onto the sample of interest. In epi-detection configuration, we collected the light scattered from the sample and coupled it into a single mode fiber to enter the spectrometer. The spectrometer was composed of two orthogonally oriented VIPA stages with etalons of 5mm thickness and 15 GHz Free Spectral Range (LightMachinery). We collimated the light from the fiber and using a cylindrical lens (Cy1, f=200 mm) we focused the beam into the VIPA1 etalon tilted in the vertical direction. We used a second cylindrical lens (Cy2, f=200 mm) to then focus the output of the VIPA1 etalon and obtain a spectrally dispersed pattern in the focal plane of Cy2. In this plane, we placed a vertical slit (slit 1) to block the non-shifted laser pattern. Next, we

repeated the process using another spectral dispersion stage in the horizontal direction: we focused the pattern transmitted through slit 1 by a spherical lens (SP1, f=200mm) onto the VIPA2 etalon and used a second spherical lens (SP2, f=200 mm) to focus the output of VIPA2. We obtained a spectrally dispersed pattern in the focal plane of SP2. In this plane, we placed a horizontal slit (slit 2) to block the non-shifted laser pattern. As previously mentioned, the second stage of the spectrometer behaves as an imaging system for the vertically dispersed pattern and the VIPA2 etalon is in the infinity space of the imaging system SP1- SP2. For apodization, after each VIPA etalon we placed a gradient neutral density filter that shaped the VIPA output pattern. To implement the spectral coronagraphy within the VIPA spectrometer, in the final segment of the VIPA spectrometer, we added a 4-f system with two identical lenses SP3 and SP4 (f=30 mm) and we placed an iris of variable aperture (denoted as "Lyot stop" in Fig. 5.2) in the Fourier plane which serves as a low-pass spatial filter.

Figures 5.2(b)-5.2(d) illustrate the ability of our method to reduce the diffraction-background noise component. At the interface of a cuvette (n~1.58) and water (n~1.33) the Brillouin signal could not be seen because of large background noise [Fig. 5.2(b)], however, by closing the Lyot stop, we were able to clearly observe the Brillouin signal [Fig. 5.2(c)]. A line average over the width of the signal reveals ~20 dB noise reduction compared with the spectrometer with the opened Lyot stop [Fig. 5.2(d)]. To further demonstrate the importance of our method for measuring a scattering sample, we filled the cuvette with a solution of water and 10% milk and acquired the signal 130 µm inside the scattering medium. Figures 5.2(e) and 5.2(f) show the recorded spectrum when the Lyot stop was opened and closed respectively. A line average over the width of the signal is presented in Figure 5.2(g).
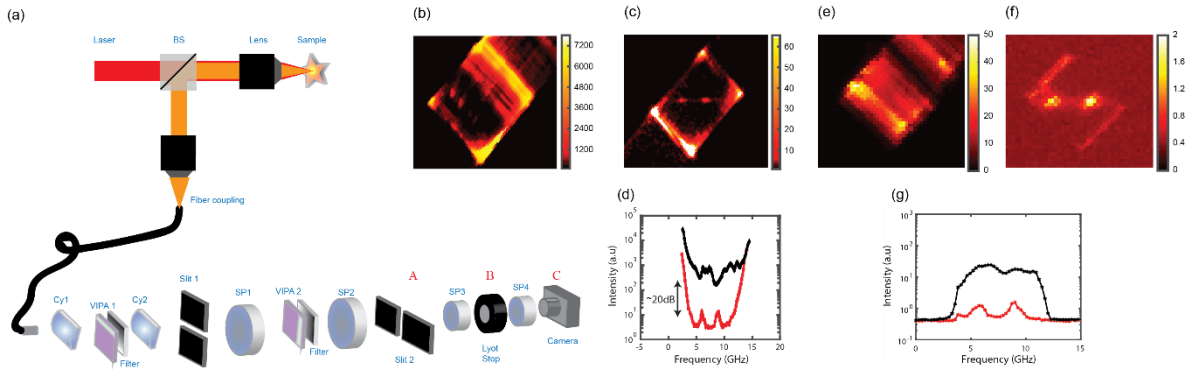
Figure 5.2. Setup and quantification of the coronagraphy effect: (a) An expanded laser beam (red path) is focused into a sample by a 0.7 NA lens (Olympus, LUCPLFLN 60X). Back scattered light (orange path) is collected in an epi-detection configuration and coupled into a single mode fiber. The collimated beam exiting the fiber is focused by a cylindrical lens (Cy1) into the first VIPA; the pattern is gradually filtered and focused onto a vertical slit (slit 1) placed in the focal plane of a second cylindrical lens (Cy2). Next, the pattern is imaged by a 4-f imaging system and through a second VIPA onto a horizontal slit (slit 2). The final plane of the spectrometer (plane A) is imaged onto the camera (plane C) via another 4-f imaging system with a spatial filter (Lyot stop) located in the Fourier plane (plane B). (b, c) Brillouin signal from the interface between water and a plastic cuvette, recorded with 27 mW laser power at the sample and 100 ms integration time. The back reflection from the interface was measured to be ~0.7%. (b) With the Lyot stop open the background overcomes the Brillouin signal. (c) By closing the Lyot stop, a clean Brillouin signal can be observed. (d) Average line plot of the signal width in b and c, demonstrating a ~20 dB noise reduction obtained by the Lyot stop. (e) A Brillouin measurement with an opened Lyot stop 130 µm inside a scattering liquid (10% milk 90% water). (f) A Brillouin measurement with a closed Lyot stop 130 µm inside a scattering liquid (10% milk 90% water). (g) Average line plot of the signal width in e and f, demonstrating a ~15 dB noise reduction obtained by the Lyot stop.

The efficiency of noise reduction depends on the diameter size of the Lyot stop relative to the size of the diffracting aperture (Sivaramakrishnan et al., 2001). To quantify this behavior within our setup, we varied the Lyot stop size and recorded the diffraction-background noise by measuring the light intensity level in the central region of the spectrum between the two Brillouin peaks. Figure 5.3a shows the experimental results of the Lyot stop diameter reduction (red symbols). For large Lyot stops nearly no reduction of background noise is observed. As the diameter of the Lyot

stop decreases, there is a sharp drop of the noise level, followed by a slow monotonic decline. This behavior is expected and can be understood as follows: once the peak of the Airy function is physically blocked by the masks, the remaining portion of the Airy function is a series of diffraction "rings", i.e. intensity peaks and valleys that repeat with a nearly constant period. In the Fourier plane where the Lyot stop is inserted, the diffraction noise therefore has dominant spatial frequencies at a given radius from the center, corresponding to the period of the Airy diffraction rings. As long as the diameter of the Lyot stop lets these dominant spatial frequencies through, the reduction in noise is very small. However, when the diameter of the Lyot stop becomes small enough to block these frequencies, a large drop in diffraction background noise is observed. Once, the dominant noise component has been eliminated, only a moderate further decrease in noise is achieved when closing the Lyot stop further and this corresponds to lower spatial frequency components composing the Airy pattern.

A unique feature of this noise reduction technique is that the measured Brillouin signal is nearly not affected by the blocking aperture placed in the Fourier plane. Figure 5.3(b) shows the intensity of the Brillouin signal for different diameter of the Lyot stop. Within our setup the Lyot stop does not decrease the intensity of the Brillouin signal until the stop is almost totally closed. This provides almost a 20 dB rejection of background noise with nearly no loss.
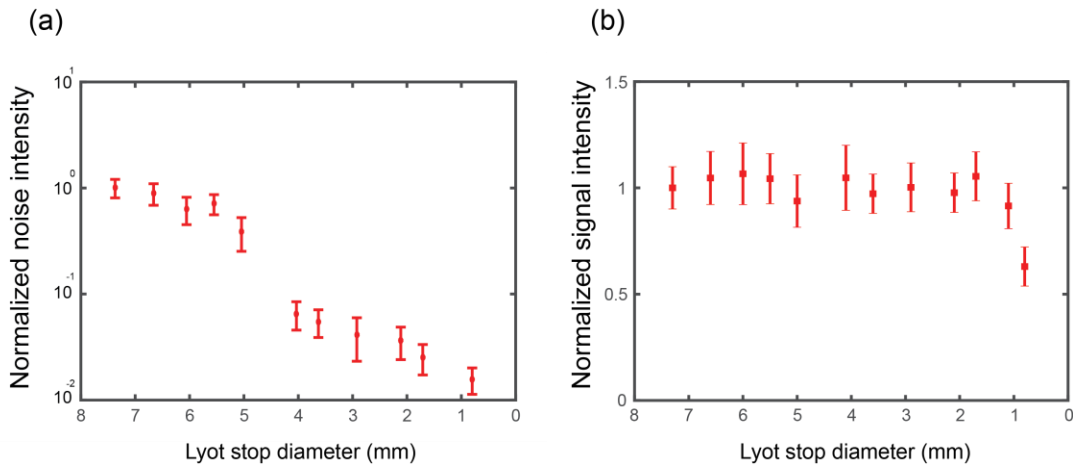
Figure 5.3. (a) Noise levels as a function of Lyot aperture diameter, closing the aperture reduces the noise levels (red symbols). The noise was determined by averaging the value of 30 pixels at the center of the image; the error bars represent the standard deviation over the same region. (b) Brillouin signal intensity as a function of the Lyot stop diameter. For Lyot stop diameters larger than 1 mm the signal intensity is not affected. Error bars represent the standard deviation of 25 repeated measurements of the Brillouin peak intensity (average of Stokes and anti-Stokes signals). All measurements were performed on a water sample as in Fig. 5.2.

5.4 Application of coronagraphy to Brillouin imaging

To demonstrate the improvement of our technique in practice, we applied it to Brillouin measurements on a PDMS micro-fluidic channel (width 250 μm, height 360 μm). We performed Brillouin imaging of the XZ cross-section plane [Fig. 5.4(a)] with transverse resolution of 0.5 μm and axial resolution of 2 μm. The laser intensity at the sample was 25 mW and the integration time was set to 0.1 sec. We left the channel empty to maximize back-reflection noise due to the refractive index mismatch. The refractive index mismatch between PDMS and air is significant (~0.4); hence, a strong back reflection of 2.8 % is expected from each interface plane. The reflected laser light is directed into the spectrometer generating a high level of background noise in the spectrally dispersed plane recorded by the camera. We used the average intensity value in the position between the Stokes and anti-Stokes Brillouin signals as a measure of the background noise in our system. When the Lyot stop is open, the background collected when recording from a position close to the interfaces between the PDMS and air is more than 200 times higher than the background noise seen in other parts of the sample [Fig. 5.4(b)]. By closing the Lyot stop, the noise level close at these interfaces was dramatically reduced, by ~2 orders of magnitude [Fig. 5.4(c)].

The Brillouin images of the sample, i.e. maps of the local Brillouin shift, are presented in Figures 5.4(d) and 5.4(e), showing the measurement acquired with an opened and a closed Lyot stop, respectively. For comparison, both images were processed in the same manner. Pixels located between the two interfaces [identified as the maximal values of every column in Figure 5.4(b)] are shown in black. When the Lyot stop was open, it was impossible to perform reliable Brillouin imaging of the PDMS material surrounding the air channel, even up to 50 microns away from the air-PDMS interfaces, as shown by the large deviation of Brillouin shift from the expected PDMS values [Fig. 5.4(d)]. By closing the Lyot stop, we were able to minimize these artifacts, and clear measurements were possible close to the interface between PDMS and air [Fig. 5.4(e)]. Fig. 5.4(f). shows line plots across the dashed lines in Figs. 5.4(d) and 5.4(e); it can be seen that the measurement with an open Lyot stop suffers dramatic false variations from both sides of the air region (red curve), while a closed Lyot stop removes the majority of these discrepancies (blue curve). Even relatively far from the interfaces the Lyot stop is helpful as it reduces the amplitude of the fluctuations in the Brillouin shift measurement due to residual background noise.
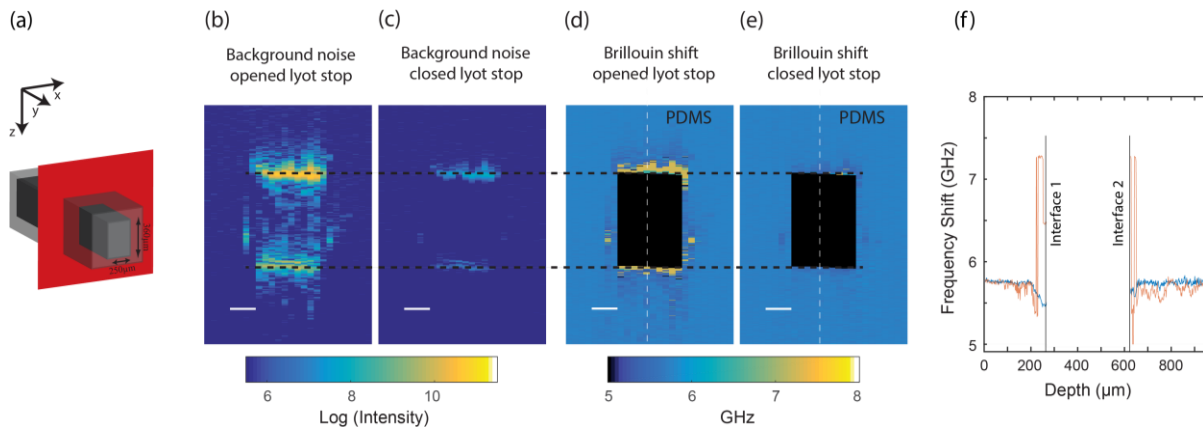

Figure. 5.4. Brillouin imaging of a micro-fluidic channel: (a) Illustration of the PDMS micro fluidic channel (width=250 µm, height=360 µm). Scanning was performed across the XZ plane highlighted in red. Background noise levels defined as the average intensity value between the

Brillouin peaks with (b) the Lyot stop widely open and (c) with a closed Lyot stop (scale bar = 100 µm). The noise from the interfaces was nearly removed for the latter. False color bar indicates camera counts on log scale. Brillouin shifts recorded with (d) an open Lyot stop and (e) a closed Lyot stop. For the former there are clear artifacts up to 50 microns away from the interfaces, whereas the latter show a continuous Brillouin shift up to the interface between air and PDMS. (f) Line plots of the Brillouin shift measurements across the central part of microfluidic channel denoted by a dashed line in Figs. 4(d) and 4(e), for an opened Lyot stop (red) and a closed Lyot stop (blue).

5.5 Conclusions

In this work, we have introduced the concept of spectral coronagraphy and implemented it within a double stage VIPA spectrometer. The idea addresses a fundamental noise component, which exists in every imaging system, including spectrometers, i.e. the diffraction patterns generated by the finite-sized optical elements. In many scenarios, the diffraction noise element is negligible due to its low intensity, or -- for spectrometers -- it can often be removed by placing a narrow-band filter to block the excitation wavelength. This is the case for example in fluorescence measurements and Raman spectroscopy where the emitted signal and the excitation light are spectrally well separated for a standard notch filter to suppress non-shifted light components. However, as demonstrated here, the diffraction noise component can be significant for Brillouin scattering measurements and the frequency shifts involved are too small to be blocked with a conventional notch filter. Intense non-shifted laser light arising from elastic scattering or back-reflections can often occur in the same plane and in close proximity to the low-intensity Brillouin signal of interest and are thus immune to confocal rejection or traditional spectral filtering. In this case, a diffraction noise of greater intensity than the measured signal is observed by the spectrometer. We identified this situation to be of great resemblance to what astronomers face when a faint star located close to a bright sun is imaged directly. Hence, we have implemented a

similar coronagraphy method within our spectrometer to reduce diffraction noise patterns and found it to be especially beneficial when the spectrum is acquired close to interfaces between two materials of different refractive index. We quantified the noise reduction in Brillouin imaging settings and found that a rejection of up to ~20 dB is achieved with no insertion loss. This will provide important practical advantages for Brillouin imaging as it will reduce the need of other sub-optimal strategies employed to manage the amount of non-shifted light entering the spectrometer such as index matching or sample tilting. Due to the straightforward implementation of our method, we expect that this technique will find widespread application in VIPA-based spectrometers.

Chapter 6

Improving localization precision of Brillouin measurements using spectral autocorrelation analysis[*]

The sensitivity to mechanical changes that a Brillouin spectrometer can detect is determined by the precision to which a spectral peak can be localized. The localization precision is however fundamentally limited by the low number of photons within a Brillouin measurement, as well as by intrinsic noise of the setup. In this chapter we present a method to improve the spectral sensitivity of Brillouin measurements by exploiting the autocorrelation function of the spectrum. We show that by performing a localization process on the autocorrelation function nearly 20% increase in localization precision can be obtained. This result is consistent between our theoretical treatment, numerical simulation and experimental results. We further study the effect of background noise on the precision improvement for realistic scenarios.

6.1 Background

Brillouin spectral analysis for applications that require high sensitivity to small mechanical changes is based on the localization of the spectral peak maximum. In fact, to capture biologically-relevant changes in material stiffness sensitivities of $\sim 10 MHz$ are needed (Scarcelli et al., 2015a); but both instrumentally, typical spectrometers have spectral resolutions in the order of hundreds of MHz to GHz; and fundamentally, biological materials present natural linewidths that exceed 500 MHz. Because of the localization processing, not only the spectral resolution of the spectrometer but also the signal-to-noise ratio and signal-to-background ratio are important factors that impact the spectral sensitivity of the measurement, which determines the mechanical sensitivity of the instrument. However, the intensity of the Brillouin spectral components is fundamentally limited due to the small scattering cross-section of the photon-phonon interaction. Over the past years, different approaches to this challenge have been pursued: on one hand stimulated scattering interaction (Ballmann et al., 2015, Remer and Bilenca, 2016b) or multiplexed configurations (Zhang et al., 2016) have been demonstrated; on the other hand, an ongoing effort is devoted to improving the efficiency of signal detection (Berghaus et al., 2015b), spectral contrast of the spectrometer (Edrei et al., 2017a, Fiore et al., 2016, Shao et al., 2016) and removing background components (Berghaus et al., 2015a, Remer and Bilenca, 2016a, Antonacci et al., 2015a, Meng et al., 2014). Here, we present an analysis method of the Brillouin spectrum based on the spectral autocorrelation function of the acquired signal. We will show both analytically and experimentally that working in the autocorrelation space is advantageous compared to current protocols in terms of localization precision.

6.2 Principle

Brillouin spectra are usually shown as a triplet of peaks: the central non-shifted peak arises from elastic scattering, while two shifted peaks, named Stokes and anti-Stokes, come from the inelastic phonon-photon scattering interactions. To determine the local elasticity from the acquired spectrum the shift of the Stokes or anti-Stokes peaks from the non-shifted central peak is required. However, the central peak is often many orders of magnitude brighter than the Brillouin signals as it contains Rayleigh, Mie interactions as well as all back-reflections of laser within the setup; therefore, the dynamic range of the camera can't capture both laser and Brillouin peaks in the same frame. One way to address this problem is to physically block the central peak in order to measure the weaker Brillouin peak. Under these circumstances though, it is impossible to determine the shift of the Brillouin signal, as no reference from the laser is recorded. A potential solution to this issue is to record the location of the laser peak beforehand and use it as a reference to evaluate the Brillouin shift in future measurements. However, laser frequency drifts or spectrometer jitters during measurements are difficult to avoid so that the laser peak location cannot be assumed to be constant. To resolve this issue, one can take advantage of the fact that Brillouin spectrometers show several diffraction orders, therefore, the Stokes and anti-Stokes peaks from two different diffraction orders can be captured in a single acquisition: the distance between the two peaks represents a robust signature to determine the Brillouin shift.

The straightforward procedure to obtain the Brillouin shift in these conditions is a as follows: the spectrum containing the Brillouin Stokes and anti-Stokes peaks from two consecutive diffraction orders is recorded, and the distance between the peaks is determined by localizing each peak using a fitting algorithm. Next, the peak separation is subtracted from the known free spectral range of the spectrometer, and this value corresponds to twice the magnitude of the Brillouin shift

in pixels. To transform the result into frequency units, a calibration process is carried-out using materials of known Brillouin shifts (Berghaus et al., 2015b, Scarcelli et al., 2015b). Although the Brillouin peaks natural bandwidth is typically hundreds of MHz, the precision to which the center of the peaks can be determined is much greater. Similar to localization microscopy and particle tracking, the localization accuracy of the center of a spot is determined by optical properties such as the number of photons within the spot and the background noise present in the measurement (Thompson et al., 2002). In contrast to localization microscopy protocols, however, in which the absolute location of each emitter is desired, the key parameter in Brillouin analysis is the relative distance between the Stokes and anti-Stokes peaks from which the Brillouin shift can be extracted. Although the peak separation can be obtained by performing two separate localization processes as described above, each localization process will contribute to the error of the estimation of the peaks separation which will therefore be enhanced. Here we demonstrate a different approach which relies on the autocorrelation function of the acquired spectrum. The autocorrelation of an object preserves information about the relative distances within the object, while the actual object form is lost and can be retrieved only under specific circumstances (FIENUP, 1977, Katz et al., 2014a, Edrei and Scarcelli, 2016b, Bertolotti et al., 2012). Particularly, for a two-peak spectrum the autocorrelation will contain three peaks, and the distance between the original two peaks will transform into the distance between the center of the autocorrelation function and either side peak (fig 6.1. a-b). Hence, tracking the distance between the two spectral peaks is equivalent to tracking the distance of the side peak from the center in the autocorrelation space. This results in improved precision in the localization protocol, thus offering a more efficient use of the information content of the collected photons.

6.3 Theoretical derivation

In general terms, the spatial uncertainty on the detection of a single photon hitting a camera is determined by the standard deviation of the point spread function of the imaging system σ. Yet, a set of N independent measured photons can be treated as N measurements of the signal location, hence, the precision to which the average position can be determined is given by the standard error of the mean: $\frac{\sigma}{\sqrt{N}}$. When two signals are detected and the distance between the signals is of interest, it can be measured using two separate localization processes or, as proposed here, by a single localization process in the autocorrelation space. Although the Brillouin signal presents a natural Lorentzian spectral distribution, the signal is convolved with the Airy pattern generated by the imaging systems of the spectrometer, as well as with a Gaussian envelope attributed to the apodization of the VIPA output. Therefore, a treatment of a more complex Voight profile will be the most proper one, yet, for simplicity here we evaluate the localization precision for both the double fitting and the autocorrelation analysis and compare them for one dimensional Gaussian shaped signals.

We begin by calculating the precision to which the distance between two signals can be determined. We consider a function of two independent Gaussian shaped signals separated by a distance 'd' as presented in figure 6.1a:
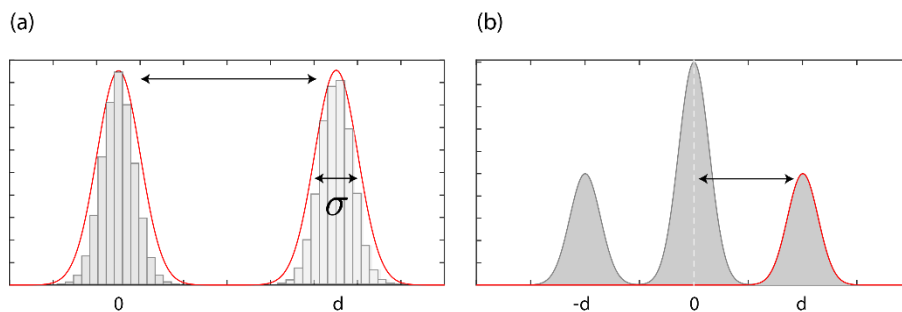
Figure 6.1: (a) Original signal: the distance between two peaks 'd' can be obtained by fitting the data and measuring the separation. (b) The autocorrelation function: the displacement of either side peaks from the center equals the distance between the original peaks.

$$f(x) = \frac{N_o}{\sigma\sqrt{2\pi}}\left(e^{\frac{-(x-d)^2}{2\sigma^2}} + e^{\frac{-x^2}{2\sigma^2}}\right) \qquad (6.1)$$

Where N_o is the number of photons contained in each peak. Hence, the localization precision of each peak is given by the standard error of the mean for the calculated number of photons: $\frac{\sigma}{\sqrt{N_o}}$.

The peak separation error is influenced by both peak localizations and is therefore larger:

$$\sqrt{\langle(\Delta d)^2\rangle}_{Double\ fit} = \frac{\sqrt{2}\sigma}{\sqrt{N_o}} \qquad (6.2)$$

Next, we derive the localization accuracy for the autocorrelated function. The autocorrelation can be calculated by multiplying equation (6.1) by a shifted form of itself and integrating over the spatial coordinate:

$$C(q) = \int_{-\infty}^{\infty} \frac{N_o}{\sigma\sqrt{2\pi}}\left(e^{\frac{-(x-d)^2}{2\sigma^2}} + e^{\frac{-x^2}{2\sigma^2}}\right) \cdot \frac{N_o}{\sigma\sqrt{2\pi}}\left(e^{\frac{-(x-d-q)^2}{2\sigma^2}} + e^{\frac{-(x-q)^2}{2\sigma^2}}\right) dx \qquad (6.3)$$

where q is the spatial coordinate in the autocorrelation space and represents the displacement of the two functions. The autocorrelation, normalized to the single peak intensity, can be therefore written as:

$$C(q) = \frac{N_o}{\sigma\sqrt{2\pi}}\left(e^{\frac{-(d+q)^2}{4\sigma^2}} + 2e^{\frac{-q^2}{4\sigma^2}} + e^{\frac{-(d-q)^2}{4\sigma^2}}\right) \qquad (6.4)$$

The autocorrelation function has three peaks, each side peak is located a distance 'd' from the center of the function corresponding to the original separation of the peaks (fig 6.1b). To evaluate the localization precision for the correlated peak we calculate the effective number of photons in the side peak of the autocorrelation by integrating over one of the side peaks:

$$\int \frac{N_o}{\sigma\sqrt{2\pi}} e^{\frac{-(d-q)^2}{4\sigma^2}} dq = \sqrt{2}N_0 \qquad (6.5)$$

The localization precision is determined by the standard error of the mean in the new space; it thus depends on the number of photons calculated in (6.5) and the width of the autocorrelation peak, which is $\sqrt{2}\sigma$. As a result the localization precision is therefore:

$$\sqrt{\langle(\Delta d)^2\rangle}_{Autocorrelation} = \frac{\sqrt{2}\sigma}{\sqrt{\sqrt{2}N_0}} \qquad (6.6)$$

The net improvement in precision provided by the autocorrelation process is therefore:

$$\frac{\sqrt{\langle(\Delta d)^2\rangle}_{Double\,fit}}{\sqrt{\langle(\Delta d)^2\rangle}_{Autocorrelation}} = \sqrt{\sqrt{2}} \qquad (6.7)$$

This can be understood intuitively: the localization improvement is a result of the doubled number of photons used to localize the correlated peak; the signal processing of each original peak involves half the number of photons used by the correlation process in which the photons from both individual signals are considered. However, the localization precision is not improved by a factor of $\sqrt{2}$ as expected when the number of photons is doubled, because the multiplication process translates into a precision loss. Note that by performing a correlation process on an acquired data with two independent signals, the information about the locations of the peaks is lost, yet, the distance between the peaks can be easily extracted which is sufficient in our scenario.

To support our derivation, we performed a numerical simulation of the localization process. We generated many Brillouin spectra with two Gaussian shaped signals (resembling the Stokes and anti-Stokes peaks), and assigned a Poisson noise behavior to each signal. We determined the distance between the signals both by localizing them using a fit for two Gaussians and by performing an autocorrelation and localizing a single side peak. Figures 6.2(a) and 6.2(b) show the result for signals of widths 2 and 5 pixels respectively. It can be seen that the red curve corresponding to the autocorrelation fit has a smaller standard deviation than the blue curve which was obtained using a double peak fitting. To better observe the differences we plotted a histogram

of both curves, as expected, the red curve transforms into a sharper and narrower histogram (fig. 6.2(a,b) insets). To compare our simulation results to the expected theoretical ones we measured the standard deviation for many sets of measurements and calculated the precision improvement which is the ratio of the standard deviations of the fitting results. We used a signal width of 2 (fig. 6.2c) and 5 (fig. 6.2d) pixels for this simulation and found an average accuracy improvement of ~18 % and ~17 % respectively, in good agreement with the theoretical prediction (fig. 6.2(c,d), red dashed line).
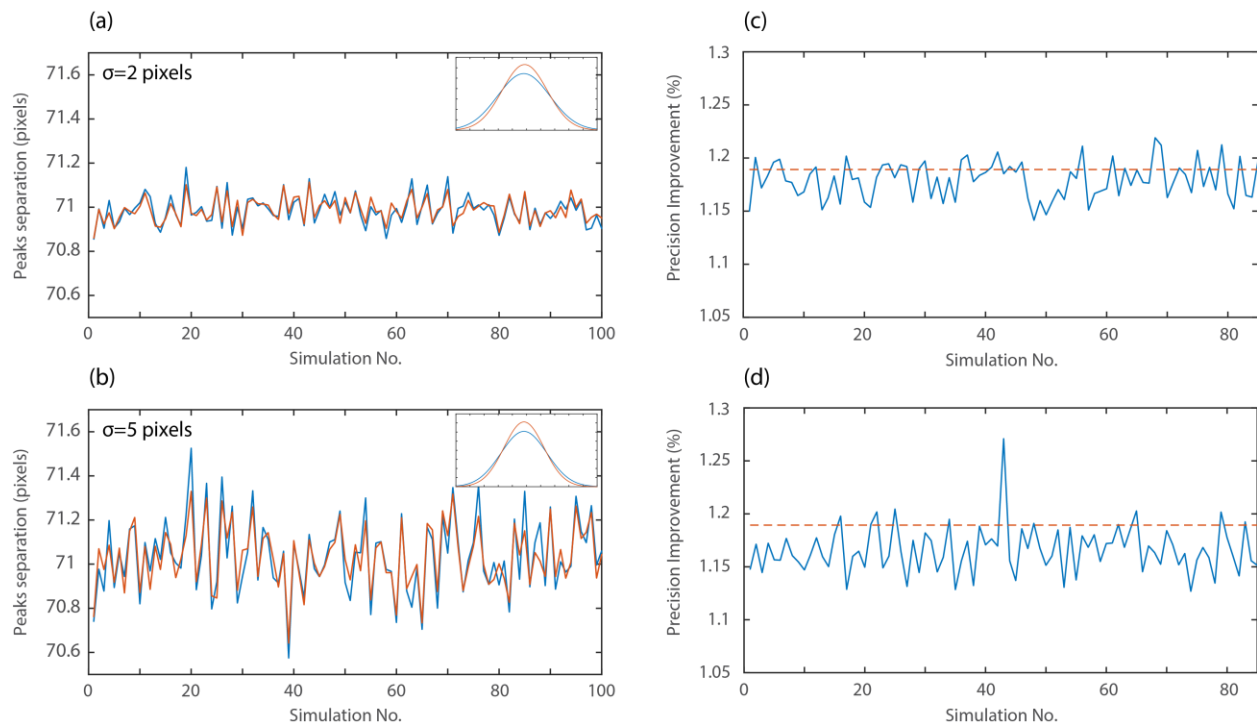
Figure 6.2: Simulation results: (a) Two peaks 2 pixels wide were repeatedly generated, and the distance between them was measured using a double peak fitting (blue curve) and a single fit of the autocorrelation function (red curve). The inset shows the corresponding histogram for the two measurements. (b) A similar measurement as in (a), with 5 pixels wide peaks. (c) The standard deviation of the data presented in (a) was measured repeatedly and the ratio between the standard deviations of the two analyses was quantified (blue curve). The theoretical expected improvement (red dashed line) is in good agreement with the simulated results. (d) A similar measurement as in (c), with 5 pixels wide peaks.

Here we derived and studied numerically the localization precision of two identical signals, since, due to error propagation considerations, it is preferable to set the system to yield identical signals rather than having an uneven photon distribution.

6.4 Experimental Data

To verify experimentally our results, we built the setup illustrated in figure 6.3a. We expanded a single frequency laser beam of wavelength 532 nm (LaserQuantum), and transmitted it through a polarizing beam splitter (PBS) and a quarter wave-plate. We focused the beam onto a sample using a one inch lens (f=50mm). The back reflected light was collected in an epi-detection configuration, and after a second transmission through the quarter wave-plate it acquired a polarization state of 900 with respect to the incoming beam. We used the polarizing beam splitter to direct the reflected light into the back entrance of an objective lens (20X, 0.4NA) and coupled it into a single mode fiber. The output of the fiber was spectrally analyzed using a double stage VIPA spectrometer with a 30 GHz free-spectral-range (for details see reference (Edrei et al., 2017a)).

Figure 6.3b shows a representative spectrum acquired using methanol as a sample (blue dots), and a matching double peak fit (red curve). The autocorrelation of the spectrum acquired in fig 6.3b is presented in fig 6.3c (blue dots), as well as a matching single fit (red curve). To quantify the localization precision in both cases, we repeated the measurement 500 times and presented the histogram of the fluctuations in figure 6.3d. As predicted previously, the precision of the single autocorrelated peak is higher resulting in a narrower histogram (fig 6.3d, red curve) compared with the double fitting of the acquired spectrum (fig 6.3d, black curve).

In the analytical derivation and the numerical simulation, it was assumed that every pixel of the signal is shot-noise limited. However, in practice, background noise is inevitable. To

examine the effect of background noise on our results we repeated the numerical study with varying levels of signal to background ratios (SBR). To do so, we varied the total number of photons in every peak within the simulation from 100 to 3500, a range similar to the experimental one, and used a constant background of 1 photon which is a typical experimental value with high-end CCD or sCMOS cameras. Figure 6.3e shows the localization precision improvement due to the autocorrelation process as a function of the SBR (blue curve), and theoretical shot-noise limited improvement (red dashed line). We found that for high SBR values the improvement approaches the theoretical prediction, while for SBR<20 the correlation process becomes less accurate than the double fitting procedure. To confirm this prediction, we repeated the experimental study with different SBR values by adjusting the integration time of the camera and found a good agreement with the simulated plot (fig 6.3e, black dots). In realistic experimental situations, the localization of the autocorrelation peak yielded $\approx$ 15 % higher precision than the double fit analysis.
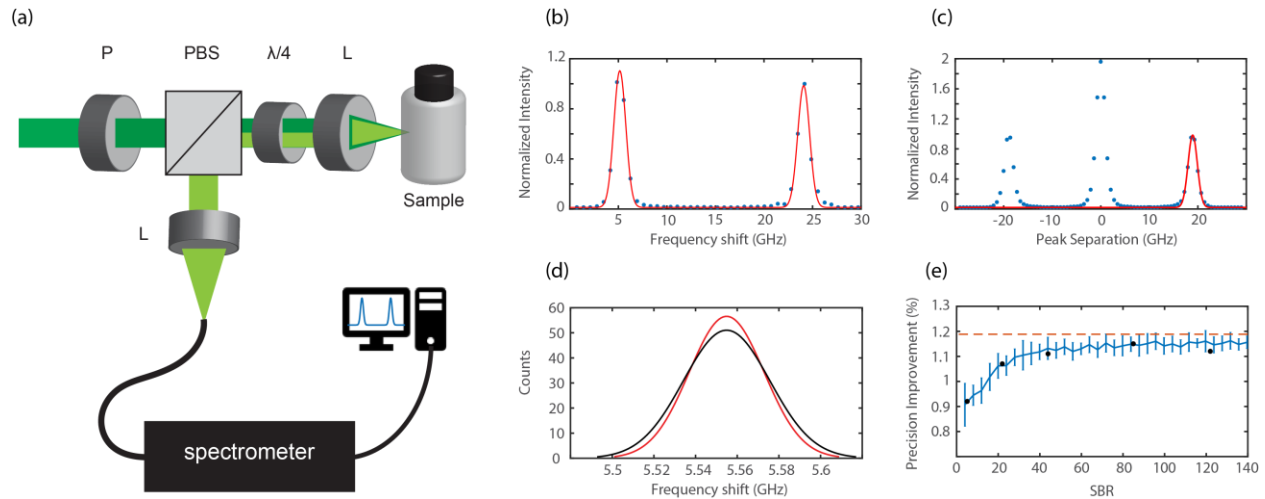
Figure 6.3: (a) Experimental setup: an epi-detection configuration was used to illuminate the sample (dark green path) and collect the back scattered light (bright green path). The collected light was spectrally analyzed using a double stage VIPA spectrometer. (b) A typical acquired spectrum of a methanol sample – blue dots (laser intensity ~10 mW, 40 msec integration time), and a double peak Gaussian fit – red curve. (c) The autocorrelation function of the spectrum shown in (b) – blue dots, and a single peak fit of the side peak – red curve. (d) A histogram of the separation between

the peaks shown in (b) for 500 measurements (black curve), and a matching histogram of the distance of the side peak in (c) from the center of the autocorrelation function (red curve). (e) Background effect on the precision improvement: at low SBR values the autocorrelated process is less accurate than the double fitting one, while at high SBR values the precision improvement (blue curve) approaches the theoretical one (red dashed line). The experimental data (black dots) agree with the numerical simulation (blue curve).

6.5 Discussion

The precision to which an optical signal can be spatially localized has been studied for many years (Thompson et al., 2002), and is the underlying principle for super-resolution localization microscopy techniques such as PALM (Betzig et al., 2006) and STORM (Rust et al., 2006). Brillouin spectroscopy also uses this type of localization process thus achieving spectral sensitivities that are much higher than the nominal spectral resolution of the spectrometer. However, Brillouin spectroscopy presents a peculiar situation where the relevant quantity is the distance between two acquired signals rather than the absolute location of a single peak. In these conditions, autocorrelation functions are particularly suitable for signal analysis. By transforming to the autocorrelation space, the spatial form of the original function is lost, however, the information regarding the distances between locations is preserved. Here we have shown that the localization process yields higher precision when applied to the autocorrelation function instead of the original signals.

We have compared the current method of spectral analysis to the autocorrelation both theoretically, numerically and experimentally. The analytical derivation predicts an improved precision of ∼ 18.9 % for the autocorrelated analysis, which is in good agreement with our experimental data. For instance, for the data presented in figure 6.3(b-d) we measured the width of the original signal to be ~850MHz, while the localization precision obtained by the double

fitting process was ~41.1 MHz and the precision of the fit of the autocorrelated data gave an advantage of ∼ 15 %, i.e: 35.7MHz. We also found that, the background imposes a limit on the expected improvement obtained by the autocorrelation processing. Indeed, we found that at low SBRs autocorrelation ceases to provide an advantage. This effect is attributed to the fact that through the autocorrelation process background photons from all locations within the spectrum contribute to the signal localization. Hence, using the autocorrelation analysis will be advantageous only when applied to high SBR scenarios, while for low SBR measurements such as within scattering medium the double fitting approach will yield a higher localization precision.

Previous studies on localization precision have shown the dependency of the final sensitivity on acquisition parameters such as the number of detected signal and background photons as well the ratio between the camera pixel size and the point spread function of the signal (Thompson et al., 2002, Ober et al., 2004). In terms of signal photons, the Brillouin spectroscopy application poses strong constraints in the spontaneous regime; in this chapter, we have used realistic parameters of ~3000 total number of photons per peak which is about what is obtained in typical samples with a few mW incident light and 100ms of integration time; as of background photons, these limits are imposed by the camera utilized and the experimental setup, we used an EMCCD camera (Andor iXon 897) with an intrinsic background noise <1 photon, hence, in our simulation we used an upper limit background of 1 photons. As for the ratio between the camera pixel size and the point spread function of the signal, it has been shown that the optimal choice depends on the specific parameters as well as the dimensionality of the measurement (Thompson et al., 2002). In order to evaluate the effect of the autocorrelation on this behavior we used a Monte Carlo simulation to generate signals with different ratios of pixels-to-PSF widths using the above-mentioned parameters. The results are presented in figure 6.4. Both the autocorrelation analysis

(red) and the double fitting approach (blue) yielded a similar optimal ratio of $\sim 4 \; pixels \; per \; PSF$ while preserving the $\sim 20 \, \%$ precision improvement of the autocorrelation process. We also compared the simulated results to the analytical expectation derived in [30], as presented in the black dashed line in figure 6.4. It can be seen that the analytical expectation is in good agreement with the simulated results for small pixels, as the pixels become larger there is an underestimation of the localization error which is a result of a first order approximation approach of the analytical derivation see [30].
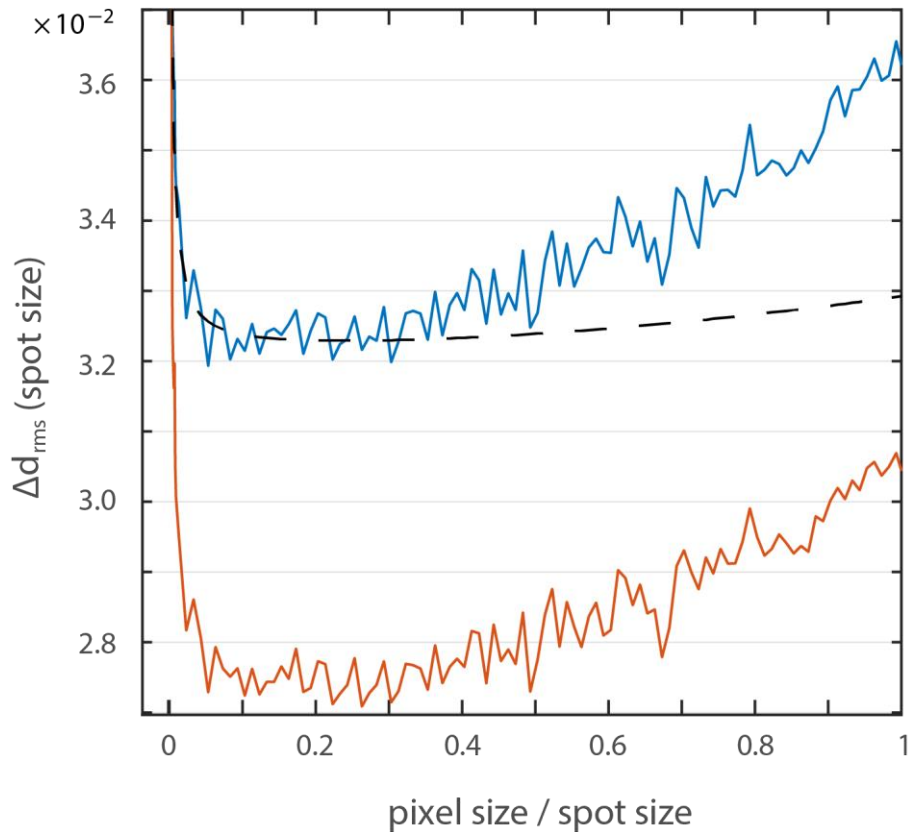
Figure 6.4: Monte Carlo simulation of peak localization precision (percentage of the spot size) as a function of the ratio between the pixel size and the spot size for the double fitting analysis (blue) and the autocorrelation analysis (red). The simulated results present similar behavior to the theoretical expectation (black dashed line) for small pixels sizes.

It should be noted that figure 6.4 is a proper estimation of the localization precision for a one-dimensional spectral scenario, for a two-dimensional case the optimal point is obtained at $\sim2\ pixels\ per\ PSF$. Another consideration for Brillouin spectral localization is that different materials have different linewidths, therefore a compromise needs to be reached by choosing spectrometer alignment that fits best the material under examination.

Chapter 7

Adaptive optics in spectroscopy and densely-labeled-fluorescence applications[*]

Even if the extinction issue is adequately treated as shown in chapter 5, the Brillouin signal will still degrade deep within samples due to scattering and aberrations. Adaptive optics systems have been integrated in many imaging modalities to correct for aberrations introduced by samples and optical elements. In most cases, the optical system has access to a guide star, i.e. a point-like structure smaller than the diffraction limit, which can be used as a beacon for adaptive optics enhancement. In contrast, in spectroscopy and in densely-labeled fluorescent samples, the signal is diffused throughout the entire beam path and is not confined to a well-defined point-like structure. In this chapter we show, analytically and experimentally, that in these scenarios adaptive optics systems are expected to yield significantly lower signal enhancement than when a guide star is available. We discuss the performance degradation of adaptive optics for different imaging modalities (e.g. confocal, multi-photon microscopy) and identify solutions to overcome low signal enhancements.

---

[*] The results of this chapter were submitted for publication and are under peer review.

7.1 Background

Optical imaging modalities often suffer from degraded performances due to aberrations and refractive index mismatches within the optical path. This long-standing issue was first addressed by astronomers who developed and implemented Adaptive Optics (AO) systems in ground-based telescopes to measure and correct atmospheric aberrations and enable diffraction limited images of distant stars (Beckers, 1993). Following the success achieved by AO in astronomy, the same concept was applied to ocular imaging to enable aberration-free imaging of retinal photoreceptors (Roorda and Williams, 1999, Roorda et al., 2002). In the past two decades AO techniques have been extensively applied to a variety of optical microscopy modalities such as wide field (Azucena et al., 2011, Li et al., 2015), confocal (Booth et al., 2002), multiphoton (Débarre et al., 2009, Wang et al., 2015b, Wang et al., 2014b) and super-resolution (Booth et al., 2015, Zheng et al., 2017).

Adaptive optics systems have improved the capabilities of optical microscopes to approach their optimal performances by improving image contrast and resolution as well as enhancing the signal-to-noise ratio (SNR) defined as: $\frac{\langle Signal \rangle}{\langle \Delta Signal \rangle}$. However, the extent to which AO can improve image quality is highly variable in the literature. Reported signal enhancements range from few percent to more than ten-fold (Zheng et al., 2017, Ji et al., 2010, Wright et al., 2007, Edrei and Scarcelli, 2018a, Thompson et al., 2016). The different performances can only partially be attributed to system parameters (e.g. finite spatial and temporal resolutions, photon noise, isoplanatism), especially because modern tools, such as phase modulators operating at a kHz rate with thousands of degrees of freedom and low noise cameras, can effectively address system-related aberrations. In this context, in fluorescence microscopy applications, the labeling density or the size of the "guide star" have been observed to strongly affect AO performances (Ji et al.,

2012), but the mechanism of such dependence has not been described thus hindering the ability to implement effective improvements to AO protocols.

Here we analyze the dependence of AO performances on labeling density both theoretically and experimentally in the context of confocal microscopy and demonstrate how it dramatically affects the ability of AO systems to enhance signal intensity. In practical scenarios, the degradation of AO performances is particularly relevant in microscopy when fluorescent labeling is diffused within the sample (i.e. fluorescent sea) and it is difficult to ensure the existence of a single fluorescence bead within the illumination path, or in spectroscopy measurements where the signal can arise from any location within the illumination path. We show that, in the context of confocal microscopy and spectroscopy of diffused signals, epi-detection configurations do not properly estimate optical aberrations in the system and have little sensitivity to proper image quality metrics; as a result, AO protocols are destined to suboptimal results in these scenarios. To quantify this effect, we analytically model the degradation of AO signal enhancement in a 'fluorescent sea' scenario compared to a point-like guide star and experimentally verify the prediction described by our model. Using aberrating layers we characterize the challenge presented by diffused signals when AO procedures are applied. We further compare the situation of confocal microscopy with multi-photon microscopy and describe potential solutions for future improvements.

7.2 Experimental configuration

Image formation in fluorescent confocal microscopy is based on imaging a focal point within the sample onto a confocal plane where a pinhole is placed to reject out-of-focus light. Scanning such focal point within the sample and mapping the intensity measured behind the pinhole yields the image. The pinhole can be a mask, typically a circular aperture of fixed diameter; alternatively, a CCD camera can be placed in the confocal plane and the intensity from only pre-selected pixels is

detected (Huff, 2015, York et al., 2012). The most common configuration for confocal microscopy is in epi-detection where illumination and collection light utilize the same objective lens. Under these circumstances, the focal point generated through a sample is imaged back onto the confocal plane of the pinhole through the same light-path. In this situation, if the sample can be regarded as a 'fluorescent sea', when performing a confocal scanning, the intensity distribution at each point in the confocal plane does not reveal the intensity distribution of the corresponding point scanned within the sample but its autocorrelation (Artal et al., 1995b). This interesting phenomenon can be intuitively understood: when an infinitely small fluorescent bead is excited within the sample, the intensity revealed in the confocal plane is the convolution of the detection path with a delta function [Fig. 7.1(a)]; for identical illumination and detection paths, this yields the inverse of the illumination PSF. In contrast, when every point in the sample generates fluorescence [Fig. 7.1(b)], we do not have access to the intensity distribution of "a single point" of the sample; instead, in the confocal plane, the intensity distribution of "a single point" in the sample is the convolution of the detection path with the "single point" as created by the illumination path. Because the illumination path and detection path are identical but inverted optical systems, the final image on the confocal plane is a convolution of the intensity distribution on the sample with an inverse version of itself, which is the autocorrelation. This property has important consequences for signal enhancement within AO systems as we will see next.
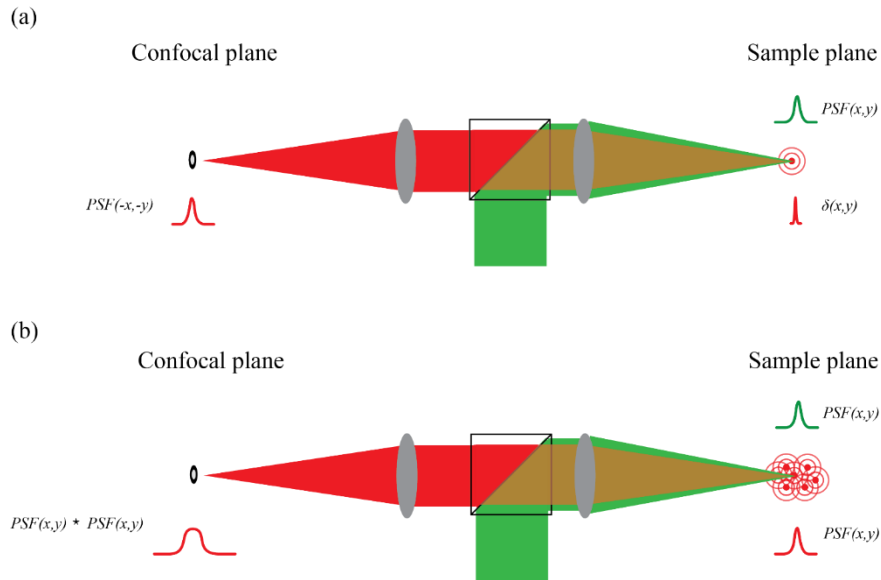
Fig 7.1. Schematics of a confocal configuration focused on a fluorescent bead (a) or on a fluorescent sea (b). The sample plane is back imaged onto the confocal plane generating either an inverse PSF (a) or the autocorrelation of the PSF (b).

We demonstrated this important property experimentally with the setup in Fig. 7.2(a). We expanded a polarized Ar-Ion laser beam (Edmund optics, λ=514nm) and reflected it off the surface of a spatial light modulator (SLM, Hamamatsu X10468). We imaged the plane of the SLM using a 4-f imaging system (L1, L2, f=150mm) onto the back plane of an objective lens (L3, 4X 0.1NA) and focused it onto a fluorescent sample (Rhodamine B solution, Sigma). The fluorescent focal point generated at the sample was imaged using two arms: one in transmission and one in epi-detection. In the transmission arm we collected the light using an identical objective lens as the one used for focusing (L4, 4X 0.1NA), and imaged the focal point onto a camera (camera 1) using a second lens (L5, f=200mm) in an infinite conjugate imaging system. In the epi-detection arm we used the back-emitted light to image the focal point; in this arm, the collected light is reflected again off the SLM surface before being focused onto the camera (camera 2), hence, any aberration presented by the SLM will be sampled twice throughout the back-and-forth paths of light. In both arms we placed an emission filter to block the excitation laser from hitting the camera. The

transmission arm of the setup in Fig. 7.2 can measure the true intensity distribution at the sample, as it directly captures the pattern before it is reimaged onto the confocal plane. The epi-detection arm of the setup in Fig. 7.2 features camera 2 where one would place a confocal pinhole to reject out-of-focus light and thus allows us to study a confocal microscopy configuration and a 'fluorescent sea' as a sample.

To demonstrate the key feature of this configuration, i.e. the detection of the autocorrelation of the sample intensity distribution on the confocal plane, we used the SLM to shape the illumination light and generate a letter 'M' in the sample plane. We then recorded the intensity distribution in both cameras: in transmission (camera 1) we observed the well expected letter 'M' [Fig. 7.2(b)]; in the epi-detection arm (camera 2), as expected, we observed the autocorrelation of the 'M' pattern [Fig 7.2(c)] as it is clear by comparing it with the computed autocorrelation image [Fig. 7.2(d)].
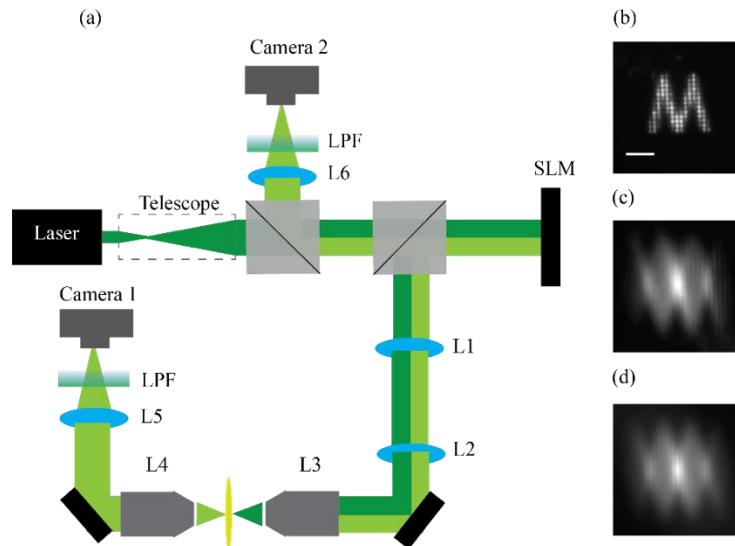
Fig 7.2. (a) Setup: The excitation beam (dark green) is reflected off the SLM surface and focused onto a 'fluorescent sea' sample. The emission light (bright green) is collected both is transmission (camera 1) and in reflection/epi-detection (camera 2). Only the reflected light is back imaged onto the SLM surface before being captured by the camera. (b) An artificial aberration of the letter 'M' generated by the SLM and captured in transmission by camera 1 (scale bar = 60 µm). (c) The

intensity distribution as captured in epi-detection by camera 2. (d) The computed autocorrelation of the letter 'M' presented in (b).

We note that although the aberration in our setup was introduced at the pupil of the objective lens (by conjugating it with the SLM plane), it is equivalent to a scenario where the aberration is introduced between the objective lens and the focal plane. In both cases the intensity distribution at the focal plane will correspond to the power spectrum of the aberration phase map (Goodman, 2005).

In the same way the intensity distribution on the sample focal plane is not faithfully reproduced in the confocal plane of epi-detection microscopes, any aberration introduced by the sample or optical system will not be probed properly when viewed through the epi-detection path; indeed, it will be detected as an autocorrelation of its intensity distribution. To demonstrate this concept, we used the setup in Fig. 7.2, focused light into a single point on the fluorescent sample and introduced four primary aberrations (astigmatism, defocus, coma and spherical) through the SLM. Fig. 3 shows the result of the aberrated intensity distributions as recorded by the transmission and epi-detection arms. Fig. 7.3(a) shows the aberrations introduced by the SLM, Fig. 7.3(b) shows the resulting intensity distribution recorded through the transmission arm (camera 1), Fig. 7.3(c) shows the intensity distribution recorded using the epi-detection arm (camera 2). For comparison, the autocorrelations of the patterns of Fig. 7.3(b) were numerically computed and are presented in Fig 7.3(d).
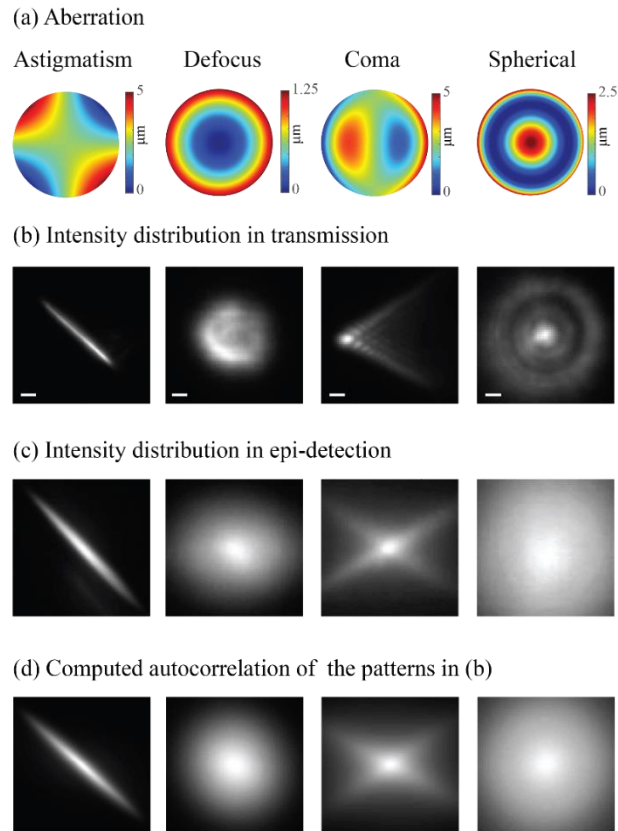
Fig 7.3. (a) Four primary aberrations projected by the SLM. (b) The intensity distribution captured in transmission by camera 1 (scale bar = 10 µm). (c) The epi-detection intensity distribution recorded by camera 2. (d) The computed autocorrelation functions of the intensity distribution presented in (b).

Fig. 7.3 emphasizes the marked difference between the true illumination pattern generated within the sample (i.e. the transmitted pattern) and the pattern as measured in epi-detection. If a pinhole were to be placed in the confocal plane (i.e. the location of camera 2), the detected light would not be a proper representation of the actual illumination pattern generated within the sample. Instead, the pinhole will sample the intensity at one location of the autocorrelation function, which is poorly sensitive to local intensity changes and therefore less affected by the AO procedure as we will later show and quantify.

7.3 Results

We set out to demonstrate how the epi-detection path on the confocal plane is not sensitive to the intensity variations in the sample plane and thus results in suboptimal AO enhancement. First, we show that using the epi-detection arm as feedback for AO procedure leads to faulty estimation of the aberration and decreases AO enhancement. To do so, within the setup, we introduced an aberration by spreading transparent glue on a microscope slide and inserting it between the objective lens (L3) and the fluorescent substrate thus causing a deformation of the focal point. We applied an iterative algorithm to correct for the induced aberration. The algorithm was designed to enhance a single point on the image by measuring the intensity response to the projection of each Zernike polynomial and its' inverse from which the coefficient value was estimated (Booth et al., 2002, Edrei and Scarcelli, 2018a). As feedback we compared using the maximal intensity of the image in the transmission path (i.e. true feedback) vs the maximal intensity as measured in the epi-detection path (i.e. the autocorrelation feedback). The transmission image feedback procedure can be considered equivalent to a procedure using a small point-like guide star. The transmission image feedback yielded highly repeatable results for ten different trials: the coefficients of the calculated Zernike modes showed small variations [Fig. 7.4(a)], the average of all phase maps had a clear structure [Fig. 7.4(b)] and the procedure resulted in ~2-fold enhancement of the focal intensity [Figs. 7.4(c) and 7.4(d)]. Instead, using the epi-detection feedback, each repetition of the algorithm yielded a different set of Zernike coefficients, with large variations [Figure 7.4(e)]. The average phase map obtained using the epi-detection arm appeared flat as the different iterative processes yielded uncorrelated phase maps [Fig. 7.4(f)] and a negligible increase in intensity was obtained [Figs. 7.4(g) and 7.4(h)].
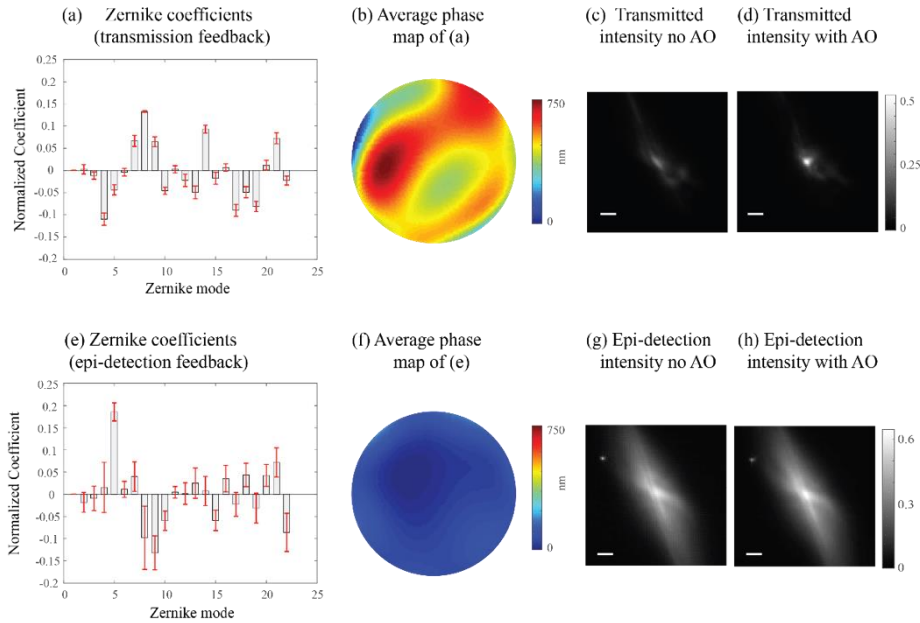
Fig 7.4. (a) The Zernike coefficients obtained by the algorithm using the transmission arm (camera 1) as feedback. (b) The average phase map of the coefficients from (a). (c) The initial intensity distribution recorded by camera 1 through the glue aberration (scale bar = 15 µm). (d) The final intensity distribution recorded by camera 1 after projecting the phase map shown in (b). (e) The Zernike coefficients obtained by the algorithm using the epi-detection arm (camera 2) as feedback. (f) The average phase map of the coefficients from (e). (g) The initial intensity distribution recorded by camera 2 through the glue aberration (scale bar = 15 µm). (h) The final intensity distribution recorded by camera 2 after projecting the phase map shown in (f).

Next, we show that even when a significant enhancement is obtained at the sample plane (for example using true transmitted intensity as feedback or using a truly point-like guide star), such enhancement is not captured by the epi-detection arm. To do so, we introduced again an aberration by spreading transparent glue on a microscope slide and inserting it between the objective lens (L3) and the fluorescent substrate and obtained a deformed focal point [Fig 7.5(a)]. Then we applied the same iterative algorithm as before to correct for the induced aberration using the maximal intensity of the image in the transmission path as feedback. The procedure resulted in ~2-fold enhancement of the focal intensity [Figs 7.5(b) and 7.5(c)]. We then recorded the intensity

distribution of the epi-detection arm before and after the enhancement process [Figs 7.5(d) and 7.5(e) respectively]. On the epi-detection arm only $\sim 20\,\%$ enhancement was observed [Fig. 7.5(f)], i.e. a "point-like guide-star" enhancement at the sample plane would have yielded 5-fold greater enhancement than the one indicated by the epi-detection image at the confocal plane.
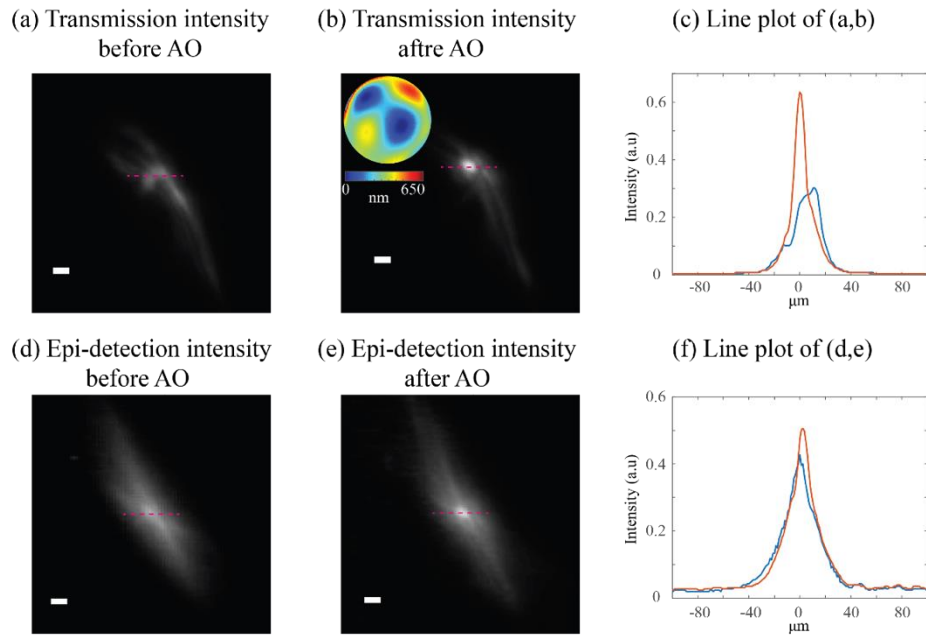
Fig 7.5. (a) Intensity distribution recorded in transmission (camera 1) through the glue aberration (scale bar = 12 µm). (b) The intensity distribution in transmission after performing the AO optimization using the transmission arm as a feedback. The inset shows the final phase map projected by the SLM. (c) A line plot comparing the peak of the intensity distribution without (blue) and with (red) AO. (d) Intensity distribution recorded in epi-detection (camera 2) through the glue aberration. (e) The intensity distribution in epi-detection after performing the same AO optimization as in (b), i.e. the same phase map as shown in the inset of (b) was applied here. (f) A line plot comparing the peak of the intensity distribution without (blue) and with (red) AO.

7.4 Analytical model

To understand the phenomenon in depth, we built a model using the experimental scenario of Fig. 7.5, i.e. we compared the true intensity enhancement achieved on the sample plane (obtained either

using the transmission arm feedback or using a point guide star) with the one observed by the epi-detection arm. The aberration introduced by the sample enlarges the diffraction limited spot and spreads its intensity I_{tot} onto a larger area; here, we denote this area to be N times larger than the diffracted limited spot and for simplicity we treat it as discrete, i.e. the intensity is equally spread onto N diffraction limited points of intensity $I = I_{tot}/N$. Suppose one is able to achieve an enhancement of a single point through an AO procedure by a factor of 'k', i.e. the intensity at that given point is: $I_{center} = k \cdot I$. As the total energy does not change, all other points will have a reduced intensity of:

$$I_{other\ points} = I \cdot \left[1 - \frac{k-1}{N-1}\right] \qquad (7.1)$$

However, as previously demonstrated, the epi-detection microscope is not sampling the actual intensity at the sample plane, but its autocorrelation. Let's then compare the autocorrelation intensity before and after enhancement. Before the AO procedure, the central autocorrelation point had intensity:

$$\sum I^2(x, y) = N \cdot I^2 \qquad (7.2)$$

After the AO procedure, from Eq. 7.1 we can derive the intensity of the central autocorrelation point to be:

$$\sum I^2(x, y) = I_{center}^2 + (N - 1) \cdot I_{other\ points}^2 = (k \cdot I)^2 + (N - 1) \cdot \left(I \cdot \left[1 - \frac{k-1}{N-1}\right]\right)^2 \qquad (7.3)$$

As a result, the enhancement following AO procedure is obtained by dividing equations (7.3) and (7.2):

$$Enhancement_{EPI} = \frac{k^2 + (N-1) \cdot \left[1 - \frac{k-1}{N-1}\right]^2}{N} \qquad (7.4)$$

In the ideal scenario where the AO procedure can refocus all energy back into a single point, i.e. $k = N$, the autocorrelation is enhanced by k times, exactly reporting the same enhancement of the

sample plane. For $k \ll N$ the enhancement in epi-detection (i.e. equation (7.4)) reduces to 1 meaning that the AO enhancement is negligible in the autocorrelation plane. Equation 4 can be applied to the reported results of Fig. 7.5; the focal point shown in Fig. 7.5(b) is estimated to be ~100 pixels at FWHM, while the aberration prior to the enhancement [Fig. 7.5(a)] is estimated to be ~10 times larger. Hence, by substituting $k = 2, N = 10$ into Equation (7.4), the enhancement is 21 % in agreement with our experimental results.

The prediction given by our model is that for a given AO procedure (i.e. same k), larger aberrations/illumination (i.e. larger values of N) will yield smaller signal enhancement in the epi-detection arm significantly deviating from the true enhancement that one would obtain at the sample plane if accurate feedback were to be used. To verify this prediction, we generated an illumination pattern containing 9 discrete points [Fig. 7.6(a)] and, using the SLM, we enhanced the central point by a factor of ~6.5 [Fig. 7.6(b)]. On the epi-detection arm we observed a ~3-fold enhancement [Figs. 7.6(c) and 7.6(d)], i.e. approximately half of the enhancement value at the sample. Next, we generated a much wider pattern containing 193 points [Fig. 7.6(e)] and enhanced the central point by a similar ~6.5 factor [Fig. 7.6(f)]. As we expected, on the epi-detection arm in this scenario we observed only ~1.16-fold enhancement [Figs. 7.6(g) and 7.6(h)]. To quantitatively verify the predictions of our model, we then used a series of such patterns with different areas and for each pattern we enhanced a single point and compared the enhancement obtained in the transmission path (camera 1) with that obtained in the epi-detection path (camera 2). Consistent with our model, for wide intensity distributions the enhancement measured on the epi-detection path was much lower than the actual enhancement measured in the transmission path (i.e. in the sample plane). However, as the intensity distribution area decreased, the enhancement in the epi-detection arm approached the actual enhancement value in the sample plane, [Fig. 7.6i, blue dots].

We fitted the experimental data to our model; the ratio between the actual and observed enhancements can be obtained by dividing Equation (7.4) by k. Leaving k as a free parameter we found the data to be in good agreement with the model [Fig. 7.6(i), red line] and the value of k was calculated by the fitting process to be 6.51.
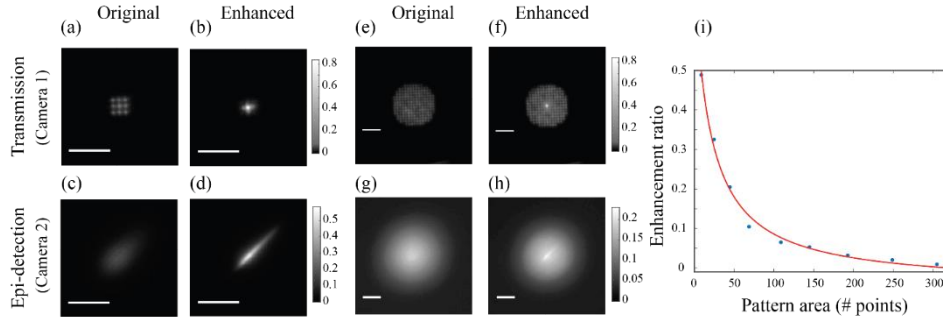
Fig 7.6. (a) An artificial aberration composed out of 9 identical points (scale bar = 60 µm). (b) The central point in (a) was enhanced by ~6.5-fold. (c, d) The intensity distribution of (a) and (b) respectively as seen in epi-detection. (e) An artificial aberration composed out of 193 identical points (scale bar = 60 µm). (f) The central point in (e) was enhanced by ~6.5-fold. (g, h) The intensity distribution of (e) and (f) respectively as seen in epi-detection. (i) The enhancement ratio between the true enhancement on the sample (recorded in transmission) and the enhancement observed in epi-detection for varying sizes of aberrations (blue dots). The data agrees with the prediction of our model as seen by the red plot.

7.5 Discussion

In ophthalmology applications, it has been known that when a double-pass configuration is used to measure the aberrations of the eye from retina reflections using a wave front sensor, the measurement will yield a false phase map (Artal et al., 1995b). This failure of the wave-front measurement is caused by the light passing twice through the same aberrating medium which causes the phase variations of even aberrations to double while odd aberrations cancel out. A

100

similar phenomenon is described here, in the realm of confocal fluorescence microscopy or spectroscopy. For biomedical applications, the double pass configuration offered by epi-detection is an important feature that enables access to the sample from just one side, while providing high 3D resolution. In such configuration, if a signal can arise from any locations within the sample without point-like guide stars, direct measurement of the phase map is prone to failure. In fluorescent microscopy, to avoid measuring the phase map directly, image-based AO approaches have been applied where the phase aberration is estimated by enhancing some image parameter such as the maximal intensity (Booth, 2014, Ji, 2017). Such indirect approaches have been shown to be successful in scenarios where direct wave-front measurements fail (e.g. within scattering materials (Ji, 2017)) because they are not bounded by the limited ability of a wave-front sensor to accurately measure the phase aberrations.

Here we showed that also image-based AO approaches fail in this experimental scenario: in a 'fluorescent-sea' scenario, the intensity response through the double pass (i.e. epi-detection) path is much lower than the true enhancement that could be obtained at the sample. This lack of sensitivity to intensity variations will yield poor results when the confocal intensity is used as an indicator for an iterative phase correction. Accordingly, denser labeled fluorescent samples and spectroscopic measurements are expected to yield lower improvements of image quality when AO procedures are applied.

In the context of two photon microscopy, Na Ji et al (Ji et al., 2012) have reported a similar trend where increase in the size of guide star leads to a decrease of signal enhancement via AO. This observation is probably dominated by a different phenomenon as the illumination and detection paths are distinct in multiphoton setups. In two photon microscopy a thick and densely labeled sample should provide the same amount of light emission regardless of the focal quality;

in fact, while tightly focused beams provide high photon flux within the illuminated voxel, increasing the illumination area compensates the intensity loss at the focus by increasing the volume from which the signal can originate (Katz et al., 2014b). Hence, with highly dense samples, a poor AO enhancement is expected because focal confinement does not affect the signal intensity. The signal from higher order non-linearity processes such as three photon emission is better suited for densely labeled samples (Horton et al., 2013).

To overcome the problem arising from the identical illumination and detection light paths in a double-pass configuration, Artal et al. had suggested to make the illumination path smaller and under-fill the objective lens (Artal et al., 1995a). In this configuration, light is aberrated by the sample only once, which enables the correct phase map measurement. However, in context of confocal microscopy, this solution may not be viable because the confocal modality relies on the tight focusing of the illuminating beam. Different approaches can potentially provide a better framework for enhancement in this case. For example, coherence gating allows to collect light from a confined region within the sample, which can mimic the existence of a guide star and avoid the 'fluorescent sea' scenario (Rueckel et al., 2006). Similarly, a wave front sensor can be placed after the confocal pinhole, which rejects light from surrounding regions (Rahman and Booth, 2013). These solutions were shown to enable a better estimation of the aberrations measured from a reflecting surface and can be also applied in the context of fluorescent sea, yet they are difficult to implement and require delicate alignment and careful choice of specifications such as broadened emission or confocal pinhole adjustment. A viable approach is to work in a dual-axis configuration so that the detection arm samples light only from a small region within the illuminated sample (Liu et al., 2007). Such a configuration was shown to enable significant AO enhancement in confocal Brillouin spectroscopy, which represents an extreme 'fluorescent sea' scenario (Edrei and

Scarcelli, 2018a). Computational approaches to handle the complexity provided by the autocorrelation outcome in the image plane such as phase-retrieval algorithms (Iglesias et al., 1998) or minimizing the area of the autocorrelation intensity distribution as recently suggested by G Stern et al. (Stern and Katz, 2018) can also provide a way to overcome the problem.

Chapter 8

Brillouin micro-spectroscopy through aberrations via sensor-less adaptive optics[*]

Brillouin spectroscopy performances are rapidly degraded by optical aberrations and have therefore been limited to homogenous transparent samples. Following the conclusions of chapter 7, in this chapter we developed an adaptive optics (AO) configuration designed for Brillouin scattering spectroscopy to engineer the incident wave-front and correct for aberrations. Our configuration does not require direct wave-front sensing and the injection of a 'guide-star'; hence, it can be implemented without the need for sample pre-treatment. We used our AO-Brillouin spectrometer in aberrated phantoms and biological samples and obtained improved precision and resolution of Brillouin spectral analysis; we demonstrated 2.5-fold enhancement in Brillouin signal strength and 1.4-fold improvement in axial resolution because of the correction of optical aberrations.

8.1 Background

For many decades, Brillouin light scattering spectroscopy, based on acoustic phonon-photon interaction (Boyd, 2008), has been a powerful optical technique in applied physics and material science due to its unique ability to characterize mechanical properties of materials at high spatial resolution without contact (Dil, 1982, Hartschuh et al., 2005, Benedek and Fritsch, 1966, Fleury and Boon, 1969, Koski et al., 2013). More recently, Brillouin spectroscopy combined with confocal microscopy has found biological applications in cell biomechanics (Scarcelli et al., 2015b, Elsayad et al., 2016, Zhang et al., 2017, Antonacci and Braakman, 2016, Meng et al., 2016, Mattana et al., 2017, Palombo et al., 2014), plaque characterization (Antonacci et al., 2015b) and is being tested in the clinic for ophthalmology applications (Besner et al., 2016, Scarcelli et al., 2015a). For Brillouin spectral measurements, two specifications are critical: due to the small spectral shift of Brillouin signatures, high spectral contrast (or extinction) is needed within spectrometers to eliminate noise from the incident laser or stray light; in addition, due to the small scattering cross-section of Brillouin interaction, the number of photons available for detection are fundamentally limited. Historically, spectrometers based on a cascade of Fabry-Perot etalons have provided sufficient extinction and resolution to detect and resolve Brillouin peaks (Meng et al., 2016, Dil, 1982); yet, measurements with multi-pass Fabry-Perot interferometers are time consuming and generally not practical for imaging and/or biomedical applications. More recently, spectrometers based on virtually-imaged-phase-array (VIPA) etalon were developed to enable rapid measurements of Brillouin spectra (Scarcelli and Yun, 2008, Scarcelli and Yun, 2011). A vast amount of effort was dedicated in the past years to increase the spectral extinction of VIPA-based spectrometers; this progress has led to measurements of Brillouin spectra in non-transparent materials with shot-noise limited performances (Fiore et al., 2016, Shao et al., 2016, Meng et al.,

2014, Antonacci et al., 2015a, Edrei et al., 2017a). Thus, the next frontier of Brillouin microscopy progress is to improve signal to noise ratio (SNR) of Brillouin spectral measurements. In this context, multiplexed detection configurations (Zhang et al., 2016) or improved spectral processing methods (Edrei et al., 2017b) have been explored as well as signal enhancement by stimulated Brillouin scattering process (Ballmann et al., 2017, Remer and Bilenca, 2016a). All these methods, though, do not address the degradation of Brillouin signal due to optical aberrations. Aberrations are significant and unavoidable within optical systems, due to optical elements, sample inhomogeneity and refractive index mismatches (Booth, 2014); hence, they impose a fundamental limitation on current capabilities of Brillouin spectrometers.

To address this limitation, we have developed a confocal Brillouin micro-spectrometer integrated with an adaptive optics (AO) system. AO is designed to measure and correct optical aberrations (Tyson, 2015, Ji, 2017) and has had great success in astronomy and ocular imaging providing aberration-free images of exosolar scenes (Hardy, 1998) and retinal photoreceptors (Roorda et al., 2002, Roorda and Williams, 1999). Over the past twenty years, the progress of AO techniques has pushed imaging capabilities towards their fundamental limit, by enhancing SNR and providing higher resolution and contrast (Booth, 2007). These advances have been traditionally focused to imaging modalities such as optical coherence tomography (Hermann et al., 2004, Zawadzki et al., 2005), wide-field fluorescence (Mertz et al., 2015, Azucena et al., 2011, Jorand et al., 2012, Li et al., 2015), confocal (Booth et al., 2002, Booth et al., 1998, Wang et al., 2015b, Tao et al., 2011b) and multiphoton microscopy (Ji et al., 2010, Wang et al., 2014b, Sinefeld et al., 2015, Débarre et al., 2009, Wang et al., 2015b, Turcotte et al., 2017, Wright et al., 2007). In this work, we present an AO-Brillouin confocal system, designed to enhance the signal and resolution of Brillouin-based elasticity mapping through the correction of aberrations.

8.2 Setup and optimization process

AO techniques can be classified in direct and indirect methods. Typically, direct methods use a wave-front sensor to measure the aberration while indirect methods either apply an iterative process to estimate the aberration or calculate the aberration from an acquired image. Direct approaches are faster because a single acquisition is needed to measure the phase aberration; however, the wave-front measurement requires a guide-star at the measured location, which may be difficult to introduce, especially in vivo (Ji, 2017). In this work, we adopted an iterative indirect AO approach. Our optimization process is based on the acquired Brillouin signal and therefore does not require a 'guide star'. We used a confocal microscope system connected to a Brillouin spectrometer through an optical fiber working as a confocal pinhole. We placed a Spatial Light Modulator (SLM) within the illumination path of the confocal system; to enhance the Brillouin signal, we monitored the Brillouin spectrum intensity while varying the phase introduced by the SLM. The enhancement mechanism can be understood by considering the confocal configuration as shown in figure 8.1(a). Without aberrations, most of the Brillouin photons are generated at the illumination focal point which is conjugated to the confocal pinole (fig 8.1(a), first row), and therefore are transmitted to the spectrometer. However, an aberration within the optical path will disperse the incident light energy over a larger volume and generate the Brillouin photons at various locations which are blocked by the confocal pinhole leading to a degraded signal (fig 8.1(a), second row). By correcting the aberration using a SLM, the focal point can be retrieved (fig 8.1(a), third row). Although aberration correction improves by optimizing also the collection path leading to the confocal pinhole (Booth, 2014, Ji, 2017), here we modified only the illuminating beam to improve overall throughput and minimize optimization time.
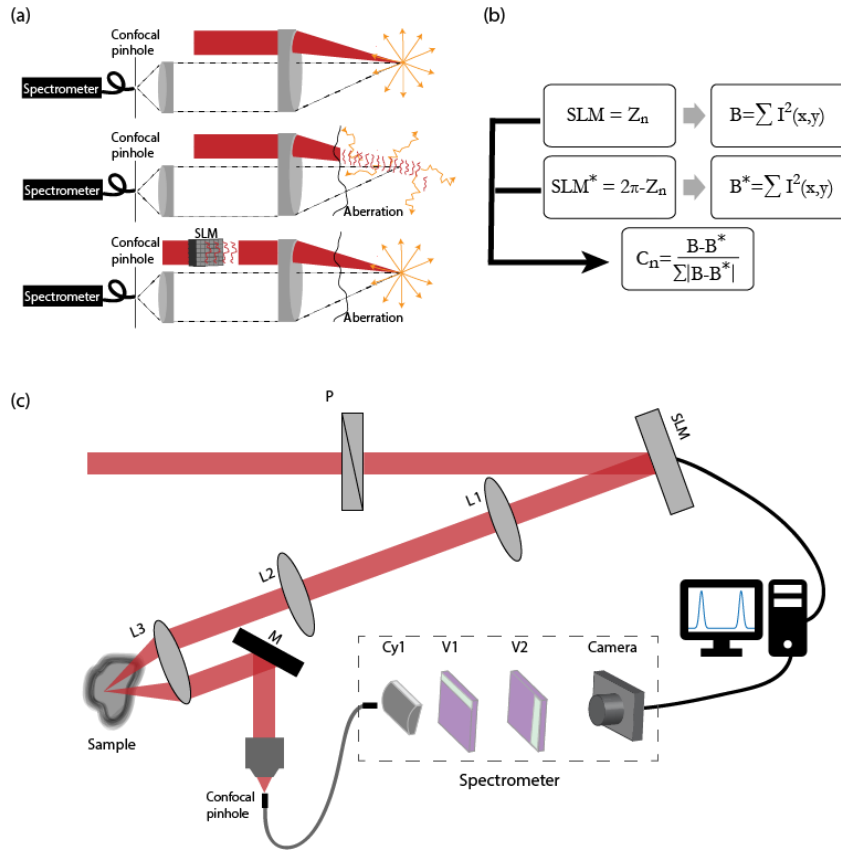
Fig. 8.1. AO optimization process and setup: (a) Enhancement mechanism: in the presence of aberrations, the region in which the Brillouin photons are generated is extended, and therefore many Brillouin photons are blocked by the confocal pinhole. (b) Optimization steps: Zernike polynomials and their inverse are projected on the SLM; the relative difference between the intensity values determines the magnitude of the measured Zernike polynomial. (c) Optical setup: A polarized expanded single frequency laser beam ($\lambda = 660nm$) is reflected off the surface of an SLM, and the plane of the SLM is imaged onto the back entrance of a 40mm focal length lens. The light focused on the sample generates Brillouin photons which are back scattered and spectrally dispersed by a double stage VIPA spectrometer; a feedback loop is used to enhance the intensity of the acquired Brillouin spectrum.

Following the protocol first presented by Booth et al (Booth et al., 2002), our process of determining the optimized SLM phase is illustrated in figure 8.1(b). As a basis for phase aberrations we used the set of orthogonal Zernike polynomials (normalized to 2π) which are well suited for circular boundary conditions. At every step of the iterative process, we sequentially projected on the SLM one Zernike polynomial and its inverse, and measured the intensity metric

response of the spectrum for both conjugated Zernike polynomial patterns (denoted by B, B^*). The coefficient of each Zernike polynomial was determined by the relative weight of the intensity squared difference $\Delta B = B - B^*$. We measured the response difference of the first twenty-one Zernike polynomials excluding the vertical and horizontal tilt phases which represent merely a lateral shift of the focal point. To minimize the influence of random intensity fluctuations on the phase optimization protocol, we set a threshold on the final coefficient amplitude and after performing a weighted average of the calculated Zernike coefficients we projected the final corrected phase on the SLM. Considering the uniform phase projected on the SLM at the first step of the iterative process, the total number of iterations is $2N + 1$, where N is the number of selected Zernike polynomials.

The experimental configuration of our AO-Brillouin system is presented in figure 8.1(c). We expanded a single frequency laser beam of wavelength 660 nm (LaserQuantum) and transmitted it through a linear polarizer to ensure a phase-only spatial modulation. We then reflected the beam off the surface of a spatial light modulator (LCOS-SLM, Hamamatsu X10468-01), and imaged the SLM plane using a 4-f imaging system (L1, L2, f=200mm) onto the back entrance of lens L3 (f=40mm) focusing the beam onto the sample of interest. We adopted a dual axis confocal configuration which has reduced collection efficiency compared to epi-detection, but it eliminates noise generated by back reflections and yields higher axial resolution for a given numerical aperture (Liu et al., 2007). We collected the scattered light and coupled it into a single mode fiber, serving as a confocal pinhole. Light was then dispersed by the double-stage VIPA spectrometer with a 15GHz free-spectral-range (Edrei et al., 2017a), and the resulting Brillouin spectrum was detected by an EMCCD camera (Andor Ixon 897).

8.3 Experimental results

To characterize the improvement of our AO-Brillouin system, we prepared a phantom sample featuring repeated layers of two different adhesive tapes (layer thickness ~70µm). An aberration was generated by spreading a thin layer of glue on the exterior surface of the sample; a chamber filled with water was then attached to the interior side (figure 8.2(a)). We performed the optimization process as described above on the water section of the sample and found the optimal Zernike coefficients (figure 8.2(b) bar graph), by repeating the iterative process several times we confirmed that the process is robust and constantly provides the same estimation for the sample aberrations. The dominant aberrations in this case are coma and astigmatism which are typically introduced by refractive index mismatches and thus expected in our case. The iterative process enhanced the intensity of the water signal by ∼2.5-fold as shown in figure 8.2(c). Although the enhancement factors are highly sample dependent, our enhancement results are consistent with previously reported AO studies for a variety of optical modalities applied to phantom samples as well as brain and ocular tissue (Ji et al., 2012, Wright et al., 2007, Roorda et al., 2002). Specifically, in Brillouin spectroscopy the signal can arise from any point in the illuminated region (as in a fluorescent sea) in which lower enhancements are expected (Ji et al., 2012). AO correction also improves spatial resolution because of a sharper focal point at the measured location. To evaluate the resolution improvement, we performed an axial scan of the layered sample, and measured the Brillouin shift at each axial location before and after the AO correction. The optimal axial resolution of our system was previously characterized to be 47 µm at FWHM, sufficient to observe the layered structure. As the aberration is introduced, the resolution of the system degrades to approximately 80 µm without the AO phase correction, and the layers of the sample cannot be distinguished (figure 8.2(d), blue dots). However, when AO correction is applied, the layers can

be clearly resolved (figure 8.2(d), orange dots) and the resolution of the system is enhanced to 57 µm, approaching the optimal performances.
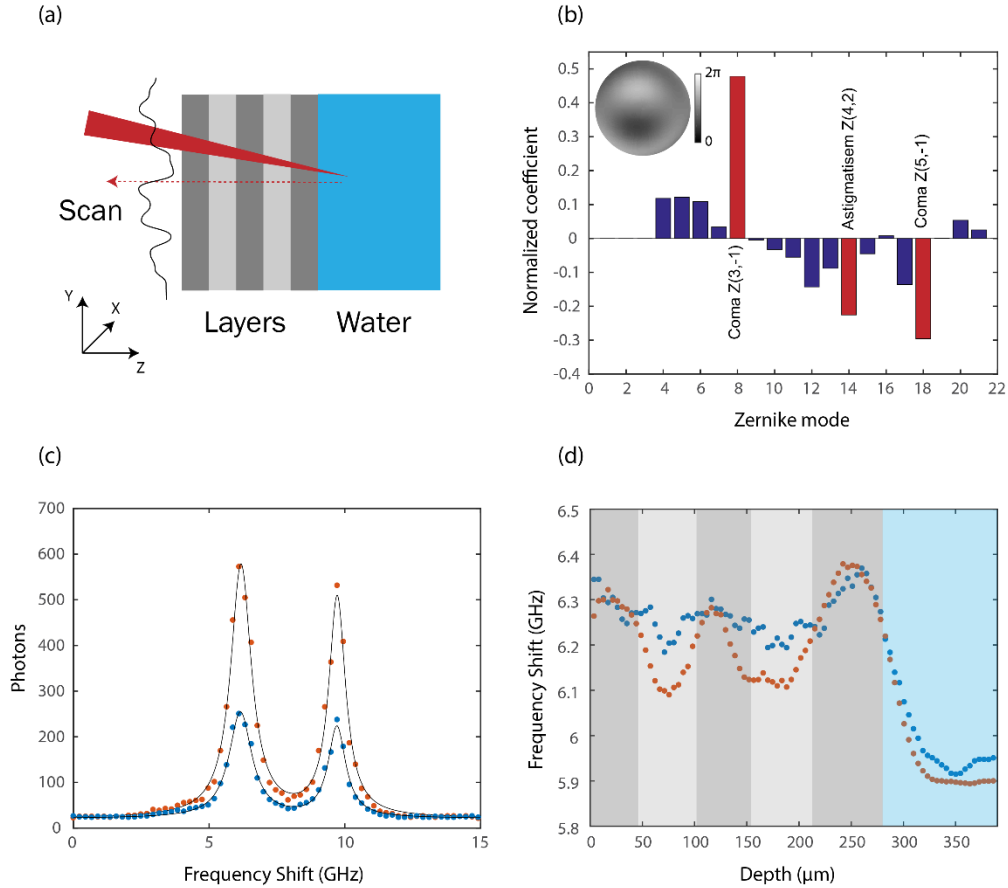
Fig. 8.2. Signal and resolution enhancement: (a) The phantom sample: a layered structure composed of two types of transparent adhesive tapes placed in front of a home-built water chamber; an aberration was introduced by spreading a layer of glue on the sample. (b) The normalized Zernike coefficients obtained by the iterative algorithm. The red bars represent the most significant modes (obtained by setting a threshold on the coefficients magnitudes), and the inset shows the phase map combining these modes. The iterative process was performed in $\sim 40\ sec$. (c) The Brillouin spectrum showing the Stokes and anti-Stokes peaks of water without AO (blue dots) and with AO (orange dots), as well as a double Lorentzian fit (black line). The elastic scattering peak originally located at zero frequency shift is invisible due to the high extinction ratio provided by the spectrometer. (d) An axial scan of the sample with AO (orange dots) and without AO (blue dots).

In this measurement the optimization routine was performed only once throughout the entire axial scan. The region in which the optimized phase is still effective at correcting the aberration defines the isoplanatic patch, which is sample dependent. In the case of this phantom sample, the axial isoplanatic patch covered the entire sample and we observed 50% signal enhancement up to 300 microns away from the corrected location. A large isoplanatic axial range is expected in the case of a single layer transparent aberration; for comparison, within scattering biological tissues such as the mouse brain the isoplanatic correction volume has been previously found to be approximately 100 μm^3 (Ji et al., 2012, Wang et al., 2014a).

To demonstrate the advantage of our system within biological samples we performed an axial measurement through the cornea and aqueous humor of a fresh porcine eye (figure 8.3(a)). Although the cornea is transparent, the signal intensity drops considerably as a function of depth due to aberrations (figure 8.3(b) blue dots). In these conditions, the AO correction increased Brillouin signal intensity up to more than 2-fold (figure 8.3(b) orange dots). The enhancement became more significant at greater depths, as expected, given the increased signal degradation due to aberrations introduced by the cornea (figure 8.3(c)).
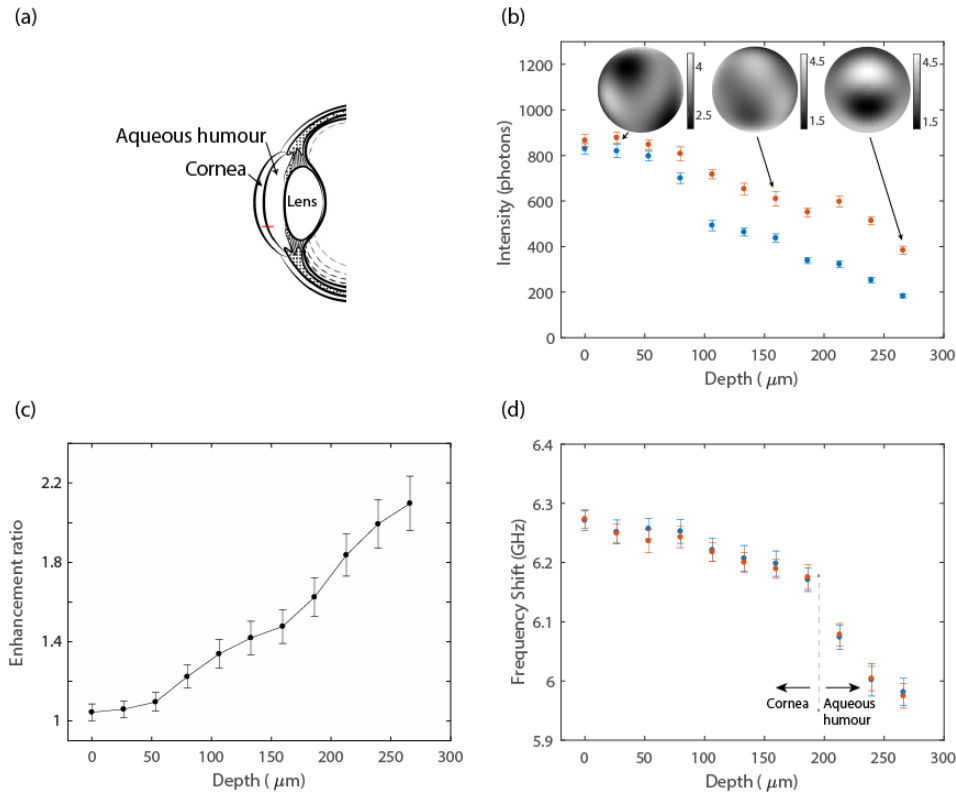
Fig. 8.3. Cornea and aqueous humor scan: (a) Structure of the porcine eye and the scanned region (red line). (b) The intensity of the Brillouin signal at various depths 27 microns apart throughout the cornea and aqueous humor of a fresh porcine eye. The optimization was performed at each location and three representative phase maps are shown. At higher depths the signal was enhanced by more than 2-fold when AO was applied (orange dots) vs the uncorrected signal intensity (blue dots). (c) Signal enhancement as a function of measurement depth. (d) The Brillouin shift at every location in (b), with (orange dots) and without (blue dots) AO correction. Error bars represent the standard deviation of twenty measurements.

In figure 8.3(d) the Brillouin frequency shift is presented for every optimized location with (orange dots) and without (blue dots) AO correction. The difference in the Brillouin shift values falls within the standard deviation of the measurement. This result is relevant for practical purposes; an active element placed within the optical path can change location of the focal point while converging towards the optimal signal enhancement. Particularly, in Brillouin spectroscopy, the signal is not confined to a point object as in fluorescence microscopy but can originate from any point within the illuminated region (as in a so-called fluorescent sea). As a result, because the active element

113

can easily shift the illumination focal point (e.g. our SLM can axially dislocate the focal point by hundreds of microns), when the signal intensity has a spatial gradient as is the case along the z-axis of the cornea sample, the tendency of the system to shift the measured location along the intensity gradient can be significant. In our experiment, the dislocation of the measured point was negligible, and the AO phase projection provided similar Brillouin shift values as the uncorrected scenario (figure 8.3(d)). We further confirmed this result by repeating the iterative process many times at a single location of the cornea and obtaining a variation in Brillouin shift of less than 10MHz, i.e. less than the single-point shift precision of our spectrometer. The reason we were able to avoid such measurement artifact is due to the confocal gating built within the setup, i.e. while the optimization process was performed on the illumination arm of the system, the collection path was kept fixed. Under these circumstances, a dislocation of the focal point will result in a mismatch between the illuminated point and the confocal pinhole which will decrease the signal intensity.

Besides nicer looking images/spectra obtained by AO, in certain scenarios AO is essential to enable a measurement by overcoming a fundamental barrier. As an example, we consider the case where the SNR of the acquired spectrum is less than one due to aberrations. In this scenario, the signal cannot be recovered by increasing the integration time of the measurement or averaging many acquired spectra. To demonstrate this, we used a glass bottle filled with methanol as a test sample and introduced an aberration on the glass by spreading a layer of glue (figure 8.4(a)). Because of the low SNR caused by aberrations and poor Brillouin gain of glass (Faris et al., 1993), measuring the Brillouin signal of glass through the aberration was impossible and averaging over many acquired spectra didn't increase the SNR of the measurement at all (figure 8.4(b), left panel). To demonstrate the power of AO correction in this scenario, we performed the optimization process on the methanol (which has high Brillouin gain) near the glass-methanol interface, i.e.

within the isoplanatic patch. After obtaining the appropriate phase correction, we axially translated the sample to measure the Brillouin signature of glass and obtained a spectrum with SNR>1 that could be averaged for proper spectral analysis (figure 8.4(b), right panel). Under these conditions, AO offered a unique solution to enable spectral analysis as seen by the line plot in figure 8.4(c).
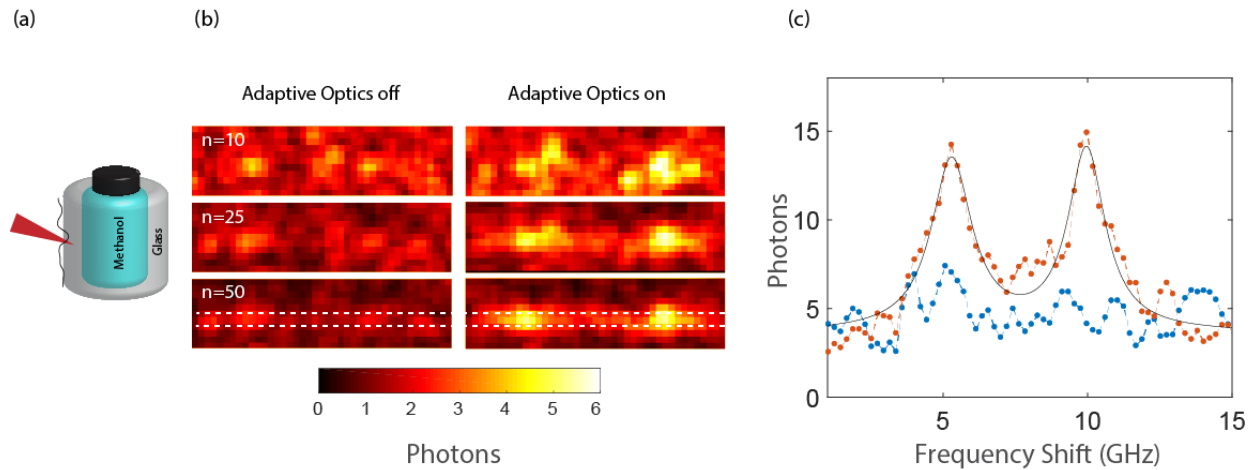
Fig. 8.4. AO-enabled measurements at low SNR: (a) Schematics of the experimental configuration. (b) Average of many acquired spectra of glass without AO (left) and with AO (right). A Gaussian filter (3x3 pixel, σ=2) was applied to the data. (c) Line plot of the area between the white dashed lines in (b). The spectrum of glass is not visible even when 50 frames are averaged if AO is not applied (blue); however, with AO correction on, the spectrum can be easily measured (orange).

8.4 Discussion

As previously mentioned, in this work we adopted the indirect approach to AO correction and enhanced the Brillouin signal through an iterative process based on the acquired spectra. This approach is made possible by the rapid acquisition times characteristic of VIPA-based spectrometers which can be as low as 50 ms. Nevertheless, in the presence of aberrations, the indirect AO correction results in an overall optimization process of tens of seconds; this is clearly a drawback of this approach that makes this method suitable to non-absorbing samples where long

illumination times are not a concern or to samples where isoplanatic regions are large enough that the iterative process needs to only be performed once for the entire scanned region (Ji et al., 2012, Wang et al., 2014a). For other samples, a direct AO approach where aberrations are rapidly measured and corrected is required; to do so, a suitable 'guide-star' such as a fluorescent bead needs to be inserted into the sample at various locations, alternatively, scattering/reflections from internal structures within the samples can be used as 'guide-stars'. The performances of the direct and indirect AO implementations are expected to be similar, with the exception that indirect approaches can be applied to more scattering samples where the wave-front provided by the 'guide-star' has been shown to not be viable (Ji, 2017).

In conclusion, we demonstrated for the first time an AO-Brillouin micro-spectrometer and obtained a 2.5-fold signal enhancement and a 1.4-fold resolution improvement using phantom samples and biological specimens such as the cornea of the eye. As optical elastrography modalities are widely being adopted for biomechanical studies, our system can enable elasticity mapping with higher precision and deeper within specimens thus potentially extending the applications of this emerging technique.

Chapter 9

Discussion and outlook

9.1 Discussion and highlighted contributions

The extensive search for optical techniques with superior capabilities to enable imaging and focusing through scattering materials is driven by the excellent resolution provided by optical modalities compared with other imaging tools such as MRI ultrasound or X-ray systems (Ntziachristos, 2010). Yet, scattering remains the greatest barrier in this context as absorption of biological tissues is negligible in the visible spectrum.

The deterioration of optical performances due to scattering is apparent in all optical modalities, however, it represents a different and unique challenge for each optical system. As a result, throughout my graduate studies, I have invented and developed several different methods that are effective in different scenarios and for different applications. In chapter 2 I developed a new method to image through dynamic scattering medium using coherent light. With this method, I was able to image through highly unstable media and very thick samples (> 3 mm of chicken breast tissue). The configuration I designed has been well received and highly cited by this community and was adopted by several laboratories which conducted follow-up studies to this work (Stern and Katz, 2018, Salhov et al., 2018, Viswanath et al., 2018, Li et al., 2018). Chapter

3 provides a framework for incoherent imaging through scattering media such as fluorescence microscopy. This work paves the way towards using deconvolution approaches, typically applied to deblur images, to enable imaging through scattering medium. Also this work has been acknowledged by colleagues in the field, and was recently adopted to enable fluorescent imaging through scattering media (Schneider and Aegerter, 2018, Edrei and Scarcelli, 2016a). Both methods presented in chapters 2 and 3 are limited to a relatively small angular range determined by the scattering characteristics. In practice this limitation means that the object of interest either needs to be located far from the scattering layer or to be very small. The scenarios in which this requirement is naturally fulfilled is when the retina is imaged through a cataracted lens or when the internal structures of the ear is imaged through the tympanic membrane.

Focusing through scattering is very important for scanning based modalities, in chapter 4 I analyzed the recently developed methods to focus through scattering materials: I derived and demonstrated the ultimate limits of these modalities and as a consequence I provided a general framework to compute optimal conditions to obtain the highest focal contrast (Edrei and Scarcelli, 2018b). This work is practically important for the many studies in the field as it provides a practical guide for choosing the focusing plane, and clearly describes the trade-off between the chosen plane and the confinement of the focal point. It is important to realize that even when a high contrast focal point is obtained behind a highly scattering medium, the vast majority of the energy is still dispersed over a large area and only a few percentages of the incoming light is focused to the focal point. This implies that such an approach will be very difficult to implement in scenarios where high intensity needs to be delivered to a confined location such as in Brillouin spectroscopy which has a very small scattering cross-section.

In part II of the thesis I studied scattering effects in the context of Brillouin spectroscopy. In chapter 5 I developed a method to reduce scattering effects by designing a coronograph filter element into current spectrometers. This method was patented and was integrated into our spectrometers and also adopted by several other groups in the field (Pukhlyakova et al., 2018, Zhang et al., 2018). Chapter 6 describes an alternative method to perform data analysis and obtain higher SNR, this method is beneficial in scenarios of low background noise.

Due to the inherently low number of photons comprising the Brillouin signals, even week aberrations are prohibitive in this context and result in a significant signal degradation. Hence, I decided to apply adaptive optics techniques, which are designed to counteract week aberrations, to enhance the Brillouin signal within aberrating materials. However, I realized that AO when applied to spectroscopy yields different results than those reported in other fields, and therefore the optical configuration needs to be modified accordingly. In chapter 7 I showed how the performances of adaptive optics systems degrade when signal is diffused over the entire illumination path rather than localized by a small labeled particle. This is an important result for many studies in the field of adaptive optics since in many scenarios the signal of interest can arise from different locations within the sample and is particularly relevant for the case of Brillouin spectroscopy. In chapter 8 I applied for the first time, adaptive optics to Brillouin spectroscopy; considering the results of chapter 7, I modified the system to accommodate the requirements of spectroscopy. My results have been the basis of a successful grant application (Glaucoma Research Foundation) from the lab to apply Brillouin spectroscopy in the back of the eye to study optical nerve biomechanics and its relation to glaucoma onset. In practice, AO signal enhancement is useful for point measurements of materials with a naturally very low Brillouin gain, as well as for scanning protocols where the AO correction needs to be performed infrequently since mare than

10 sec are required to perform the correction. For instance, in many cases aberrations can arise from refractive index mismatches between air and the sample of interest or from slight tilts of the sample, in these scenarios the correction is uniform and therefore the process needs to be performed only once.

9.2 Future directions

The fundamental concepts described in this thesis were mainly demonstrated using artificial scattering layers or ex-vivo samples; future progress in the field can lead to the translation of these approaches to real-life scenarios and clinical applications. The imaging modalities presented in chapters 2 and 3 can be used to image the retina through a cataracted lens or to examine internal structures of the ear through the Tympanic membrane. Clinical translation of these methods will be strongly dependent on technology development. For instance, the main drawback of the method developed in chapter 2 as well as of similar reported techniques is the image restoration from an autocorrelation function. This challenge can be accommodated by advancements in computational methods. Another drawback of these modalities which needs to be addressed to enable their realistic implementation is the lack of axial resolution, i.e. they have an infinite depth of field. This has been partially solved using coherence gating (Salhov et al., 2018), but was so far only demonstrated over large scales and on very simple objects.

The coronagraph presented in chapter 5 together with the AO enhancement described in chapters 7 and 8 can potentially be combined with high extinction spectrometers to enable Brillouin measurements in non-transparent samples. Such ability will require a fast and accurate estimation of phase aberrations, which can be accommodated by development of state-of-the-art devices with high projection rates high reflectivity and many degrees of freedom. Additionally,

advances in spectrometer capabilities such as higher throughput at a high extinction ratio is expected to promote this desired capability.

Another direction that my research could contribute to advance is applications where the reconstruction of a full image through scattering is not necessary. For instance, tracking of objects behind walls and within scattering materials as well as studying spacing and pattern recognition where demonstrated (Gariepy et al., 2016, Satat et al., 2017, Marcos et al., 1996). In these types of applications, the extent to which scattering effects needs to be eliminated is lower and so more options can be explored.

As a general prediction regarding future progress in the field, the new approach according to which scattering is considered beneficial to optical modalities when properly treated seems promising. For instance, while speckles generated by scattering events are typically considered to be noise which should be removed, some studies have been using such outcome to measure substrate elasticity (Nadkarni et al., 2005, Hajjarian and Nadkarni, 2012, Tripathi et al., 2014) or to obtain focusing and imaging capabilities beyond the diffraction limit (Vellekoop et al., 2010). Following this exciting trend, in my thesis I presented several approaches using scattering as an advantage rather than treating it as a nuisance.

Bibliography

ANDERSON, B. R., GUNAWIDJAJA, R. & EILERS, H. 2014. Effect of experimental parameters on optimal transmission of light through opaque media. *Physical Review A,* 90**,** 053826.

ANDREOLI, D., VOLPE, G., POPOFF, S., KATZ, O., GRESILLON, S. & GIGAN, S. 2015. Deterministic control of broadband light through a multiply scattering medium via the multispectral transmission matrix. *Scientific Reports,* 5.

ANTIPA, N., KUO, G., HECKEL, R., MILDENHALL, B., BOSTAN, E., NG, R. & WALLER, L. 2018. DiffuserCam: lensless single-exposure 3D imaging. *Optica,* 5**,** 1-9.

ANTONACCI, G. & BRAAKMAN, S. 2016. Biomechanics of subcellular structures by non-invasive Brillouin microscopy. *Scientific Reports,* 6.

ANTONACCI, G., DE PANFILIS, S., DI DOMENICO, G., DELRE, E. & RUOCCO, G. 2016. Breaking the Contrast Limit in Single-Pass Fabry-Pérot Spectrometers. *Physical Review Applied,* 6**,** 054020.

ANTONACCI, G., LEPERT, G., PATERSON, C. & TOROK, P. 2015a. Elastic suppression in Brillouin imaging by destructive interference. *Applied Physics Letters,* 107.

ANTONACCI, G., PEDRIGI, R. M., KONDIBOYINA, A., MEHTA, V. V., DE SILVA, R., PATERSON, C., KRAMS, R. & TÖRÖK, P. 2015b. Quantification of plaque stiffness by Brillouin microscopy in experimental thin cap fibroatheroma. *Journal of the Royal Society Interface,* 12**,** 20150843.

ARTAL, P., IGLESIAS, I., LOPEZGIL, N. & GREEN, D. G. 1995a. DOUBLE-PASS MEASUREMENTS OF THE RETINAL-IMAGE QUALITY WITH UNEQUAL ENTRANCE AND EXIT PUPIL SIZES AND THE REVERSIBILITY OF THE EYES OPTICAL-SYSTEM. *Journal of the Optical Society of America a-Optics Image Science and Vision,* 12**,** 2358-2366.

ARTAL, P., MARCOS, S., NAVARRO, R. & WILLIAMS, D. R. 1995b. ODD ABERRATIONS AND DOUBLE-PASS MEASUREMENTS OF RETINAL IMAGE QUALITY. *Journal of the Optical Society of America a-Optics Image Science and Vision,* 12**,** 195-201.

AZUCENA, O., CREST, J., KOTADIA, S., SULLIVAN, W., TAO, X., REINIG, M., GAVEL, D., OLIVIER, S. & KUBBY, J. 2011. Adaptive optics wide-field microscopy using direct wavefront sensing. *Optics letters,* 36**,** 825-827.

BALLMANN, C., THOMPSON, J., TRAVERSO, A., MENG, Z., SCULLY, M. & YAKOVLEV, V. 2015. Stimulated Brillouin Scattering Microscopic Imaging. *Scientific Reports,* 5.

BALLMANN, C. W., MENG, Z., TRAVERSO, A. J., SCULLY, M. O. & YAKOVLEV, V. V. 2017. Impulsive Brillouin microscopy. *Optica,* 4**,** 124-128.

BAUDOZ, P., GAY, J. & RABBIA, Y. 1998. Interfero-coronagraphy: A tool for detection of faint companions. Workshop on Brown Dwarfs and Extrasolar Planets, Mar 17-21 1997 Puerto La Cruz, Spain. 254-261.

BECKERS, J. M. 1993. ADAPTIVE OPTICS FOR ASTRONOMY - PRINCIPLES, PERFORMANCE, AND APPLICATIONS. *Annual Review of Astronomy and Astrophysics,* 31**,** 13-62.

BENEDEK, G. & FRITSCH, K. 1966. Brillouin scattering in cubic crystals. *Physical Review,* 149**,** 647.

BERGHAUS, K., ZHANG, J., YUN, S. H. & SCARCELLI, G. 2015a. High-finesse sub-GHz-resolution spectrometer employing VIPA etalons of different dispersion. *Optics Letters,* 40**,** 4436-4439.

BERGHAUS, K. V., YUN, S. H. & SCARCELLI, G. 2015b. High Speed Sub-GHz Spectrometer for Brillouin Scattering Analysis. *Jove-Journal of Visualized Experiments*.

BERTOLOTTI, J., VAN PUTTEN, E., BLUM, C., LAGENDIJK, A., VOS, W. & MOSK, A. 2012. Non-invasive imaging through opaque scattering layers. *Nature,* 491**,** 232-234.

BESNER, S., SCARCELLI, G., PINEDA, R. & YUN, S.-H. 2016. In Vivo Brillouin Analysis of the Aging Crystalline LensIn Vivo Brillouin Analysis of the Aging Human Lens. *Investigative Ophthalmology & Visual Science,* 57**,** 5093-5100.

BETZIG, E., PATTERSON, G. H., SOUGRAT, R., LINDWASSER, O. W., OLENYCH, S., BONIFACINO, J. S., DAVIDSON, M. W., LIPPINCOTT-SCHWARTZ, J. & HESS, H. F. 2006. Imaging intracellular fluorescent proteins at nanometer resolution. *Science,* 313**,** 1642-1645.

BOOTH, M., ANDRADE, D., BURKE, D., PATTON, B. & ZURAUSKAS, M. 2015. Aberrations and adaptive optics in super-resolution microscopy. *Microscopy,* 64**,** 251-261.

BOOTH, M. J. 2007. Adaptive optics in microscopy. *Philosophical Transactions of the Royal Society of London A: Mathematical, Physical and Engineering Sciences,* 365**,** 2829-2843.

BOOTH, M. J. 2014. Adaptive optical microscopy: the ongoing quest for a perfect image. *Light-Science & Applications,* 3.

BOOTH, M. J., NEIL, M. A. & WILSON, T. 1998. Aberration correction for confocal imaging in refractive-index-mismatched media. *Journal of Microscopy,* 192**,** 90-98.

BOOTH, M. J., NEIL, M. A. A., JUSKAITIS, R. & WILSON, T. 2002. Adaptive aberration correction in a confocal microscope. *Proceedings of the National Academy of Sciences of the United States of America,* 99**,** 5788-5792.

BOYD, R. W. 2008. Nonlinear Optics, 3rd Edition. *Nonlinear Optics, 3rd Edition***,** 1-613.

CATLIN, D. & DAINTY, C. 2002. High-resolution imaging of the human retina with a Fourier deconvolution technique. *Journal of the Optical Society of America a-Optics Image Science and Vision,* 19**,** 1515-1523.

CERBINO, R. 2007. Correlations of light in the deep Fresnel region: An extended Van Cittert and Zernike theorem. *Physical Review A,* 75.

CHEONG, W. F., PRAHL, S. A. & WELCH, A. J. 1990. A REVIEW OF THE OPTICAL-PROPERTIES OF BIOLOGICAL TISSUES. *Ieee Journal of Quantum Electronics,* 26**,** 2166-2185.

CHOI, Y., YANG, T. D., FANG-YEN, C., KANG, P., LEE, K. J., DASARI, R. R., FELD, M. S. & CHOI, W. 2011. Overcoming the Diffraction Limit Using Multiple Light Scattering in a Highly Disordered Medium. *Physical Review Letters,* 107.

CHRISTOU, J. C., ROORDA, A. & WILLIAMS, D. R. 2004. Deconvolution of adaptive optics retinal images. *Journal of the Optical Society of America a-Optics Image Science and Vision,* 21**,** 1393-1401.

CONKEY, D. B., CARAVACA-AGUIRRE, A. M. & PIESTUN, R. 2012. High-speed scattering medium characterization with application to focusing light through turbid media. *Optics Express,* 20**,** 1733-1740.

CUI, M. & YANG, C. 2010. Implementation of a digital optical phase conjugation system and its application to study the robustness of turbidity suppression by phase conjugation. *Optics Express,* 18**,** 3444-3455.

DAINTY, J. C. Laser speckle and related phenomena. Berlin and New York, Springer-Verlag (Topics in Applied Physics. Volume 9), 1975. 298 p, 1975.

DENK, W., STRICKLER, J. H. & WEBB, W. W. 1990. Two-photon laser scanning fluorescence microscopy. *Science,* 248**,** 73-76.

DERODE, A., ROUX, P. & FINK, M. 1995. Robust acoustic time reversal with high-order multiple scattering. *Physical review letters,* 75**,** 4206.

DI BATTISTA, D., ZACHARAKIS, G. & LEONETTI, M. 2015. Enhanced adaptive focusing through semi-transparent media. *Scientific reports,* 5**,** 17406.

DIL, J. G. 1982. BRILLOUIN-SCATTERING IN CONDENSED MATTER. *Reports on Progress in Physics,* 45**,** 285-334.

DÉBARRE, D., BOTCHERBY, E. J., WATANABE, T., SRINIVAS, S., BOOTH, M. J. & WILSON, T. 2009. Image-based adaptive optics for two-photon microscopy. *Optics letters,* 34**,** 2495-2497.

EDREI, E., GATHER, M. & SCARCELLI, G. 2017a. Integration of spectral coronagraphy within VIPA-based spectrometers for high extinction Brillouin imaging. *Optics Express,* 25**,** 6895.

EDREI, E., NIKOLIC, M. & SCARCELLI, G. 2017b. Improving localization precision of Brillouin measurements using spectral autocorrelation analysis. *Journal of Innovative Optical Health Sciences,* 10**,** 1742004.

EDREI, E. & SCARCELLI, G. 2016a. Memory-effect based deconvolution microscopy for super-resolution imaging through scattering media. *Scientific Reports,* 6.

EDREI, E. & SCARCELLI, G. 2016b. Optical imaging through dynamic turbid media using the Fourier-domain shower-curtain effect. *Optica,* 3**,** 71-74.

EDREI, E. & SCARCELLI, G. 2018a. Brillouin micro-spectroscopy through aberrations via sensorless adaptive optics. *Applied Physics Letters,* 112.

EDREI, E. & SCARCELLI, G. 2018b. Focusing through scattering medium: a fundamental trade-off between speckle size and intensity enhancement. *arXiv preprint arXiv:1808.07830*.

ELSAYAD, K., WERNER, S., GALLEMÍ, M., KONG, J., GUAJARDO, E. R. S., ZHANG, L., JAILLAIS, Y., GREB, T. & BELKHADIR, Y. 2016. Mapping the subcellular mechanical properties of live cells in tissues with fluorescence emission–Brillouin imaging. *Sci. Signal.,* 9**,** rs5-rs5.

FARIS, G. W., JUSINSKI, L. E. & HICKMAN, A. P. 1993. High-resolution stimulated Brillouin gain spectroscopy in glasses and crystals. *JOSA B,* 10**,** 587-599.

FENG, S. C., KANE, C., LEE, P. A. & STONE, A. D. 1988. CORRELATIONS AND FLUCTUATIONS OF COHERENT WAVE TRANSMISSION THROUGH DISORDERED MEDIA. *Physical Review Letters,* 61**,** 834-837.

FIENUP, J. 1977. RECONSTRUCTION OF AN OBJECT FROM MODULUS OF ITS FOURIER-TRANSFORM. *Journal of the Optical Society of America,* 67**,** 1389-1389.

FIENUP, J. R. 1978. RECONSTRUCTION OF AN OBJECT FROM MODULUS OF ITS FOURIER-TRANSFORM. *Optics Letters,* 3**,** 27-29.

FIENUP, J. R. 1982. PHASE RETRIEVAL ALGORITHMS - A COMPARISON. *Applied Optics,* 21**,** 2758-2769.

FIORE, A., ZHANG, J., SHAO, P., YUN, S. & SCARCELLI, G. 2016. High-extinction virtually imaged phased array-based Brillouin spectroscopy of turbid biological media. *Applied Physics Letters,* 108.

FLEURY, P. A. & BOON, J. P. 1969. Brillouin scattering in simple liquids: argon and neon. *Physical Review,* 186**,** 244.

FREUND, I. 1990. LOOKING THROUGH WALLS AND AROUND CORNERS. *Physica A,* 168**,** 49-65.

FREUND, I., ROSENBLUH, M. & FENG, S. 1988. MEMORY EFFECTS IN PROPAGATION OF OPTICAL WAVES THROUGH DISORDERED MEDIA. *Physical Review Letters,* 61**,** 2328-2331.

GARIEPY, G., TONOLINI, F., HENDERSON, R., LEACH, J. & FACCIO, D. 2016. Detection and tracking of moving objects hidden from view. *Nature Photonics,* 10**,** 23-U32.

GIGLIO, M., CARPINETI, M., VAILATI, A. & BROGIOLI, D. 2001. Near-field intensity correlations of scattered light. *Applied Optics,* 40**,** 4036-4040.

GIRARD, M. J., DUPPS, W. J., BASKARAN, M., SCARCELLI, G., YUN, S. H., QUIGLEY, H. A., SIGAL, I. A. & STROUTHIDIS, N. G. 2015. Translating ocular biomechanics into clinical practice: current state and future prospects. *Current eye research,* 40**,** 1-18.

GOODMAN, J. W. 2005. *Introduction to Fourier optics*, Roberts and Company Publishers.

GOODMAN, J. W. 2007. *Speckle phenomena in optics: theory and applications*, Roberts and Company Publishers.

GOODMAN, J. W. & HAUPT, R. L. 2015. *Statistical optics*, John Wiley & Sons.

HAJJARIAN, Z. & NADKARNI, S. K. 2012. Evaluating the Viscoelastic Properties of Tissue from Laser Speckle Fluctuations. *Scientific Reports,* 2.

HARDY, J. W. 1998. *Adaptive optics for astronomical telescopes*, Oxford University Press on Demand.

HARTSCHUH, R. D., KISLIUK, A., NOVIKOV, V., SOKOLOV, A. P., HEYLIGER, P. R., FLANNERY, C. M., JOHNSON, W. L., SOLES, C. L. & WU, W. L. 2005. Acoustic modes and elastic properties of polymeric nanostructures. *Applied Physics Letters,* 87.

HELMCHEN, F. & DENK, W. 2005. Deep tissue two-photon microscopy. *Nature Methods,* 2**,** 932-940.

HERMANN, B., FERNÁNDEZ, E., UNTERHUBER, A., SATTMANN, H., FERCHER, A., DREXLER, W., PRIETO, P. & ARTAL, P. 2004. Adaptive-optics ultrahigh-resolution optical coherence tomography. *Optics letters,* 29**,** 2142-2144.

HORSTMEYER, R., RUAN, H. & YANG, C. 2015. Guidestar-assisted wavefront-shaping methods for focusing light into biological tissue. *Nature Photonics,* 9**,** 563-571.

HORTON, N. G., WANG, K., KOBAT, D., CLARK, C. G., WISE, F. W., SCHAFFER, C. B. & XU, C. 2013. In vivo three-photon microscopy of subcortical structures within an intact mouse brain. *Nature Photonics,* 7**,** 205-209.

HSIEH, C.-L., PU, Y., GRANGE, R. & PSALTIS, D. 2010. Digital phase conjugation of second harmonic radiation emitted by nanoparticles in turbid media. *Optics Express,* 18**,** 12283-12290.

HSU, C. W., GOETSCHY, A., BROMBERG, Y., STONE, A. D. & CAO, H. 2015. Broadband Coherent Enhancement of Transmission and Absorption in Disordered Media. *Physical Review Letters,* 115.

HUANG, D., SWANSON, E. A., LIN, C. P., SCHUMAN, J. S., STINSON, W. G., CHANG, W., HEE, M. R., FLOTTE, T., GREGORY, K. & PULIAFITO, C. A. 1991. Optical coherence tomography. *Science,* 254**,** 1178-1181.

HUFF, J. 2015. The Airyscan detector from ZEISS: confocal imaging with improved signal-to-noise ratio and super-resolution. *Nature Methods,* 12.

IDELL, P. S., FIENUP, J. R. & GOODMAN, R. S. 1987. IMAGE SYNTHESIS FROM NONIMAGED LASER-SPECKLE PATTERNS. *Optics Letters,* 12**,** 858-860.

IDELL, P. S., GONGLEWSKI, J. D., VOELZ, D. G. & KNOPP, J. 1989. IMAGE SYNTHESIS FROM NONIMAGED LASER-SPECKLE PATTERNS - EXPERIMENTAL-VERIFICATION. *Optics Letters,* 14**,** 154-156.

IGLESIAS, I., LOPEZ-GIL, N. & ARTAL, P. 1998. Reconstruction of the point-spread function of the human eye from two double-pass retinal images by phase-retrieval algorithms. *Journal of the Optical Society of America a-Optics Image Science and Vision,* 15**,** 326-339.

JACQUES, S. L. 2013. Optical properties of biological tissues: a review. *Physics in Medicine and Biology,* 58**,** R37-R61.

JANG, M., HORIE, Y., SHIBUKAWA, A., BRAKE, J., LIU, Y., KAMALI, S. M., ARBABI, A., RUAN, H., FARAON, A. & YANG, C. 2018. Wavefront shaping with disorder-engineered metasurfaces. *Nature Photonics***,** 1.

JI, N. 2017. Adaptive optical fluorescence microscopy. *Nature Methods,* 14**,** 374-380.

JI, N., MILKIE, D. E. & BETZIG, E. 2010. Adaptive optics via pupil segmentation for high-resolution imaging in biological tissues. *Nature Methods,* 7**,** 141-U84.

JI, N., SATO, T. R. & BETZIG, E. 2012. Characterization and adaptive optical correction of aberrations during in vivo imaging in the mouse cortex. *Proceedings of the National Academy of Sciences,* 109**,** 22-27.

JOHNSEN, S. & WIDDER, E. A. 1999. The physical basis of transparency in biological tissue: Ultrastructure and the minimization of light scattering. *Journal of Theoretical Biology,* 199**,** 181-198.

JOHNSTON, D. C. & WELSH, B. M. 1994. ANALYSIS OF MULTICONJUGATE ADAPTIVE OPTICS. *Journal of the Optical Society of America a-Optics Image Science and Vision,* 11**,** 394-408.

JORAND, R., LE CORRE, G., ANDILLA, J., MAANDHUI, A., FRONGIA, C., LOBJOIS, V., DUCOMMUN, B. & LORENZO, C. 2012. Deep and clear optical imaging of thick inhomogeneous samples. *PLoS One,* 7**,** e35795.

KAMALI, S. M., ARBABI, E., ARBABI, A., HORIE, Y. & FARAON, A. 2016. Highly tunable elastic dielectric metasurface lenses. *Laser & Photonics Reviews,* 10**,** 1002-1008.

KATZ, O., HEIDMANN, P., FINK, M. & GIGAN, S. 2014a. Non-invasive single-shot imaging through scattering layers and around corners via speckle correlations. *Nature Photonics,* 8**,** 784-790.

KATZ, O., SMALL, E., GUAN, Y. & SILBERBERG, Y. 2014b. Noninvasive nonlinear focusing and imaging through strongly scattering turbid layers. *Optica,* 1**,** 170-174.

KATZ, O., SMALL, E. & SILBERBERG, Y. 2012. Looking around corners and through thin turbid layers in real time with scattered incoherent light. *Nature Photonics,* 6**,** 549-553.

KOSKI, K. J., AKHENBLIT, P., MCKIERNAN, K. & YARGER, J. L. 2013. Non-invasive determination of the complete elastic moduli of spider silks. *Nature materials,* 12**,** 262-267.

KUNDUR, D. & HATZINAKOS, D. 1996. Blind image deconvolution. *Ieee Signal Processing Magazine,* 13**,** 43-64.

LABEYRIE, A. 1970. ATTAINMENT OF DIFFRACTION LIMITED RESOLUTION IN LARGE TELESCOPES BY FOURIER ANALYSING SPECKLE PATTERNS IN STAR IMAGES. *Astronomy & Astrophysics,* 6**,** 85-+.

LEONETTI, M., GRIMALDI, A., RUOCCO, G. & ANTONACCI, G. 2018. Scattering-assisted localization microscopy. *arXiv preprint arXiv:1804.01511*.

LI, G., LI, D. & SITU, G. Single shot imaging through turbid medium and around corner using coherent light. 2017 International Conference on Optical Instruments and Technology: Optoelectronic Imaging/Spectroscopy and Signal Processing Technology, 2018. International Society for Optics and Photonics, 1062005.

LI, J., BEAULIEU, D. R., PAUDEL, H., BARANKOV, R., BIFANO, T. G. & MERTZ, J. 2015. Conjugate adaptive optics in widefield microscopy with an extended-source wavefront sensor. *Optica,* 2**,** 682-688.

LIBERMAN, L., ISRAEL, Y., POEM, E. & SILBERBERG, Y. 2016. Quantum enhanced phase retrieval. *Optica,* 3**,** 193-199.

LIU, J. T., MANDELLA, M. J., RA, H., WONG, L. K., SOLGAARD, O., KINO, G. S., PIYAWATTANAMETHA, W., CONTAG, C. H. & WANG, T. D. 2007. Miniature near-infrared dual-axes confocal microscope utilizing a two-dimensional microelectromechanical systems scanner. *Optics letters,* 32**,** 256-258.

LIU, Y., LAI, P., MA, C., XU, X., GRABAR, A. A. & WANG, L. V. 2015. Optical focusing deep inside dynamic scattering media with near-infrared time-reversed ultrasonically encoded (TRUE) light. *Nature Communications,* 6.

LUCY, L. B. 1974. ITERATIVE TECHNIQUE FOR RECTIFICATION OF OBSERVED DISTRIBUTIONS. *Astronomical Journal,* 79**,** 745-754.

LYOT, M. A study of the Solar Corona And Prominences Without Eclipses, 1939. *MNRAS,* 99**,** 580.

MARCOS, S., NAVARRO, R. & ARTAL, P. 1996. Coherent imaging of the cone mosaic in the living human eye. *Journal of the Optical Society of America a-Optics Image Science and Vision,* 13**,** 897-905.

MATTANA, S., CARDINALI, M. A., CAPONI, S., PIERANTONI, D. C., CORTE, L., ROSCINI, L., CARDINALI, G. & FIORETTO, D. 2017. High-contrast Brillouin and Raman micro-spectroscopy for simultaneous mechanical and chemical investigation of microbial biofilms. *Biophysical chemistry,* 229**,** 123-129.

MAWET, D., RIAUD, P., ABSIL, O. & SURDEJ, J. 2005. Annular groove phase mask coronagraph. *Astrophysical Journal,* 633**,** 1191-1200.

MCNALLY, J. G., KARPOVA, T., COOPER, J. & CONCHELLO, J. A. 1999. Three-dimensional imaging by deconvolution microscopy. *Methods-a Companion to Methods in Enzymology,* 19**,** 373-385.

MENG, Z., TRAVERSO, A. & YAKOVLEV, V. 2014. Background clean-up in Brillouin microspectroscopy of scattering medium. *Optics Express,* 22**,** 5410-5415.

MENG, Z., TRAVERSO, A. J., BALLMANN, C. W., TROYANOVA-WOOD, M. A. & YAKOVLEV, V. V. 2016. Seeing cells in a new light: a renaissance of Brillouin spectroscopy. *Advances in Optics and Photonics,* 8**,** 300-327.

MERTZ, J., PAUDEL, H. & BIFANO, T. G. 2015. Field of view advantage of conjugate adaptive optics in microscopy applications. *Applied Optics,* 54**,** 3498-3506.

MINAMI, Y. & SAKAI, K. 2009. Ripplon on high viscosity liquid. *Review of Scientific Instruments,* 80.

MOURANT, J. R., FREYER, J. P., HIELSCHER, A. H., EICK, A. A., SHEN, D. & JOHNSON, T. M. 1998. Mechanisms of light scattering from biological cells relevant to noninvasive optical-tissue diagnostics. *Applied Optics,* 37**,** 3586-3593.

NADKARNI, S. K., BOUMA, B. E., HELG, T., CHAN, R., HALPERN, E., CHAU, A., MINSKY, M. S., MOTZ, J. T., HOUSER, S. L. & TEARNEY, G. J. 2005. Characterization of atherosclerotic plaques by laser speckle imaging. *Circulation,* 112**,** 885-892.

NTZIACHRISTOS, V. 2010. Going deeper than microscopy: the optical imaging frontier in biology. *Nature Methods,* 7**,** 603-614.

OBER, R. J., RAM, S. & WARD, E. S. 2004. Localization accuracy in single-molecule microscopy. *Biophysical Journal,* 86**,** 1185-1200.

PALOMBO, F., WINLOVE, C. P., EDGINTON, R. S., GREEN, E., STONE, N., CAPONI, S., MADAMI, M. & FIORETTO, D. 2014. Biomechanics of fibrous proteins of the extracellular matrix studied by Brillouin scattering. *Journal of The Royal Society Interface,* 11**,** 20140739.

PAPADOPOULOS, I. N., FARAHI, S., MOSER, C. & PSALTIS, D. 2012. Focusing and scanning light through a multimode optical fiber using digital phase conjugation. *Optics Express,* 20**,** 10583-10590.

PAPADOPOULOS, I. N., FARAHI, S., MOSER, C. & PSALTIS, D. 2013. High-resolution, lensless endoscope based on digital scanning through a multimode optical fiber. *Biomedical Optics Express,* 4**,** 260-270.

PARIGI, V., PERROS, E., BINARD, G., BOURDILLON, C., MAÎTRE, A., CARMINATI, R., KRACHMALNICOFF, V. & DE WILDE, Y. 2016. Near-field to far-field characterization of speckle patterns generated by disordered nanomaterials. *Optics express,* 24**,** 7019-7027.

PARK, J.-H., PARK, C., YU, H., PARK, J., HAN, S., SHIN, J., KO, S. H., NAM, K. T., CHO, Y.-H. & PARK, Y. 2013. Subwavelength light focusing using random nanoparticles. *Nature Photonics,* 7**,** 455-459.

PARK, J.-H., SUN, W. & CUI, M. 2015. High-resolution in vivo imaging of mouse brain through the intact skull. *Proceedings of the National Academy of Sciences of the United States of America,* 112**,** 9236-9241.

PARK, Y., CHOI, W., YAQOOB, Z., DASARI, R., BADIZADEGAN, K. & FELD, M. S. 2009. Speckle-field digital holographic microscopy. *Optics Express,* 17**,** 12285-12292.

PAUDEL, H. P., STOCKBRIDGE, C., MERTZ, J. & BIFANO, T. 2013. Focusing polychromatic light through strongly scattering media. *Optics Express,* 21**,** 17299-17308.

PAWLEY, J. 2010. *Handbook of biological confocal microscopy*, Springer Science & Business Media.

PIERRAT, R., AMBICHL, P., GIGAN, S., HABER, A., CARMINATI, R. & ROTTER, S. 2014. Invariance property of wave scattering through disordered media. *Proceedings of the National Academy of Sciences of the United States of America,* 111**,** 17765-17770.

PLOSCHNER, M., TYC, T. & CIZMAR, T. 2015. Seeing through chaos in multimode fibres. *Nature Photonics,* 9**,** 529-+.

POPOFF, S., LEROSEY, G., FINK, M., BOCCARA, A. C. & GIGAN, S. 2010a. Image transmission through an opaque material. *Nature Communications,* 1.

POPOFF, S. M., LEROSEY, G., CARMINATI, R., FINK, M., BOCCARA, A. C. & GIGAN, S. 2010b. Measuring the transmission matrix in optics: an approach to the study and control of light propagation in disordered media. *Physical review letters,* 104**,** 100601.

PUKHLYAKOVA, E., AMAN, A. J., ELSAYAD, K. & TECHNAU, U. 2018. beta-Catenin-dependent mechanotransduction dates back to the common ancestor of Cnidaria and Bilateria. *Proceedings of the National Academy of Sciences of the United States of America,* 115**,** 6231-6236.

RAGAZZONI, R., MARCHETTI, E. & VALENTE, G. 2000. Adaptive-optics corrections available for the whole sky. *Nature,* 403**,** 54-56.

RAHMAN, S. A. & BOOTH, M. J. 2013. Direct wavefront sensing in adaptive optical microscopy using backscattered light. *Applied Optics,* 52**,** 5523-5532.

REMER, I. & BILENCA, A. 2016a. Background-free Brillouin spectroscopy in scattering media at 780 nm via stimulated Brillouin scattering. *Optics Letters,* 41**,** 926-929.

REMER, I. & BILENCA, A. 2016b. High-speed stimulated Brillouin scattering spectroscopy at 780 nm. *Apl Photonics,* 1.

RICHARDS.WH 1972. BAYESIAN-BASED ITERATIVE METHOD OF IMAGE RESTORATION. *Journal of the Optical Society of America,* 62**,** 55-&.

RODDIER, F. & RODDIER, C. 1997. Stellar coronagraph with phase mask. *Publications of the Astronomical Society of the Pacific,* 109**,** 815-820.

ROORDA, A., ROMERO-BORJA, F., DONNELLY, W. J., QUEENER, H., HEBERT, T. J. & CAMPBELL, M. C. W. 2002. Adaptive optics scanning laser ophthalmoscopy. *Optics Express,* 10**,** 405-412.

ROORDA, A. & WILLIAMS, D. R. 1999. The arrangement of the three cone classes in the living human eye. *Nature,* 397**,** 520-522.

ROUAN, D., RIAUD, P., BOCCALETTI, A., CLENET, Y. & LABEYRIE, A. 2000. The four-quadrant phase-mask coronagraph. I. Principle. *Publications of the Astronomical Society of the Pacific,* 112**,** 1479-1486.

RUAN, H., BRAKE, J., ROBINSON, J. E., LIU, Y., JANG, M., XIAO, C., ZHOU, C., GRADINARU, V. & YANG, C. 2017. Deep tissue optical focusing and optogenetic modulation with time-reversed ultrasonically encoded light. *Science advances,* 3**,** eaao5520.

RUECKEL, M., MACK-BUCHER, J. A. & DENK, W. 2006. Adaptive wavefront correction in two-photon microscopy using coherence-gated wavefront sensing. *Proceedings of the National Academy of Sciences of the United States of America,* 103**,** 17137-17142.

RUST, M. J., BATES, M. & ZHUANG, X. 2006. Sub-diffraction-limit imaging by stochastic optical reconstruction microscopy (STORM). *Nature Methods,* 3**,** 793-795.

RYU, J., JANG, M., EOM, T. J., YANG, C. & CHUNG, E. 2016. Optical phase conjugation assisted scattering lens: variable focusing and 3D patterning. *Scientific Reports,* 6.

SALHOV, O., WEINBERG, G. & KATZ, O. 2018. Depth-Resolved Speckle-Correlations Imaging through Scattering Layers. *arXiv preprint arXiv:1808.02926.*

SANDERCOCK, J. 1970. Brillouin scattering study of SbSI using a double-passed, stabilised scanning interferometer. *Optics Communications,* 2**,** 73-76.

SARDER, P. & NEHORAI, A. 2006. Deconvolution methods for 3-D fluorescence microscopy images. *Ieee Signal Processing Magazine,* 23**,** 32-45.

SATAT, G., TANCIK, M., GUPTA, O., HESHMAT, B. & RASKAR, R. 2017. Object classification through scattering media with deep learning on time resolved measurement. *Optics Express,* 25**,** 17466-17479.

SAVO, R., PIERRAT, R., NAJAR, U., CARMINATI, R., ROTTER, S. & GIGAN, S. 2017. Observation of mean path length invariance in light-scattering media. Science, 358, 765-+.

SCARCELLI, G., BESNER, S., PINEDA, R., KALOUT, P. & YUN, S. H. 2015a. In Vivo Biomechanical Mapping of Normal and Keratoconus Corneas. *Jama Ophthalmology,* 133**,** 480-482.

SCARCELLI, G., KIM, P. & YUN, S. H. 2008. Cross-axis cascading of spectral dispersion. *Optics Letters,* 33**,** 2979-2981.

SCARCELLI, G., PINEDA, R. & YUN, S. H. 2012. Brillouin Optical Microscopy for Corneal Biomechanics. *Investigative Ophthalmology & Visual Science,* 53**,** 185-190.

SCARCELLI, G., POLACHECK, W. J., NIA, H. T., PATEL, K., GRODZINSKY, A. J., KAMM, R. D. & YUN, S. H. 2015b. Noncontact three-dimensional mapping of intracellular hydromechanical properties by Brillouin microscopy. *Nature Methods,* 12**,** 1132-+.

SCARCELLI, G. & YUN, S. H. 2008. Confocal Brillouin microscopy for three-dimensional mechanical imaging. *Nature Photonics,* 2**,** 39-43.

SCARCELLI, G. & YUN, S. H. 2011. Multistage VIPA etalons for high-extinction parallel Brillouin spectroscopy. *Optics Express,* 19**,** 10913-10922.

SCARCELLI, G. & YUN, S. H. 2012. In vivo Brillouin optical microscopy of the human eye. *Optics Express,* 20**,** 9197-9202.

SCHERMELLEH, L., HEINTZMANN, R. & LEONHARDT, H. 2010. A guide to super-resolution fluorescence microscopy. *Journal of Cell Biology,* 190**,** 165-175.

SCHNEIDER, J. & AEGERTER, C. M. 2018. Guide star based deconvolution for imaging behind turbid media. *Journal of the European Optical Society-Rapid Publications,* 14**,** 21.

SCHOTT, S., BERTOLOTTI, J., LEGER, J.-F., BOURDIEU, L. & GIGAN, S. 2015. Characterization of the angular memory effect of scattered light in biological tissues. *Optics Express,* 23**,** 13505-13516.

SERGA, A. A., SCHNEIDER, T., HILLEBRANDS, B., DEMOKRITOV, S. O. & KOSTYLEV, M. P. 2006. Phase-sensitive Brillouin light scattering spectroscopy from spin-wave packets. *Applied Physics Letters,* 89.

SHAO, P., BESNER, S., ZHANG, J., SCARCELLI, G. & YUN, S. 2016. Etalon filters for Brillouin microscopy of highly scattering tissues. *Optics Express,* 24**,** 22232-22238.

SHECHTMAN, Y., ELDAR, Y. C., COHEN, O., CHAPMAN, H. N., MIAO, J. & SEGEV, M. 2015. Phase Retrieval with Application to Optical Imaging. *Ieee Signal Processing Magazine,* 32**,** 87-109.

SIBARITA, J. B. 2005. Deconvolution microscopy. *Microscopy Techniques,* 95**,** 201-243.

SINEFELD, D., PAUDEL, H. P., OUZOUNOV, D. G., BIFANO, T. G. & XU, C. 2015. Adaptive optics in multiphoton microscopy: comparison of two, three and four photon fluorescence. *Optics express,* 23**,** 31472-31483.

SIVARAMAKRISHNAN, A., KORESKO, C. D., MAKIDON, R. B., BERKEFELD, T. & KUCHNER, M. J. 2001. Ground-based coronagraphy with high-order adaptive optics. *Astrophysical Journal,* 552**,** 397-408.

STARCK, J. L., PANTIN, E. & MURTAGH, F. 2002. Deconvolution in astronomy: A review. *Publications of the Astronomical Society of the Pacific,* 114**,** 1051-1069.

STEELMAN, Z., MENG, Z., TRAVERSO, A. J. & YAKOVLEV, V. V. 2015. Brillouin spectroscopy as a new method of screening for increased CSF total protein during bacterial meningitis. *Journal of biophotonics,* 8**,** 408-414.

STERN, G. & KATZ, O. 2018. Non-invasive Focusing Through Scattering Layers Using Speckle-Correlations. *arXiv preprint arXiv:1808.03267*.

STILL, T., SAINIDOU, R., RETSCH, M., JONAS, U., SPAHN, P., HELLMANN, G. P. & FYTAS, G. 2008. The "Music" of Core-Shell Spheres and Hollow Capsules: Influence of the Architecture on the Mechanical Properties at the Nanoscale. *Nano Letters,* 8**,** 3194-3199.

TAO, X., AZUCENA, O., FU, M., ZUO, Y., CHEN, D. C. & KUBBY, J. 2011a. Adaptive optics microscopy with direct wavefront sensing using fluorescent protein guide stars. *Optics Letters,* 36**,** 3389-3391.

TAO, X., FERNANDEZ, B., AZUCENA, O., FU, M., GARCIA, D., ZUO, Y., CHEN, D. C. & KUBBY, J. 2011b. Adaptive optics confocal microscopy using direct wavefront sensing. *Optics letters,* 36**,** 1062-1064.

TAXT, T. 1995. RESTORATION OF MEDICAL ULTRASOUND IMAGES USING 2-DIMENSIONAL HOMOMORPHIC DECONVOLUTION. *Ieee Transactions on Ultrasonics Ferroelectrics and Frequency Control,* 42**,** 543-554.

THOMPSON, J. V., THROCKMORTON, G. A., HOKR, B. H. & YAKOVLEV, V. V. 2016. Wavefront shaping enhanced Raman scattering in a turbid medium. *Optics Letters,* 41**,** 1769-1772.

THOMPSON, R. E., LARSON, D. R. & WEBB, W. W. 2002. Precise nanometer localization analysis for individual fluorescent probes. *Biophysical Journal,* 82**,** 2775-2783.

TRIPATHI, M. M., HAJJARIAN, Z., VAN COTT, E. M. & NADKARNI, S. K. 2014. Assessing blood coagulation status with laser speckle rheology. *Biomedical Optics Express,* 5**,** 817-831.

TURCOTTE, R., LIANG, Y. & JI, N. 2017. Adaptive optical versus spherical aberration corrections for in vivo brain imaging. *Biomedical optics express,* 8**,** 3891-3902.

TYSON, R. K. 2015. *Principles of adaptive optics*, CRC press.

TZANG, O., CARAVACA-AGUIRRE, A. M., WAGNER, K. & PIESTUN, R. 2018. Adaptive wavefront shaping for controlling nonlinear multimode interactions in optical fibres. *Nature Photonics,* 12**,** 368-+.

VAN BEIJNUM, F., VAN PUTTEN, E. G., LAGENDIJK, A. & MOSK, A. P. 2011. Frequency bandwidth of light focused through turbid media. *Optics Letters,* 36**,** 373-375.

VAN PUTTEN, E., AKBULUT, D., BERTOLOTTI, J., VOS, W. L., LAGENDIJK, A. & MOSK, A. 2011. Scattering lens resolves sub-100 nm structures with visible light. *Physical review letters,* 106**,** 193905.

VELLEKOOP, I. M. 2015. Feedback-based wavefront shaping. *Optics express,* 23**,** 12189-12206.

VELLEKOOP, I. M. & AEGERTER, C. M. Focusing light through living tissue. BiOS, 2010. International Society for Optics and Photonics, 755430-755430-10.

VELLEKOOP, I. M., LAGENDIJK, A. & MOSK, A. P. 2010. Exploiting disorder for perfect focusing. *Nature Photonics,* 4**,** 320-322.

VELLEKOOP, I. M. & MOSK, A. 2008a. Phase control algorithms for focusing light through turbid media. *Optics communications,* 281**,** 3071-3080.

VELLEKOOP, I. M. & MOSK, A. 2008b. Universal optimal transmission of light through disordered materials. *Physical review letters,* 101**,** 120601.

VELLEKOOP, I. M. & MOSK, A. P. 2007. Focusing coherent light through opaque strongly scattering media. *Optics Letters,* 32**,** 2309-2311.

VISWANATH, A., RANGARAJAN, P., MACFARLANE, D. & CHRISTENSEN, M. P. Indirect Imaging Using Correlography. Imaging and Applied Optics 2018 (3D, AO, AIO, COSI, DH, IS, LACSEA, LS&C, MATH, pcAOP), 2018/06/25 2018 Orlando, Florida. Optical Society of America, CM2E.3.

VOELZ, D. G., GONGLEWSKI, J. D. & IDELL, P. S. 1991. IMAGE SYNTHESIS FROM NONIMAGED LASER-SPECKLE PATTERNS - COMPARISON OF THEORY, COMPUTER-SIMULATION, AND LABORATORY RESULTS. *Applied Optics,* 30**,** 3333-3344.

WANG, C., LIU, R., MILKIE, D. E., SUN, W., TAN, Z., KERLIN, A., CHEN, T.-W., KIM, D. S. & JI, N. 2014a. Multiplexed aberration measurement for deep tissue imaging in vivo. *Nature methods,* 11**,** 1037-1040.

WANG, D., ZHOU, E. H., BRAKE, J., RUAN, H., JANG, M. & YANG, C. 2015a. Focusing through dynamic tissue with millisecond digital optical phase conjugation. *Optica,* 2**,** 728-735.

WANG, K., MILKIE, D. E., SAXENA, A., ENGERER, P., MISGELD, T., BRONNER, M. E., MUMM, J. & BETZIG, E. 2014b. Rapid adaptive optical recovery of optimal resolution over large volumes. *Nature Methods,* 11**,** 625-+.

WANG, K., SUN, W., RICHIE, C. T., HARVEY, B. K., BETZIG, E. & JI, N. 2015b. Direct wavefront sensing for high-resolution in vivo imaging in scattering tissue. *Nature Communications,* 6.

WANG, Y. M., JUDKEWITZ, B., DIMARZIO, C. A. & YANG, C. 2012. Deep-tissue focal fluorescence imaging with digitally time-reversed ultrasound-encoded light. *Nature Communications,* 3.

WRIGHT, A., POLAND, S., GIRKIN, J., FREUDIGER, C., EVANS, C. & XIE, X. 2007. Adaptive optics for enhanced signal in CARS microscopy. *Optics express,* 15**,** 18209-18219.

YANG, X., PU, Y. & PSALTIS, D. 2014. Imaging blood cells through scattering biological tissue using speckle scanning microscopy. *Optics Express,* 22**,** 3405-3413.

YAQOOB, Z., PSALTIS, D., FELD, M. S. & YANG, C. 2008. Optical phase conjugation for turbidity suppression in biological samples. *Nature Photonics,* 2**,** 110-115.

YAROSLAVSKY, A. N., SCHULZE, P. C., YAROSLAVSKY, I. V., SCHOBER, R., ULRICH, F. & SCHWARZMAIER, H. J. 2002. Optical properties of selected native and coagulated human brain tissues in vitro in the visible and near infrared spectral range. *Physics in Medicine and Biology,* 47**,** 2059-2073.

YILMAZ, H., VOS, W. L. & MOSK, A. P. 2013. Optimal control of light propagation through multiple-scattering media in the presence of noise. *Biomedical optics express,* 4**,** 1759-1768.

YORK, A. G., PAREKH, S. H., NOGARE, D. D., FISCHER, R. S., TEMPRINE, K., MIONE, M., CHITNIS, A. B., COMBS, C. A. & SHROFF, H. 2012. Resolution doubling in live, multicellular organisms via multifocal structured illumination microscopy. *Nature Methods,* 9**,** 749-U167.

ZAWADZKI, R. J., JONES, S. M., OLIVIER, S. S., ZHAO, M., BOWER, B. A., IZATT, J. A., CHOI, S., LAUT, S. & WERNER, J. S. 2005. Adaptive-optics optical coherence tomography for high-resolution and high-speed 3D retinal in vivo imaging. *Optics express,* 13**,** 8532-8546.

ZHANG, J., FIORE, A., YUN, S., KIM, H. & SCARCELLI, G. 2016. Line-scanning Brillouin microscopy for rapid non-invasive mechanical imaging. *Scientific Reports,* 6.

ZHANG, J., NOU, X. A., KIM, H. & SCARCELLI, G. 2017. Brillouin flow cytometry for label-free mechanical phenotyping of the nucleus. *Lab on a Chip,* 17**,** 663-670.

ZHANG, J., RAGHUNATHAN, R., RIPPY, J., WU, C., FINNELL, R. H., LARIN, K. V. & SCARCELLI, G. 2018. Tissue biomechanics during cranial neural tube closure measured by Brillouin microscopy and optical coherence tomography. *Birth defects research*.

ZHENG, W., WU, Y. C., WINTER, P., FISCHER, R., NOGARE, D. D., HONG, A., MCCORMICK, C., CHRISTENSEN, R., DEMPSEY, W. P., ARNOLD, D. B., ZIMMERBERG, J., CHITNIS, A., SELLERS, J., WATERMAN, C. & SHROFF, H. 2017. Adaptive optics improves multiphoton super-resolution imaging. *Nature Methods,* 14**,** 869-+.